Rovibrational Dynamics of Nuclei and Molecules

Jonathan Ian Rawlinson

University of Cambridge

Department of Applied Mathematics and Theoretical Physics

Queens' College

February 2020

This dissertation is submitted for
the degree of Doctor of Philosophy

Declaration

This dissertation is the result of my own work and includes nothing which is the outcome of work done in collaboration except as declared in the Preface and specified in the text. It is not substantially the same as any that I have submitted, or, is being concurrently submitted for a degree or diploma or other qualification at the University of Cambridge or any other University or similar institution except as declared in the Preface and specified in the text. I further state that no substantial part of my dissertation has already been submitted, or, is being concurrently submitted for any such degree, diploma or other qualification at the University of Cambridge or any other University or similar institution except as declared in the Preface and specified in the text.

Jonathan Ian Rawlinson
February 2020

Rovibrational Dynamics of Nuclei and Molecules

Jonathan Ian Rawlinson

We study quantized rotation-vibration dynamics with applications to nuclear and molecular models. Firstly we consider small vibrations of Skyrmions (topological solitons which model atomic nuclei), developing new approximations to their quantum energy spectra which incorporate both rotation-vibration and isorotation-vibration corrections. We find that the forms of these corrections are highly restricted as a consequence of the large symmetry groups of Skyrmions, and we determine them using representation theory. We explore the implications for the Helium-4 nucleus and the Lithium-7/Beryllium-7 isodoublet, comparing our findings with experimental data.

We propose a model for the Carbon-12 nucleus based on point α-particles restricted to isosceles triangular configurations, inspired by linear chain and equilateral triangular Skyrmions. The configuration space is not a manifold but has a graph-like structure, and we make use of Quantum Graph Theory to study the quantized dynamics. The resulting energy spectrum reproduces the experimental data rather well.

Nuclear physicists are interested in more than just the quantum energy spectrum: electromagnetic transition rates, for instance, measure γ-decay between two nuclear states and can be measured in the laboratory. We develop a formalism to compute electromagnetic transition rates within rotation-vibration models and compare the results of our Carbon-12 model and a recent Oxygen-16 model to experimental data. We go on to propose some ways in which the Oxygen-16 model might be improved.

Finally, we turn from nuclear physics to molecular physics and study the protonated methane molecular ion, introducing a quantum graph model for the complex rotation-vibration dynamics. We find good agreement with other numerical work where available and compute states up to angular momentum $J = 4$ for the first time.

Dedicated to Mum and Dad
for their endless love, wisdom and encouragement.

Acknowledgements

Contents

List of Figures

List of Tables

Chapter 1

Introduction

This thesis is concerned with rotational-vibrational (or *rovibrational*) dynamics. Rovibrational dynamics are of relevance to many physical systems: we focus on problems in nuclear physics in Chapters 2 to 5 before turning to molecular physics in Chapter 6. The rovibrational point of view is more familiar in the latter area of physics. We begin, therefore, by giving a brief outline of molecular vibrations and rotations.

Molecules are complex systems of atomic nuclei and electrons with many degrees of freedom. It is often possible to separate the electronic motion from the nuclear motion through the Born-Oppenheimer approximation. This results in a simpler problem: the atomic nuclei move in the presence of a Born-Oppenheimer potential V which captures the average effect of the electrons. If V has a deep minimum then the molecule stays close to this equilibrium. Methane (CH_4), for example, has a definite tetrahedral shape as illustrated in Figure 1.1. The molecule is free to rotate in space and perform small vibrations about the tetrahedral shape. If these vibrations are small enough then a further simplification is possible, namely the separation of vibrational and rotational degrees of freedom. Separability is taken as a first approximation and, if necessary, some corrections such as centrifugal effects and Coriolis couplings can be introduced to account for rovibrational interactions.

The separation of rotations and vibrations is often a very good approximation. However, there are systems of physical importance for which it breaks down. Phosphorus pentafluoride (PF_5) is a famous example. The equilibrium shape for PF_5 is illustrated in Figure 1.2. This arrangement involves two different kinds of $P - F$ bonds (axial and equatorial), owing to its trigonal bipyramidal structure. However, there is a relatively low energy barrier to the exchange of fluorine atoms between equatorial and axial positions via a continuous change of shape known as Berry pseudorotation [1]. This is thought to explain why NMR studies of PF_5 find only one type of ^{19}F resonant frequency instead of the naive two expected from the equilibrium structure [2].

A more dramatic breakdown occurs for protonated methane (CH_5^+): here, even just the
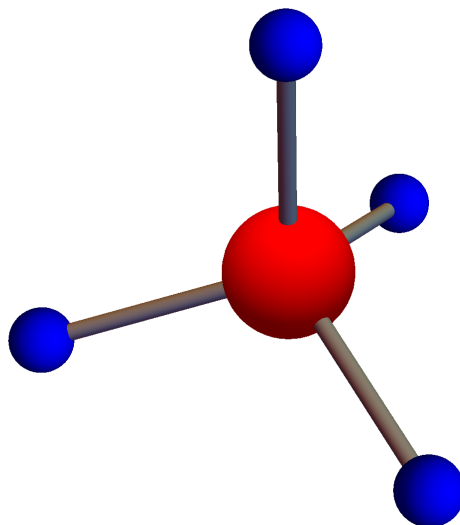
Figure 1.1: Tetrahedral structure of CH$_4$. C and H atoms are coloured red and blue respectively.
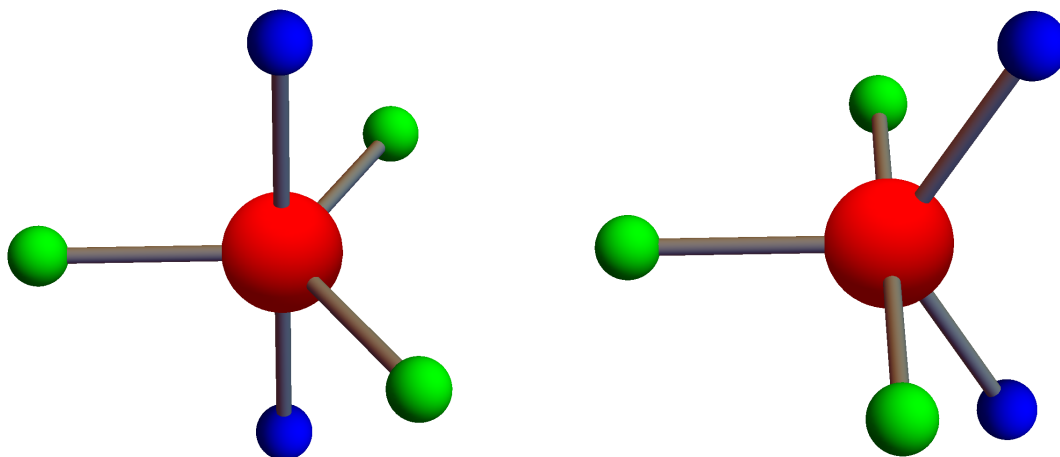
Figure 1.2: Trigonal bipyramidal structure of PF$_5$. P and F atoms are coloured red and blue/green respectively. In the left-hand configuration, green denotes equatorial F atoms while blue denotes axial F atoms. The axial atoms can easily become equatorial atoms by a motion called Berry pseudorotation, giving the right-hand configuration.

zero-point energies of the lowest vibrational modes are sufficiently large to overcome the energy barrier for exchange of the protons, allowing essentially free movement between the various minima on the Born-Oppenheimer potential energy surface [3]. Thus, even at zero temperature, CH_5^+ should not be pictured as having a definite shape but rather as constantly moving between the minima. The conventional techniques of molecular physics do not apply to such systems and the treatment of CH_5^+ has required creative new models such as the molecular superrotor [4] and the quantum graph model [5]. We will revisit CH_5^+ in Chapter 6.

Wheeler proposed long ago that light α-conjugate nuclei such as Carbon-12 and Oxygen-16 should be thought of as molecules of α-particles [6]. Carbon-12, for example, is based on an equilateral triangular arrangement of α-particles and Oxygen-16 on a tetrahedral arrangement. The only difference is that, in the absence of the Born-Oppenheimer potential of molecular physics, there is some freedom in choosing the potential energy. Once the potential energy is fixed, one can derive the quantum states of nuclei such as Carbon-12 and Oxygen-16 as rovibrational excitations in just the same way as in molecular physics. More generally, in nuclear models such as the Skyrme model, where nuclei appear as topological solitons, one pictures atomic nuclei as having some definite equilibrium shape with the possibility of vibrations and rotations about this shape. Thus a clear understanding of rovibrational dynamics is of importance for a variety of problems within nuclear physics as well as in molecular physics.

Recent work inspired by Skyrmion dynamics suggests that, even at low energies, the Oxygen-16 nucleus knows about shapes other than the minimal-energy tetrahedron of the traditional α-particle model [7]. These include a flat square, another highly symmetric arrangement of α-particles. In Chapter 3 we make an analogous proposal for Carbon-12. These models suggest it is better to compare Oxygen-16 and Carbon-12 to floppy molecules such as CH_5^+ than to rigid molecules such as CH_4. We will explore some more of the physical consequences of these models in Chapter 4, deriving electromagnetic transition rates between nuclear states.

Much of the literature on rovibrational dynamics is tied to the traditional small-vibration picture of molecular physics. From this perspective, it is hard to understand the complicated interplay between rotations and shape-deforming degrees of freedom that occur in more general nuclear and molecular models. We aim to clarify some of these issues by adopting a geometric approach, as described in Section 1.1 and Chapter 2. Chapters 3 to 6 involve a novel approximation, based on Quantum Graph Theory (QGT), relevant for situations where a molecule or nucleus can move between several different equilibria on a potential energy surface of the kind described above. We review some essential material from QGT in Section 1.2.

3

1.1 Geometric approach to deformable body dynamics

A novel approach to deformable body dynamics emerged in the 1980s in the work of Shapere and Wilczek [8]. Their work made it clear that the appropriate mathematical setting for the discussion of rotations and vibrations is that of principal bundles. The key idea is the following: the configuration space $\mathcal{C}$ of a deformable body, consisting of oriented shapes, has the structure of an SO(3)-bundle. The SO(3) action simply rotates configurations in physical space. Thus the base space is the space of unoriented shapes and the fibre above a given unoriented shape represents all the possible orientations of that shape in space.

Suppose one is interested in computing the net rotation undergone by a deformable body, under conditions of vanishing angular momentum, as the body changes its shape to traverse a closed loop in shape space. Shapere and Wilczek showed that this net rotation can be computed as the holonomy associated with a certain connection $\mathbf{A}$ on the bundle. In particular, the net rotation depends only on the path in shape space and is independent of the rate at which the body changes its shape. This elegant result illustrates the power of the geometric formulation of deformable body dynamics.

Many concepts in the traditional molecular physics literature such as Coriolis corrections and the subtleties of body-fixed frame definitions are most easily visualised and expressed in the language of principle bundles, becoming simple consequences of geometric facts such as the existence of the non-trivial connection $\mathbf{A}$ or the freedom to choose different gauges. In this thesis we aim to show how these concepts can be useful in developing molecular and nuclear models. In Chapter 2, in which we study the Coriolis corrections of molecular physics and their analogues in nuclear physics, we make use of a formulation of the quantum Hamiltonian for deformable body dynamics in which natural geometric objects such as the connection $\mathbf{A}$ are manifest.

1.2 Quantum graph theory

In QGT one is interested in describing the dynamics of a quantum particle confined to the edges of a metric graph Γ, consisting of vertices $v \in \mathcal{V}$ and edges $e \in \mathcal{E}$. In later chapters these vertices will represent equilibrium shapes of a molecule or nucleus, with the edges corresponding to low-energy paths between them. Suppose for now we are interested in free motion on the graph Γ for a particle of unit mass. On each edge $e \in \mathcal{E}$, it is natural to write down the time-independent Schrödinger equation (in units where $\hbar = 1$)

$$\mathcal{H}\psi_e\left(s\right) \equiv -\frac{1}{2}\frac{d^2}{ds^2}\psi_e\left(s\right) = E\psi_e\left(s\right), \tag{1.1}$$
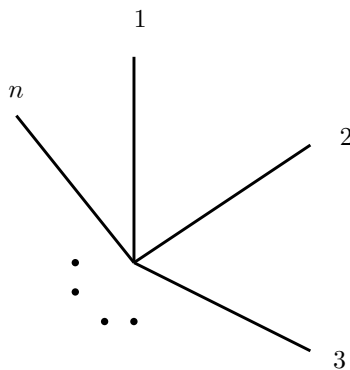
Figure 1.3: Star graph Γ_S.

where s is a coordinate along the edge and ψ_e is the wavefunction. But this is not enough to set up the quantum mechanical problem: we also need to specify appropriate boundary conditions at the vertices $v \in \mathcal{V}$. Here, by *appropriate* we mean boundary conditions which preserve familiar requirements of quantum theory such as self-adjointness of the Hamiltonian. We may wonder what is the complete set of such boundary conditions. This question can be answered using the mathematical theory of self-adjoint extensions. For our purposes, however, it will suffice to consider a simple example.

1.2.1   Quantum particle on a star graph

Consider the graph Γ_S illustrated in Figure 1.3, consisting of a single vertex which joins n edges. We define a coordinate s_i on edge i with the vertex at $s_i = 0$ and we demand that the wavefunction $\psi_i(s_i)$ satisfies the Schrödinger equation

$$\left(-\frac{1}{2}\frac{d^2}{ds_i^2} + V(s_i) \right) \psi_i(s_i) = E\psi_i(s_i) \tag{1.2}$$

which possibly involves a potential $V(s_i)$. Then the most common boundary conditions are the so-called *free* or *Kirchoff* boundary conditions

$$\sum_{i=1}^{N} \psi_i'(0) = 0 \tag{1.3}$$

$$\psi_1(0) = \psi_2(0) = \ldots \psi_N(0). \tag{1.4}$$

In words: the wavefunction is continuous at the vertex, with outgoing derivatives summing to zero. These are the vertex boundary conditions usually adopted in physical applications of QGT and will be our boundary conditions of choice whenever we talk about quantum mechanics on a graph. We now compute the spectrum for a free particle on a simple compact graph to illustrate how quantization proceeds.
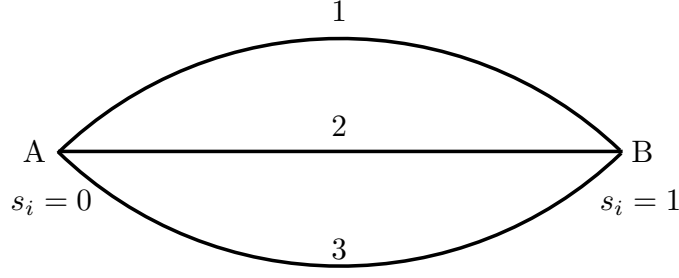
Figure 1.4: Three-edged graph Γ_3.

1.2.2 Quantum particle on compact three-edged graph

Consider the graph Γ_3 in Figure 1.4. Γ_3 has three edges labelled $1, 2, 3$ with coordinates s_1, s_2, s_3 respectively, with each coordinate s_i ranging from $s_i = 0$ (vertex A) to $s_i = 1$ (vertex B). We take the Schrödinger equation on each edge to be

$$-\frac{1}{2}\frac{d^2}{ds_i^2}\psi_i\left(s_i\right) = E\psi_i\left(s_i\right). \tag{1.5}$$

It follows that the wavefunction on edge i must take the form

$$\psi_i\left(s_i\right) = a_i \exp\left(iks_i\right) + b_i \exp\left(ik\left(1 - s_i\right)\right) \tag{1.6}$$

with $E = \frac{1}{2}k^2$. We will refer to k as the edge momentum. The vertex boundary conditions described in the previous section lead to linear constraints on the a_i and the b_i: continuity at vertex A implies

$$a_1 + b_1 \exp\left(ik\right) = a_2 + b_2 \exp\left(ik\right) = a_3 + b_3 \exp\left(ik\right) \tag{1.7}$$

while continuity at vertex B implies

$$a_1 \exp\left(ik\right) + b_1 = a_2 \exp\left(ik\right) + b_2 = a_3 \exp\left(ik\right) + b_3. \tag{1.8}$$

Finally, the condition on the sum of the outgoing derivatives at A and B leads to the conditions (for $k \neq 0$)

$$\left(a_1 + a_2 + a_3\right) - \left(b_1 + b_2 + b_3\right)\exp\left(ik\right) = 0 \tag{1.9}$$

and

$$\left(a_1 + a_2 + a_3\right)\exp\left(ik\right) - \left(b_1 + b_2 + b_3\right) = 0 \tag{1.10}$$

respectively. The above equations constitute, for generic k, a set of 6 linearly independent constraints on the a_i and the b_i giving no non-trivial solutions. However, for special values of k there will be a linear dependence between the constraints.

Explicitly, the above constraints are easily recast in matrix form as

$$
\begin{pmatrix}
e^{ik} & e^{ik} & e^{ik} & -1 & -1 & -1 \\
1 & 1 & 1 & -e^{ik} & -e^{ik} & -e^{ik} \\
1 & -1 & 0 & e^{ik} & -e^{ik} & 0 \\
1 & 0 & -1 & e^{ik} & 0 & -e^{ik} \\
e^{ik} & -e^{ik} & 0 & 1 & -1 & 0 \\
e^{ik} & 0 & -e^{ik} & 1 & 0 & -1
\end{pmatrix}
\begin{pmatrix}
a_1 \\ a_2 \\ a_3 \\ b_1 \\ b_2 \\ b_3
\end{pmatrix}
=
\begin{pmatrix}
0 \\ 0 \\ 0 \\ 0 \\ 0 \\ 0
\end{pmatrix}
\tag{1.11}
$$

and the matrix on the left has a non-trivial kernel if and only if it has vanishing determinant, that is if and only if

$$
0 = 9 \left(1 - e^{2ik} \right)^3
\tag{1.12}
$$

which is true precisely when

$$
k = n\pi
\tag{1.13}
$$

for $n \in \mathbb{Z}^+$. So the discrete energy spectrum is

$$
E = \frac{n^2 \pi^2}{2}
\tag{1.14}
$$

where $n \in \mathbb{Z}^+$, together with the special case

$$
E = 0
\tag{1.15}
$$

associated with the constant wavefunction ($k = 0$).

Chapter 2

Coriolis terms in Skyrmion quantization

This chapter is based on the single-author paper [9].

2.1   Introduction

In the Skyrme model approach to nuclear physics, atomic nuclei are identified with topological solitons in a nonlinear field theory of pions. These topological solitons are known as Skyrmions. Given a Skyrmion, one may use insights from the field theory dynamics to identify a small number of collective coordinates which are relevant at low energies. The collective coordinates chosen will typically include both rotations and isorotations of the Skyrmion together with other, shape-deforming, degrees of freedom: the nucleus is viewed as a deformable body which is free to rotate in space as well as isorotate in isospace. These degrees of freedom of the Skyrmion are then quantized, hopefully giving a reasonable description of the corresponding nucleus.

Naively one may hope to separate the zero modes (rotations and isorotations, corresponding to the action of the symmetry group $SU(2)_{\text{spin}} \times SU(2)_{\text{isospin}}$ on the Skyrmion) when quantizing this system. In some cases a complete factorisation is possible, but generally one has to live with interactions between zero modes and shape-deforming degrees of freedom. This kind of interaction is already understood in the molecular physics literature, where so-called Coriolis effects are known to play an important role in rovibrational spectra. Skyrmion quantization involves a slight generalisation: a molecule can rotate and vibrate, but a Skyrmion can additionally isorotate. Mathematically it is not difficult to incorporate isorotations, provided we have a clear understanding of the usual Coriolis effects. We choose to take a geometric perspective, as described in Chapter 1. A useful review article for quantization within the geometric point of view is [10] which we follow closely in this chapter.

In Section 2.2 we set up the general formalism before exploring various applications in the

following sections. In Section 2.3 we consider small vibrations of a Skyrmion and show how the problem simplifies in this case. Using these ideas, we compute the quantum spectrum of a vibrating and rotating $B = 4$ Skyrmion (with cubic symmetry) in section 2.4, finding good agreement with the observed excited states of the α-particle. Finally, we study the lowest-frequency vibration of the $B = 7$ Skyrmion, leading to a suggestion that the surprisingly low energy of the Lithium-7/Beryllium-7 spin $\frac{3}{2}$ ground state may be in part due to an isospin Coriolis effect.

2.2 Quantization of Skyrmions

2.2.1 Skyrme Lagrangian

Skyrmions are static soliton solutions to the field equations associated with the Skyrme Lagrangian. In more detail, pion fields $\pi(x,t)$ are combined into an $SU(2)$-valued field on spacetime $U : \mathbb{R}^4 \to SU(2)$

$$U(x,t) = \sigma(x,t)\mathbb{I}_2 + i\pi(x,t) \cdot \tau \tag{2.1}$$

and the Lagrangian defining the classical field theory is (in Skyrme units)

$$L = \int d^3x \left[\frac{1}{2}\mathrm{Tr}(L_\mu L^\mu) + \frac{1}{16}\mathrm{Tr}([L_\mu, L_\nu][L^\mu, L^\nu]) + m^2 Tr(U - \mathbb{I}_2) \right] \tag{2.2}$$

with $L_\mu = U^\dagger \partial_\mu U$. Isospin symmetry corresponds to transformations $U \to C^\dagger U C$ for any constant matrix $C \in SU(2)$. Skyrmions are classified by an integer $B \in \mathbb{Z}$ which is identified with the baryon number of the nucleus. The integer B is conserved as a consequence of boundary conditions: we demand that

$$U \to \mathbb{I}_2 \tag{2.3}$$

at spatial infinity which means that the static field U can be regarded as a continuous map from the one-point compactification S^3 of spatial $\mathbb{R}^3$, i.e. $U : S^3 \to S^3$. Such maps are classified by a homotopy class $B \in \pi_3(S^3) \cong \mathbb{Z}$ which is preserved under continuous time evolution. We will see explicit examples of Skyrmions in Section 2.4 and Section 2.5.

2.2.2 Restricted configuration space

Given a Skyrmion, we are often interested in constructing a restricted configuration space $\mathcal{C}$ of deformations. $\mathcal{C}$ should in principle capture the field configurations which are relevant at low energies. A natural first choice is given by the rigid-body approximation: only rotations

and isorotations of the Skyrmion are included. One then quantizes geodesic motion on the corresponding submanifold $\mathcal{C} \simeq SU(2) \times SU(2)$ with respect to the metric induced from the full field theory. The resulting problem is equivalent to a (generalised) rigid rotor, with quantum states classified by spin and isospin. Comparisons to nuclear data have been promising in many cases, but recent work suggests that to model real nuclei it is necessary to take additional deformations of the Skyrmion into account: we need to include more than just the zero modes.

One can study vibrations of Skyrmions and find their normal modes [11]. Then a natural next step beyond rigid-body quantization is to include those modes with the lowest non-zero frequency (the first N of them, say). Within a harmonic approximation we can think of the resulting configuration space as $\mathcal{C} \simeq SU(2) \times SU(2) \times \mathbb{R}^N$. More generally we may be interested in larger collective motions (not just small vibrations). For example, in [7] Oxygen-16 was modelled by motion on $\mathcal{C} \simeq SU(2) \times SU(2) \times \mathcal{M}$ with $\mathcal{M}$ a quotient of a six-punctured sphere.

The examples given so far have the product structure $\mathcal{C} \simeq SU(2) \times SU(2) \times \mathcal{C}_{\text{shapes}}$, but one could imagine a restricted configuration space $\mathcal{C}$ which includes zero modes (generated by $SU(2) \times SU(2)$) but which is not globally a product of the above form. $\mathcal{C}$ should really be thought of as a principal $SU(2) \times SU(2)$-bundle, with rotations and isorotations generating the fibres. Locally it will be a product but this might not be true globally.

2.2.3 Quantum Hamiltonian

For clarity, we will at first ignore isorotations. Our configuration space comes with an action of the rotational symmetry group $SU(2)$, and we can think of the configuration space $\mathcal{C}$ as a principal $SU(2)$-bundle

$$\pi : \mathcal{C} \to \mathcal{C}_{\text{shapes}}$$

with rotations generating the fibres. For every point in the base space $\mathcal{C}_{\text{shapes}}$ (which we will refer to as shape space) there is an open neighbourhood $V \subseteq \mathcal{C}_{\text{shapes}}$ containing the point such that $\pi^{-1}(V)$ can be identified with $SU(2) \times V$ (one should think of this identification as making a particular choice of reference orientation for each fibre). Working locally, we think of a point in configuration space as a pair (θ_i, s_j) with s_j, the coordinates on $V \subseteq \mathcal{C}_{\text{shapes}}$, specifying the shape of the field configuration and with θ_i Euler angles parametrising its orientation in space.

Our configuration space inherits a metric $\tilde{g}$ from the full Skyrme field theory. $SU(2)$ symmetry implies that this inherited metric must be symmetric under (left) translations in

the $SU(2)$ factor. Thus the most general form of the inherited metric is

$$\tilde{g} = \begin{pmatrix} \sigma & ds_i \end{pmatrix} \begin{pmatrix} \Lambda & \Lambda \mathbf{A}_j \\ \mathbf{A}_i^T \Lambda & g_{ij} + \mathbf{A}_i \cdot \Lambda \cdot \mathbf{A}_j \end{pmatrix} \begin{pmatrix} \sigma \\ ds_j \end{pmatrix} \tag{2.4}$$

where the $\sigma = (\sigma_1, \sigma_2, \sigma_3)$ are left-invariant one forms on $SU(2)$ and where Λ, $\mathbf{A}_i$ and g_{ij} only depend on the shape coordinates s_i. Note that we have suppressed the index on σ, that Λ is a 3×3 matrix, and that a bold font is used to indicate that $\mathbf{A}_i$ is a 3-component vector for each i. The suggestive notation $\mathbf{A}_j$ has been used as it will turn out that this corresponds to a particular connection on the principal bundle $\mathcal{C}$.

We now construct a quantum Hamiltonian by computing the Laplace-Beltrami operator on $\mathcal{C}$. Recall that the Laplace-Beltrami operator Δ corresponding to a metric G has an expression in local coordinates

$$\Delta f = \frac{1}{\sqrt{|G|}} \partial_i \left(\sqrt{|G|} G^{ij} \partial_j f \right). \tag{2.5}$$

For the calculation of Δ it is useful to note that $\tilde{g}$ can be rewritten as

$$\tilde{g} = \begin{pmatrix} d\theta & ds_i \end{pmatrix} G \begin{pmatrix} d\theta \\ ds_j \end{pmatrix} \tag{2.6}$$

(here we closely follow [10]) where

$$G = \begin{pmatrix} \lambda^T & 0 \\ \mathbf{A}_i^T & I \end{pmatrix} \begin{pmatrix} \Lambda & 0 \\ 0 & g_{ij} \end{pmatrix} \begin{pmatrix} \lambda & \mathbf{A}_j \\ 0 & I \end{pmatrix}. \tag{2.7}$$

λ is the matrix which captures the relationship between the left-invariant one forms σ and the (coordinate) one forms $d\theta$. Thus we can compute $|G| = |\lambda|^2 |\Lambda| |g_{ij}|$ and then use the expression (2.5) to obtain a quantum Hamiltonian

$$\mathcal{H} = \frac{1}{2} \mathbf{L} \cdot \Lambda^{-1} \cdot \mathbf{L} + \frac{1}{2} (p_i - \mathbf{L} \cdot \mathbf{A}_i) g_{ij}^{-1} (p_j - \mathbf{L} \cdot \mathbf{A}_j) + V_2(s) + V(s) \tag{2.8}$$

where we have included both the kinetic term $-\hbar^2 \Delta$ and a potential $V(s)$ on configuration space. $\mathbf{L}$ is the (usual) body-fixed angular momentum operator familiar from rigid-body theory ($\mathbf{J}$ will denote the space-fixed angular momentum operator) and $p_i = -i\hbar \frac{\partial}{\partial s_i}$. Also appearing in the kinetic term is

$$V_2(s) = \frac{\hbar^2}{2} (|\Lambda| |g_{ij}|)^{-\frac{1}{4}} \partial_i \left(g_{ij}^{-1} \partial_j (|\Lambda| |g_{ij}|)^{\frac{1}{4}} \right). \tag{2.9}$$

11

2.2.4 Effective problem on $\mathcal{C}_{\text{shapes}}$

Exploiting rotational symmetry, we can classify the energy eigenstates of (2.8) by J (where $J(J+1)$ is the eigenvalue of $\mathbf{J}^2$ in the usual way) and J_3. Recall from rigid-body theory that a complete set of commuting operators for the rotational part of the problem is given by $\mathbf{J}^2, J_3, L_3$ and so within a particular (J, J_3) sector we can expand the total wavefunction

$$\Psi = \sum_{L_3=-J}^{+J} \chi_{L_3}(s) \left| J J_3 L_3 \right\rangle. \tag{2.10}$$

Within this sector, we see that Ψ can be thought of as a complex vector-valued function

$$\begin{pmatrix} \chi_{-J}(s) \\ \vdots \\ \chi_J(s) \end{pmatrix}$$

on $V \subseteq \mathcal{C}_{\text{shapes}}$. Of course, we have only been working locally, i.e. in some patch of $\mathcal{C}$ which looks like a product $SU(2) \times V$. The total wavefunction, defined on all of $\mathcal{C}$, isn't a vector-valued *function* on the base space but is more precisely a *section* of a (complex) vector bundle of rank $2J+1$. These two notions coincide for the case of trivial bundles. In the more general case, we would work with functions in separate patches and then impose appropriate conditions on the overlaps to ensure they give a genuine section. An explicit example of this process will be given in Chapter 5.

Given the expansion for Ψ above, we obtain the Schrödinger equation

$$\frac{1}{2} \mathbf{L} \cdot \Lambda^{-1} \cdot \mathbf{L} \begin{pmatrix} \chi_{-J}(s) \\ \vdots \\ \chi_J(s) \end{pmatrix} + \frac{1}{2} \left(p_i - \mathbf{L} \cdot \mathbf{A}_i \right) g_{ij}^{-1} \left(p_j - \mathbf{L} \cdot \mathbf{A}_j \right) \begin{pmatrix} \chi_{-J}(s) \\ \vdots \\ \chi_J(s) \end{pmatrix} \tag{2.11}$$

$$+ \left(V_2(s) + V(s) - E \right) \begin{pmatrix} \chi_{-J}(s) \\ \vdots \\ \chi_J(s) \end{pmatrix} = 0$$

where now the operators $\mathbf{L}$ act by matrix multiplication. This is the effective problem on $\mathcal{C}_{\text{shapes}}$. It is equivalent to the motion of a particle on $\mathcal{C}_{\text{shapes}}$ coupled to an $SU(2)$ gauge field, with the particle transforming in the $(2J + 1)$-dimensional irrep of the gauge group and with the gauge field (or connection) corresponding to $\mathbf{A}_i$. Gauge transformations are equivalent to redefining our choice of reference orientation for each $s \in \mathcal{C}_{\text{shapes}}$.

Note that the rotational motion influences the motion on $\mathcal{C}_{\text{shapes}}$ through the familiar minimal coupling $p_j - \mathbf{L} \cdot \mathbf{A}_j$ of the momentum p_j to the gauge field. To completely separate

out rotational motion would require us to find a gauge where $\mathbf{A}_i$ vanishes. $\mathbf{A}_i$, while gauge dependent, has gauge-invariant properties such as (possibly non-vanishing) curvature. The curvature of $\mathbf{A}_i$ can therefore be viewed as an obstruction to complete separation of rotational motion from the other degrees of freedom.

2.2.5 Including isospin

The above derivation is easily modified to include the possibility of isospin. Once again the metric must take the form

$$\tilde{g} = \begin{pmatrix} \sigma & ds_i \end{pmatrix} \begin{pmatrix} \Lambda & \Lambda \mathbf{A}_j \\ \mathbf{A}_i^T \Lambda & g_{ij} + \mathbf{A}_i \cdot \Lambda \cdot \mathbf{A}_j \end{pmatrix} \begin{pmatrix} \sigma \\ ds_j \end{pmatrix} \tag{2.12}$$

where now $\sigma = \left(\sigma_1^J, \sigma_2^J, \sigma_3^J, \sigma_1^I, \sigma_2^I, \sigma_3^I\right)$ includes both left-invariant one forms $\left(\sigma_1^J, \sigma_2^J, \sigma_3^J\right)$ associated with rotations and $\left(\sigma_1^I, \sigma_2^I, \sigma_3^I\right)$ associated with isorotations. Λ and $\mathbf{A}_i$ have now become a 6×6 matrix and (for each i) a 6-component vector respectively. One ends up with the Hamiltonian

$$\mathcal{H} = \frac{1}{2} \begin{pmatrix} \mathbf{L} \\ \mathbf{K} \end{pmatrix} \cdot \Lambda^{-1} \cdot \begin{pmatrix} \mathbf{L} \\ \mathbf{K} \end{pmatrix} + \frac{1}{2} \left(p_i - \begin{pmatrix} \mathbf{L} \\ \mathbf{K} \end{pmatrix} \cdot \mathbf{A}_i \right) g_{ij}^{-1} \left(p_j - \begin{pmatrix} \mathbf{L} \\ \mathbf{K} \end{pmatrix} \cdot \mathbf{A}_j \right) + V_2 + V \tag{2.13}$$

where

$$V_2(s) = \frac{\hbar^2}{2} \left(|\Lambda| \, |g_{ij}|\right)^{-\frac{1}{4}} \partial_i \left(g_{ij}^{-1} \partial_j \left(|\Lambda| \, |g_{ij}|\right)^{\frac{1}{4}} \right). \tag{2.14}$$

We will make use of this Hamiltonian later. For now, we will go back to only including rotations.

2.3 Equilateral triangle in $\mathbb{R}^3$

We will be interested in small vibrations of Skyrmions, ultimately applying the above ideas to the quantization of the $B = 4$ and $B = 7$ Skyrmions. But let us start with a simpler problem which illustrates the main ideas: as a model for a Skyrmion, consider an equilateral triangular arrangement of point particles in $\mathbb{R}^3$, with particle i having unit mass and position vector $\mathbf{r}_i$. We imagine these are attached by identical springs.

This (equilateral) arrangement has symmetry group D_{3h}, and so its vibrations can be classified by irreps of this group. There are three normal modes (not including zero modes), which split into the irreps $A \oplus E'$ under the action of D_{3h}. For the spring model, the E' vibration has the lowest frequency with $\frac{\omega_{E'}}{\omega_A} = \frac{1}{\sqrt{2}}$. Suppose we are interested in a configuration space $\mathcal{C} \simeq SO(3) \times \mathbb{R}^2$ which includes only this doubly-degenerate vibration (E') together with rotations. This is clearly a trivial bundle. We will use coordinates $\mathbf{s} = (s_1, s_2)$

on C_{shapes}, and Euler angles θ^i to specify orientation. Let d be the distance from each particle to the centre of mass in the equilibrium configuration, and work in units where $\hbar = 1$, $d = 1$. Let the coordinates $(\theta^i = 0, \mathbf{s})$ correspond to the configuration

$$
\mathbf{r}_1 = \begin{pmatrix} 0 \\ 1 \\ 0 \end{pmatrix} + s_1 \begin{pmatrix} 0 \\ \frac{1}{\sqrt{3}} \\ 0 \end{pmatrix} + s_2 \begin{pmatrix} \frac{1}{\sqrt{3}} \\ 0 \\ 0 \end{pmatrix} \tag{2.15}
$$

$$
\mathbf{r}_2 = \begin{pmatrix} \frac{\sqrt{3}}{2} \\ -\frac{1}{2} \\ 0 \end{pmatrix} + s_1 \begin{pmatrix} -\frac{1}{2} \\ -\frac{1}{2\sqrt{3}} \\ 0 \end{pmatrix} + s_2 \begin{pmatrix} -\frac{1}{2\sqrt{3}} \\ \frac{1}{2} \\ 0 \end{pmatrix} \tag{2.16}
$$

$$
\mathbf{r}_3 = \begin{pmatrix} -\frac{\sqrt{3}}{2} \\ -\frac{1}{2} \\ 0 \end{pmatrix} + s_1 \begin{pmatrix} \frac{1}{2} \\ -\frac{1}{2\sqrt{3}} \\ 0 \end{pmatrix} + s_2 \begin{pmatrix} -\frac{1}{2\sqrt{3}} \\ -\frac{1}{2} \\ 0 \end{pmatrix}. \tag{2.17}
$$

This is our gauge choice. A general configuration $(\theta^i, \mathbf{s})$ with $\theta^i \neq 0$ can be deduced from a rotation of the corresponding reference configuration $(0, \mathbf{s})$. We will assume $V(\mathbf{s}) = \frac{1}{2}\omega^2 \mathbf{s}^2$. We can compute the metric induced from the Euclidean metric on $\mathbb{R}^9$ (three point particles) which leads, by comparison to the expression

$$
\tilde{g} = \begin{pmatrix} \sigma & ds_i \end{pmatrix} \begin{pmatrix} \Lambda & \Lambda \mathbf{A}_j \\ \mathbf{A}_i^T \Lambda & g_{ij} + \mathbf{A}_i \cdot \Lambda \cdot \mathbf{A}_j \end{pmatrix} \begin{pmatrix} \sigma \\ ds_j \end{pmatrix}, \tag{2.18}
$$

to

$$
\Lambda = \begin{pmatrix} \frac{3}{2} + \sqrt{3}s_1 + \frac{1}{2}\left(s_1^2 + s_2^2\right) & -\sqrt{3}s_2 & 0 \\ -\sqrt{3}s_2 & \frac{3}{2} - \sqrt{3}s_1 + \frac{1}{2}\left(s_1^2 + s_2^2\right) & 0 \\ 0 & 0 & 3 + s_1^2 + s_2^2 \end{pmatrix}, \tag{2.19}
$$

$$
g_{ij} = \frac{1}{3 + s_1^2 + s_2^2} \begin{pmatrix} 3 + s_1^2 & s_1 s_2 \\ s_1 s_2 & 3 + s_2^2 \end{pmatrix}, \tag{2.20}
$$

and

$$
\mathbf{A}_1 = \begin{pmatrix} 0 \\ 0 \\ \frac{s_2}{3 + s_1^2 + s_2^2} \end{pmatrix} \qquad \mathbf{A}_2 = \begin{pmatrix} 0 \\ 0 \\ -\frac{s_1}{3 + s_1^2 + s_2^2} \end{pmatrix}. \tag{2.21}
$$

14

We can already see that the gauge field takes a familiar form for small (s_1, s_2): we have

$$\mathbf{A}_1 \sim \begin{pmatrix} 0 \\ 0 \\ \frac{s_2}{3} \end{pmatrix}, \mathbf{A}_2 \sim \begin{pmatrix} 0 \\ 0 \\ -\frac{s_1}{3} \end{pmatrix} \tag{2.22}$$

and so the effective motion on $\mathcal{C}_{\text{shapes}}$ will appear as if coupled to a constant magnetic field (of strength $\frac{1}{3}L_3$) pointing out of the (s_1, s_2)-plane. For this example, it is also simple to compute

$$
\begin{aligned}
V_2(s) &= \frac{1}{2} \left(|\Lambda|\, |g_{ij}|\right)^{-\frac{1}{4}} \partial_i \left(g_{ij}^{-1} \partial_j \left(|\Lambda|\, |g_{ij}|\right)^{\frac{1}{4}} \right) \\
&= \frac{1}{2} \frac{-6 + s_1^2 + s_2^2}{\left(3 - s_1^2 - s_2^2\right)^2}.
\end{aligned} \tag{2.23}
$$

Recall that the full quantum Hamiltonian is

$$\mathcal{H} = \frac{1}{2}\mathbf{L} \cdot \Lambda^{-1} \cdot \mathbf{L} + \frac{1}{2}\left(p_i - \mathbf{L} \cdot \mathbf{A}_i\right) g_{ij}^{-1} \left(p_j - \mathbf{L} \cdot \mathbf{A}_j\right) + V_2(s) + V(s). \tag{2.24}$$

We now make the following approximation: assume that the vibrational frequency ω is large so that the most important terms in the above Hamiltonian give a harmonic oscillator

$$\mathcal{H}_0 = \frac{1}{2}\left(p_1^2 + p_2^2\right) + \frac{1}{2}\omega^2 \left(s_1^2 + s_2^2\right). \tag{2.25}$$

We will expand the full Hamiltonian in $\frac{1}{\omega}$, keeping the leading corrections to the $\mathcal{H}_0$ system. Note that $\mathcal{H}_0$ has eigenvalues $\sim \omega$. Also note that, schematically, $s^2 \sim \frac{1}{\omega}$ and $p^2 \sim \omega$ for the harmonic oscillator from which the orders of other terms in $\mathcal{H}$ can be deduced. Expanding out the full Hamiltonian, we have

$$\mathcal{H} = \underbrace{\mathcal{H}_0}_{\sim \omega^1} + \underbrace{\frac{1}{3}\left(\mathbf{L}^2 - \frac{1}{2}L_3^2\right) + \frac{1}{3}L_3 J_s + \frac{1}{6}J_s^2 - \frac{1}{3}}_{\sim \omega^0} + \underbrace{\cdots}_{\sim \text{higher}} \tag{2.26}$$

where $J_s = s_1 p_2 - s_2 p_1$ is an operator which will be referred to as the vibrational angular momentum. To this order, the only effect of $V_2(s)$ is to contribute an additive constant (here, $-\frac{1}{3}$) to the Hamiltonian. This will be the case more generally and so we will neglect $V_2(s)$ in later examples. So the terms that remain are $\mathcal{H}_0$ (a harmonic oscillator corresponding to vibrations), $\frac{1}{3}\left(\mathbf{L}^2 - \frac{1}{2}L_3^2\right)$ (the familiar rigid-body Hamiltonian, corresponding to rotations) and finally the term $\frac{1}{3}L_3 J_s + \frac{1}{6}J_s^2$ which comes from the gauge field. It gives the leading correction due to rotation-vibration coupling. This is referred to as a *Coriolis term* in the molecular physics literature.

2.3.1 Symmetry arguments

Before moving on, let's reflect on what we have done in this example. The coordinates $(\theta^i, \mathbf{s})$ were actually carefully chosen so that the metric took the form

$$
\tilde{g} = \begin{pmatrix} \sigma & ds_i \end{pmatrix} \begin{pmatrix} \Lambda_0 & \Lambda_0 \mathbf{A}_j \\ \mathbf{A}_i^T \Lambda_0 & \delta_{ij} \end{pmatrix} \begin{pmatrix} \sigma \\ ds_j \end{pmatrix} \tag{2.27}
$$

where to the order we are interested in, $\Lambda = \Lambda_0$ a constant matrix (the moment of inertia tensor for the equilibrium configuration) and the bottom-right entry is δ_{ij} (normal coordinates for the vibration) and the off-diagonal entry $\Lambda \mathbf{A}_i$ vanishes at the equilibrium configuration (this says that rotations and vibrations are orthogonal at the equilibrium configuration). Then, to the order we are interested in, $\mathbf{A}_i$ is linear in the shape coordinates.

Now recall that the equilibrium configuration has D_{3h} symmetry and that the vibration we are interested in transforms in the E' representation of D_{3h}, $\rho_{\text{vib}} \cong E'$. In particular, the metric $\tilde{g}$ enjoys a D_{3h} symmetry and so the gauge field $\mathbf{A}_i$ is not just an *arbitrary* linear function of the shape coordinates but corresponds to a singlet of D_{3h} under an action of D_{3h} isomorphic to $\rho_{\text{vib}} \otimes \rho_{\text{vib}} \otimes \rho_{\text{rot}}$ where ρ_{rot} denotes the representation in which rotations (R_x, R_y, R_z) transform under D_{3h} (for our example $\rho_{\text{rot}} = A_2' \oplus E''$). This observation is equivalent to *Jahn's rule*, which is known in molecular physics as a necessary condition for the existence of non-trivial first-order Coriolis terms [12]. In the present case, a simple character theory calculation shows that $\rho_{\text{vib}} \otimes \rho_{\text{vib}} \otimes \rho_{\text{rot}}$ contains precisely one copy of the trivial irrep of D_{3h}. So the gauge field $\mathbf{A}_i$ is determined by a single constant η. It has to transform trivially under $\rho_{\text{vib}} \otimes \rho_{\text{vib}} \otimes \rho_{\text{rot}}$, which in this case means that the $\mathbf{A}_i$ must satisfy

$$
\forall g \in D_{3h} : \rho_{\text{rot}}(g)\, (\rho_{\text{vib}}(g))_{ik}\, \mathbf{A}_k \left((\rho_{\text{vib}}(g))_{jl}^{-1} s_l \right) = \mathbf{A}_i(s_j) \tag{2.28}
$$

so that

$$
\mathbf{A}_1 = \eta \begin{pmatrix} 0 \\ 0 \\ s_2 \end{pmatrix} \qquad \mathbf{A}_2 = \eta \begin{pmatrix} 0 \\ 0 \\ -s_1 \end{pmatrix}. \tag{2.29}
$$

The only reason to do the explicit calculation of the previous section was to determine that $\eta = \frac{1}{3}$. We might more generally take η to be a free parameter. This insight will prove useful in situations where it is not so easy to compute the gauge field explicitly, and all we have is knowledge of the relevant symmetry group together with the transformation properties of the vibration.
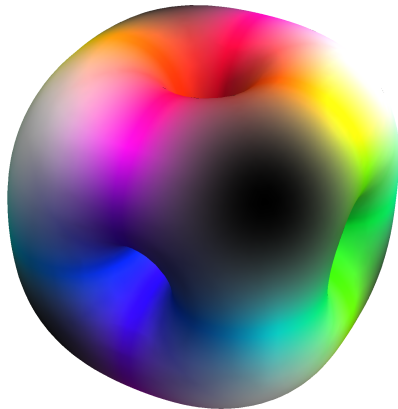
Figure 2.1: B=4 Skyrmion with O_h symmetry. Figure courtesy of Dankrad Feist.

2.4 $B = 4$ Skyrmion and the α-particle

We now apply our insights from the previous section to the problem of a vibrating and rotating Skyrmion. The minimal energy $B = 4$ Skyrmion has O_h symmetry and is illustrated in Figure 2.1. The isospin 0 quantum states of this Skyrmion correspond to the α-particle. In [13] the authors performed rigid-body quantization of the O_h-symmetric $B = 4$ Skyrmion, finding a ground state with spin $J = 0$ and a first excited state with $J = 4$. The spin 4 excitation (at roughly 40 MeV) has not yet been experimentally observed. In addition, there are numerous observed excited states with lower spin in the $20 - 30$ MeV range [14] which are not captured by the rigid-body picture. The O_h symmetry group of the rigid $B = 4$ Skyrmion is too large to allow such excitations (which have spins 0, 1 and 2) and so the data suggests that vibrations must be included if we want to describe these states.

2.4.1 Vibrations of the $B = 4$ Skyrmion

The lowest four vibrational modes [11, 15] of the $B = 4$ O_h-symmetric Skyrmion are listed in Table 2.1. The associated frequencies are those calculated in [11] for a dimensionless pion mass of $m = 1$. These vibrations have been classified using O_h representation theory. As a group, O_h is generated by a 3-fold rotation C_3, 4-fold rotation C_4 together with an inversion element $-I$. O_h has 10 irreps with the corresponding character table given in Table 2.2. Following a similar approximation scheme to the previous section, we aim to compute the quantum spectrum of a vibrating and rotating $B = 4$ Skyrmion. We assume that the vibrations in Table 2.1 are the most important and neglect any other degrees of freedom. We will ignore isorotations as we are interested in isospin 0 states corresponding to the α-particle. (We will include isorotations when we look at the $B = 7$ Skyrmion in the next section).

Frequency	Irrep of O_h	Description
0.46	E^+	Two opposite faces pull away from each other to form two $B = 2$ tori. In the other direction, four edges pull away to become four $B = 1$ Skyrmions.
0.48	F_2^+	An opposing pair of square-symmetric faces deform to become rhombus-shaped.
0.52	A_2^-	Four vertices of the cube pull away, retaining tetrahedral symmetry. These then come in again and the other four vertices pull away to form the dual tetrahedron.
0.62	F_2^-	Two opposite edges from the same face pull away from the origin. On the opposite face, the perpendicular edges also pull away.

Table 2.1: Vibrations of $B = 4$ Skyrmion. Frequencies (in Skyrme units) and descriptions from [11].

O_h	E	$8C_3$	$6C_2$	$6C_4$	$3C_2 = (C_4)^2$	i	$6S_4$	$8S_6$	$3\sigma_h$	$6\sigma_d$
A_1^+	1	1	1	1	1	1	1	1	1	1
A_2^+	1	1	-1	-1	1	1	-1	1	1	-1
E^+	2	-1	0	0	2	2	0	-1	2	0
F_1^+	3	0	-1	1	-1	3	1	0	-1	-1
F_2^+	3	0	1	-1	-1	3	-1	0	-1	1
A_1^-	1	1	1	1	1	-1	-1	-1	-1	-1
A_2^-	1	1	-1	-1	1	-1	1	-1	-1	1
E^-	2	-1	0	0	2	-2	0	1	-2	0
F_1^-	3	0	-1	1	-1	-3	-1	0	1	1
F_2^-	3	0	1	-1	-1	-3	1	0	1	-1

Table 2.2: O_h character table [16].

2.4.2 The F_2^- vibration

To start, we consider just the triply degenerate F_2^- vibration of the $B = 4$ Skyrmion along with rotations, $\mathcal{C} \simeq SU(2) \times \mathbb{R}^3$. As in the case of the equilateral triangle, we assume the vibrations are small. The equilibrium configuration has symmetry group O_h, which acts on physical space as follows:

$$C_4 : (x, y, z) \to (-y, x, z)$$

$$C_3 : (x, y, z) \to (y, z, x) \tag{2.30}$$

$$-I : (x, y, z) \to (-x, -y, -z).$$

Note that this action of O_h is isomorphic to F_1^-. Introduce coordinates $(\theta^i, \mathbf{s})$ such that the total metric takes the form (to the order we are interested in)

$$\tilde{g} = \begin{pmatrix} \sigma & ds_i \end{pmatrix} \begin{pmatrix} \Lambda_0 & \Lambda_0 \mathbf{A}_i \\ \mathbf{A}_i^T \Lambda_0 & \delta_{ij} \end{pmatrix} \begin{pmatrix} \sigma \\ ds_j \end{pmatrix} \tag{2.31}$$

with

$$\Lambda_0 = \begin{pmatrix} \mathcal{I} & 0 & 0 \\ 0 & \mathcal{I} & 0 \\ 0 & 0 & \mathcal{I} \end{pmatrix}, \tag{2.32}$$

$\mathbf{A}_i$ linear and vanishing at the equilibrium configuration $s_1 = s_2 = s_3 = 0$. We still have some freedom in which vibrational coordinates $\mathbf{s} = (s_1, s_2, s_3)$ we choose, and we will choose them so that they transform under O_h as follows:

$$C_4 : (s_1, s_2, s_3) \to (s_2, -s_1, -s_3)$$

$$C_3 : (s_1, s_2, s_3) \to (s_2, s_3, s_1) \tag{2.33}$$

$$-I : (s_1, s_2, s_3) \to (-s_1, -s_2, -s_3).$$

Note at this point that, unlike in the point particle example of the previous section, we do not have explicit expressions for the Skyrme field configurations corresponding to each $\mathbf{s} = (s_1, s_2, s_3)$. However, it is always possible to pick coordinates so that the action of O_h is realised exactly as above (since the representation ρ_{vib} of O_h given in (2.33) is indeed isomorphic to F_2^-). As in the point particle model of the previous section, it turns out that $\rho_{\text{vib}} \otimes \rho_{\text{vib}} \otimes \rho_{\text{rot}} = F_2^- \otimes F_2^- \otimes F_1^+$ contains precisely one singlet, and that the gauge field is

therefore determined up to a single multiplicative scalar η_-:

$$\mathbf{A}_1 = \tfrac{\eta_-}{2\mathcal{I}} \begin{pmatrix} 0 \\ -s_3 \\ s_2 \end{pmatrix} \qquad \mathbf{A}_2 = \tfrac{\eta_-}{2\mathcal{I}} \begin{pmatrix} s_3 \\ 0 \\ -s_1 \end{pmatrix} \qquad \mathbf{A}_3 = \tfrac{\eta_-}{2\mathcal{I}} \begin{pmatrix} -s_2 \\ s_1 \\ 0 \end{pmatrix}. \tag{2.34}$$

Substituting this into the general expression in (2.24), we arrive at the Hamiltonian

$$\mathcal{H} \approx \frac{1}{2}\mathbf{p}^2 + \frac{1}{2}\omega_{F_2^-}^2 \mathbf{s}^2 + \frac{1}{2\mathcal{I}}\mathbf{L}^2 - \frac{\eta_-}{2\mathcal{I}}\mathbf{L}\cdot\mathbf{J_s} + \frac{\eta_-^2}{8\mathcal{I}}\mathbf{J_s}^2 \tag{2.35}$$

where $p_i = -i\hbar\frac{\partial}{\partial s_i}$ and $\mathbf{J_s} = \mathbf{s}\times\mathbf{p}$. A similar picture to that in equation (2.26) emerges: we have a harmonic oscillator system and a rigid-body system which are coupled through the additional term $-\frac{\eta_-}{2\mathcal{I}}\mathbf{L}\cdot\mathbf{J_s} + \frac{\eta_-^2}{8\mathcal{I}}\mathbf{J_s}^2$ involving the usual body-fixed angular momentum $\mathbf{L}$ and a vibrational angular momentum $\mathbf{J_s}$. In principle η_- could be calculated from the Skyrme model given explicit Skyrme field configurations, much like how we calculated $\eta = \frac{1}{3}$ in the preceding (point particle) example. We will take it to be a free parameter.

2.4.3 Computing the spectrum

We are interested in the Hamiltonian

$$\mathcal{H} = \frac{1}{2}\mathbf{p}^2 + \frac{1}{2}\omega_{F_2^-}^2 \mathbf{s}^2 + \frac{1}{2I}\mathbf{L}^2 - \frac{\eta_-}{2I}\mathbf{L}\cdot\mathbf{J_s} + \frac{\eta_-^2}{8I}\mathbf{J_s}^2. \tag{2.36}$$

It will help to rewrite the Hamiltonian using the fact that, as $\mathbf{J_s}$ and $\mathbf{L}$ commute,

$$\mathbf{L}\cdot\mathbf{J_s} = \frac{1}{2}\mathbf{L}^2 + \frac{1}{2}\mathbf{J_s}^2 - \frac{1}{2}\mathbf{M}^2 \tag{2.37}$$

where we have introduced a new angular momentum operator $\mathbf{M} = \mathbf{J_s} - \mathbf{L}$. (Note that $-\mathbf{L}$, not $+\mathbf{L}$, obeys the usual angular momentum commutation relations: $\mathbf{L}$ is the vector of *body-fixed* angular momentum operators so its commutation relations differ by a minus sign compared to *space-fixed* angular momentum operators). Then

$$\mathcal{H} = \frac{1}{2}\mathbf{p}^2 + \frac{1}{2}\omega_{F_2^-}^2 \mathbf{s}^2 + \left(\frac{1}{2\mathcal{I}} - \frac{\eta_-}{4\mathcal{I}}\right)\mathbf{L}^2 + \frac{\eta_-}{4\mathcal{I}}\mathbf{M}^2 + \left(\frac{\eta_-^2}{8\mathcal{I}} - \frac{\eta_-}{4\mathcal{I}}\right)\mathbf{J_s}^2. \tag{2.38}$$

Energy eigenstates Ψ can be classified by $\mathbf{M}^2, \mathbf{J_s}^2, \mathbf{L}^2$ and the vibrational phonon-number $N_{F_2^-}$, and additionally by their transformation under the O_h symmetry group, where O_h acts on a state by transforming the vibrational coordinates, and then performing a compensating rotation:

$$\Psi \to \rho_{\text{rot}}(g) \otimes \rho_{\text{vib}}(g)\,\Psi. \tag{2.39}$$

Explicitly, this action is generated by

$$C_4 : \Psi \to P e^{-\frac{2\pi i}{4}\mathbf{n}_4 \cdot \mathbf{M}}\Psi$$

$$C_3 : \Psi \to e^{-\frac{2\pi i}{3}\mathbf{n}_3 \cdot \mathbf{M}}\Psi \tag{2.40}$$

$$-I : \Psi \to P\Psi$$

where $\mathbf{n}_4 = \begin{pmatrix} 0 \\ 0 \\ 1 \end{pmatrix}$, $\mathbf{n}_3 = \frac{1}{\sqrt{3}}\begin{pmatrix} -1 \\ -1 \\ -1 \end{pmatrix}$ and where P is the parity operation on the vibrational coordinates $\mathbf{s} \to -\mathbf{s}$.

Finkelstein-Rubinstein constraints restrict the allowed quantum states. They come from requiring that the $B = 1$ Skyrmion (whose quantum states give rise to the proton/neutron isodoublet) is quantized as a fermion, and involve working out whether the symmetries of the classical Skyrme field configurations correspond to contractible or non-contractible loops, as explained in [17]. They have been worked out in detail [18] for all the minimal-energy Skyrmions we will be interested in, within the context of rigid-body quantization. Actually we are interested in *vibrations* which take us away from the minimal-energy Skyrmions. So long as these vibrations are small, it is clear that the F-R constraints follow from the rigid-body constraints by a simple continuity argument.

In the present case, the F-R constraints are that physical states should be taken to transform trivially under the action of $\langle C_4, C_3 \rangle \cong O \le O_h$, the subgroup consisting of rotations. Recall $O_h \cong O \times \mathbb{Z}_2$, a direct product of groups, with $\mathbb{Z}_2$ the subgroup generated by the parity operation $-I \in O_h$. So such representations fall into two classes, A_1^+ or A_1^-, depending on their transformation under the $\mathbb{Z}_2$. This determines the parity of the state as $+$ or $-$. Within each fixed $\mathbf{M}^2, \mathbf{J}_{\mathbf{s}}^2, \mathbf{L}^2, N_{F_2^-}$ sector, we compute the character of the action of O_h and then look for representations of type A_1.

As an example, suppose we are interested in one-phonon states (i.e. states with one quantum of vibrational energy). Such states have $J_{\mathbf{s}} = 1$. We might look for states with $J = L = 2$. Adding these angular momenta, we have several possibilities for the total angular momentum $M = J_{\mathbf{s}} - L = 3, 2, 1$. So, if we are interested say in $M = 3$, we have narrowed down to a seven-dimensional subspace. We now look at how this seven-dimensional subspace transforms under the action above, computing the associated character χ. We then find that $\langle \chi, A_1^+ \rangle = 0$ and $\langle \chi, A_1^- \rangle = 1$ giving a single negative parity 2^- state.

2.4.4 Other vibrations

We now include the vibrations transforming as F_2^-, F_2^+, A_2^-, treating the vibrational frequencies as free parameters, and fit the resulting spectrum to data in the < 30 MeV range. We

could also include the E^+ vibration but it turns out that including it gives no improvement to the fit to experimental data. In fact it will turn out that almost all of the data can be explained solely in terms of F_2^- and F_2^+ modes, with a higher frequency A_2^- mode important for a couple of higher energy (~ 28 MeV) states. The F_2^- and F_2^+ can have Coriolis terms whereas symmetry considerations exclude any non-trivial Coriolis term for the A_2^-. This leads to the Hamiltonian

$$
\begin{aligned}
\mathcal{H} \;=\; & \frac{1}{2}\mathbf{p_s}^2 + \frac{1}{2}\omega_{F_2^-}^2 \mathbf{s}^2 + \frac{1}{2}\mathbf{p_t}^2 + \frac{1}{2}\omega_{F_2^+}^2 \mathbf{t}^2 + \frac{1}{2}p_u^2 + \frac{1}{2}\omega_{A_2^-}^2 u^2 \\
& + \frac{1}{2\mathcal{I}}\mathbf{L}^2 - \frac{\eta_-}{2\mathcal{I}}\mathbf{L}\cdot\mathbf{J_s} + \frac{\eta_-^2}{8\mathcal{I}}\mathbf{J_s}^2 - \frac{\eta_+}{2\mathcal{I}}\mathbf{L}\cdot\mathbf{J_t} + \frac{\eta_+^2}{8\mathcal{I}}\mathbf{J_t}^2 .
\end{aligned}
\tag{2.41}
$$

where coordinates $\mathbf{s}, \mathbf{t}, u$ correspond to the vibrations F_2^-, F_2^+, A_2^- respectively. As in our analysis of (2.36), it will be useful to introduce a total angular momentum operator $\mathbf{M} = \mathbf{J_s} + \mathbf{J_t} - \mathbf{L}$ combining vibrational angular momentum operators $\mathbf{J_s}, \mathbf{J_t}$ with body-fixed angular momentum $\mathbf{L}$. Energy eigenstates Ψ can be classified by $\mathbf{M}^2 = (\mathbf{J_s} + \mathbf{J_t} - \mathbf{L})^2$, $\mathbf{J_s}^2$, $\mathbf{J_t}^2$, $\mathbf{L}^2$ and vibrational phonon-numbers $N_{F_2^-}, N_{F_2^+}, N_{A_2^-}$, and additionally by their transformation under the O_h symmetry group, where O_h acts on a state by transforming the vibrational coordinates and then performing a compensating rotation of the state:

$$
\Psi \to \rho_{\mathrm{rot}}\left(g\right) \otimes \rho_{\mathrm{vib}}\left(g\right)\Psi .
\tag{2.42}
$$

Explicitly, this action is generated by

$$
C_4 : \Psi \to P_\mathbf{s} P_\mathbf{t} P_u e^{-\frac{2\pi i}{4}\mathbf{n_4}\cdot\mathbf{M}}\Psi
$$

$$
C_3 : \Psi \to e^{-\frac{2\pi i}{3}\mathbf{n_3}\cdot\mathbf{M}}\Psi
\tag{2.43}
$$

$$
-I : \Psi \to P_u P_\mathbf{s}\Psi
$$

where $\mathbf{n_4} = \begin{pmatrix} 0 \\ 0 \\ 1 \end{pmatrix}$, $\mathbf{n_3} = \frac{1}{\sqrt{3}}\begin{pmatrix} -1 \\ -1 \\ -1 \end{pmatrix}$ and where $P_\mathbf{s}, P_\mathbf{t}, P_u$ are parity operators on the vibrational coordinates.

We demand that states transform trivially under the subgroup $\langle C_4, C_3 \rangle \cong O$ consisting of rotations. Within a fixed $\mathbf{M}^2 = (\mathbf{J_s} + \mathbf{J_t} - \mathbf{L})^2$, $\mathbf{J_s}^2$, $\mathbf{J_t}^2$, $\mathbf{L}^2$, $N_{F_2^-}$, $N_{F_2^+}$, $N_{A_2^-}$ sector, we perform character theory calculations and determine A_1 summands as before. Calculating the resulting spectrum, and then fitting the frequencies, Coriolis parameters $\eta_{+/-}$ and moment of inertia Λ of the $B = 4$ to nuclear data, we obtain the best fit (in a least-squares sense) for

the values

$$\hbar\omega_{F_2^-} \approx 9.7\text{MeV} \qquad \frac{\hbar^2}{\mathcal{I}} \approx 4\text{MeV}$$
$$\hbar\omega_{F_2^+} \approx 11.7\text{MeV} \qquad \eta_+ \approx 0.71 \qquad . \qquad (2.44)$$
$$\hbar\omega_{A_2^-} \approx 15.1\text{MeV} \qquad \eta_- \approx 0.13$$

In Table 2.3 and Figure 2.2, we display all allowed states up to 30 MeV for the parameter values in (2.44). The states in this energy range consist of both 1-phonon and 2-phonon excitations. With these 6 parameters we can describe 11 of the 12 experimentally observed Helium-4 states below 30 MeV complete with the correct spin and parity assignments, and we predict one further 0^+ state at 23.4 MeV. A column $E_{\eta=0}$ is included to show the spectrum when Coriolis effects are neglected: the Coriolis corrections have a particularly large effect on the 2^+ states, raising the energy of the lowest 2^+ excitation by as much as 3.3 MeV (comparing favourably to experiment). Note that the ordering of the fitted frequencies does not agree with that of the Skyrme model values in Table 2.1, which put the E^+ as the lowest-energy vibration. This discrepancy can perhaps be understood by considering behaviour beyond small vibrations: recall that the E^+ vibration is associated with the breakup of the $B = 4$ Skyrmion into two $B = 2$ or four $B = 1$ Skyrmions. Physically, the breakup energy for $^4\text{He} \to {}^2\text{H} + {}^2\text{H}$ is 23.8 MeV, higher than the breakup energy for $^4\text{He} \to {}^3\text{H} + \text{p}$ (which should be associated with the F_2 modes) at 20.3 MeV.

Our picture suggests that the 20.2 MeV 0^+ state should be identified with a two-phonon excitation of the F_2^- mode of the cube. Promisingly, electron scattering measurements [19] of the transition form factor for the 0^+ suggest collective behaviour, as noted by the authors of [20]. More recent work based on an ab initio study gives further evidence for the collective interpretation of this state, suggesting a breathing mode [21]. We agree on the collective nature of this state but, based on the $B = 4$ cube, suggest that the breathing mode should be assigned a higher frequency than our F_2^- mode. To compare these two interpretations it would be worthwhile computing transition form factors from our model. This would require the explicit form of the Skyrme fields at each point in our configuration space which, while possible in principle, is beyond the scope of our work. There have also been studies of the negative parity excited states making use of Wigner's theory based on approximate $SU(4)$ symmetry [22]. Our novel picture has the advantage of giving a unified understanding of almost all observed excited states, both positive and negative parity, in terms of simple vibrations of the $B = 4$ cube.

2.5   The $B = 7$ Skyrmion and vibration-isospin coupling

The lowest-energy $B = 7$ Skyrmion is a dodecahedron with symmetry group I_h (illustrated in Figure 2.3) and its normal modes were studied in detail in [23]. If vibrations are not included,

Energy (MeV)

35

30

25

20

2^+

2^+ 1^- 2^-

2^+ 1^+

2^+

1^-

0^+

2^-

0^-

0^+

2^+

1^- 2^- 0^- 2^+

1^+

2^+

1^-

2^-

0^-

0^+

2^+

2^-

2^+

1^-

1^+

1^-

2^+

0^+

2^-

0^-

0^+

Model   Experiment   Model (η=0)
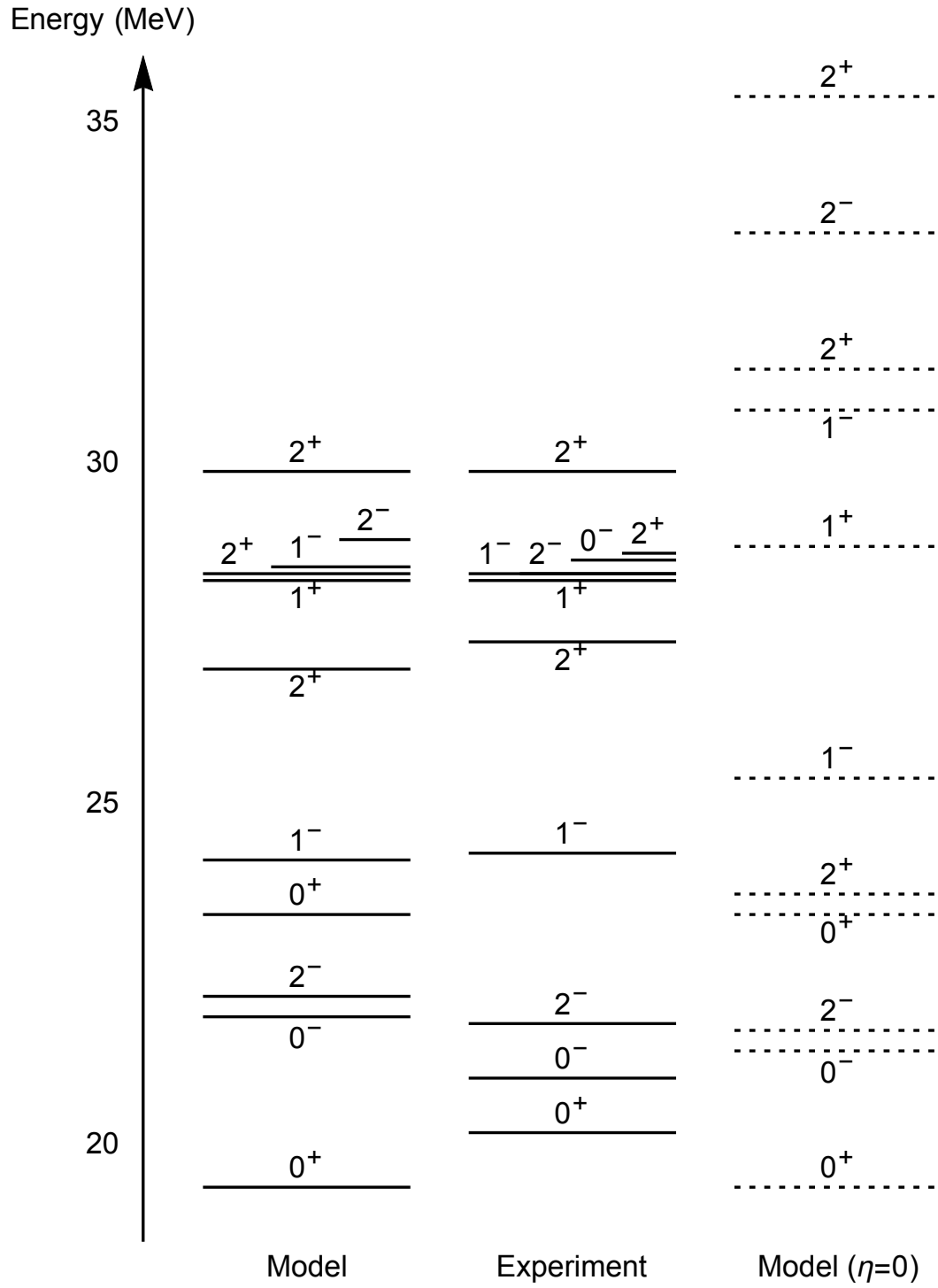
Figure 2.2: Energy level diagram for Helium-4, constructed from the data in Table 2.3. We omit the 0 MeV ground state. The rightmost levels correspond to turning off Coriolis effects.

J^P	$N_{F_2^-}$	$N_{F_2^+}$	$N_{A_2^-}$	$\mathbf{J}_\mathbf{s}^2$	$\mathbf{J}_\mathbf{t}^2$	$\mathbf{L}^2$	$\mathbf{M}^2$	E	$E_{\exp}$	$E_{\eta=0}$
0^+	0	0	0	0	0	0	0	0	0	0
0^+	2	0	0	0	0	0	0	19.4	20.2	19.4
0^-	1	1	0	2	2	0	0	21.9	21.0	21.4
2^-	1	0	0	2	0	6	12	22.2	21.8	21.7
0^+	0	2	0	0	0	0	0	23.4		23.4
1^-	1	1	0	2	2	2	0	24.2	24.3	25.4
2^+	0	1	0	0	2	6	12	27.0	27.4	23.7
1^+	1	0	1	2	0	2	0	28.3	28.3	28.8
1^-	0	1	1	0	2	2	0	28.5	28.4	30.8
2^-	1	1	0	2	2	6	0	28.9	28.4	33.4
0^-									28.6	
2^+	0	2	0	0	6	6	0	28.4	28.7	35.4
2^+	2	0	0	6	0	6	0	29.9	29.9	31.4

Table 2.3: Vibrating $B = 4$ spectrum up to 30 MeV.

the high degree of symmetry of the $B = 7$ means that the lowest energy isospin $\frac{1}{2}$ state has spin $\frac{7}{2}$. In reality, the observed ground state of the Lithium-7/Beryllium-7 isodoublet has spin $\frac{3}{2}$. It was suggested in [24] that to capture this state one should include a five-fold degenerate vibration which transforms in the H_g^5 irrep of I_h and which is generated by pairs of opposite pentagonal faces pulling away from the centre of the Skyrmion. In [25] this vibration was treated within a harmonic approximation and interactions between rotations and vibrations were neglected. Here we extend that analysis to include the Coriolis corrections.

We take our configuration space $\mathcal{C} \simeq SU(2) \times SU(2) \times \mathbb{R}^5$ to include the H_g^5 vibration along with rotations and isorotations. Recalling (2.13), we should now take $\mathbf{A}_i$ to be a 6-component vector for each i as we are including isorotations. Introduce coordinates such that the total metric takes the form (to the order we are interested in)

$$\tilde{g} = \begin{pmatrix} \sigma & ds_i \end{pmatrix} \begin{pmatrix} \Lambda_0 & \Lambda_0 \mathbf{A}_i \\ \mathbf{A}_i^T \Lambda_0 & \delta_{ij} \end{pmatrix} \begin{pmatrix} \sigma \\ ds_j \end{pmatrix} \tag{2.45}$$

with

$$\Lambda_0 = \begin{pmatrix} \Lambda_L \mathbb{I}_3 & 0 \\ 0 & \Lambda_K \mathbb{I}_3 \end{pmatrix}, \tag{2.46}$$

$\mathbf{A}_i$ linear and vanishing at the equilibrium configuration $s_1 = s_2 = s_3 = 0$. Recall Jahn's rule from the end of section 2.3. Now that we are including isorotations, Jahn's rule should be generalised: the gauge field $\mathbf{A}_i$ now corresponds to a singlet of I_h under an action of I_h
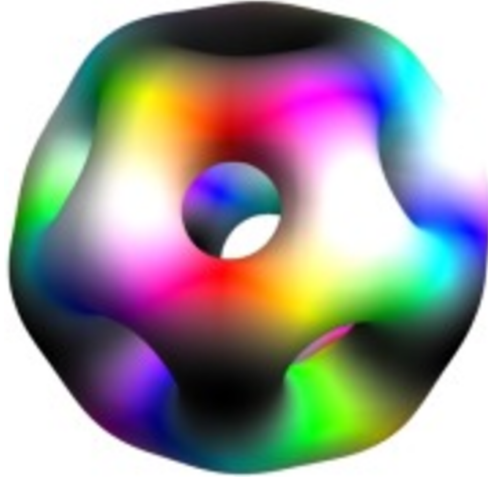
Figure 2.3: B=7 Skyrmion with I_h symmetry. Figure courtesy of Chris Halcrow.

isomorphic to $\rho_{\text{vib}} \otimes \rho_{\text{vib}} \otimes (\rho_{\text{rot}} \oplus \rho_{\text{isorot}})$ where ρ_{isorot} denotes the representation in which isorotations transform under I_h. In the present case, rotations transform as T_{1g}^3 and isorotations transform as T_{2g}^3. An easy calculation shows that

$$H_g^5 \otimes H_g^5 \otimes \left(T_{1g}^3 \oplus T_{2g}^3\right) \cong 2A_g^1 \oplus \cdots \tag{2.47}$$

so there is the possibility of non-trivial Coriolis terms coupling vibrations to spin and isospin (note that we have two copies of the trivial representation and so the coupling will be determined up to two arbitrary constants). We wish to find the symmetry-allowed form of $\mathbf{A}_i$, and for this we need explicit coordinates: note that the usual action of I_h on $\mathbb{R}^3 = \langle e_1, e_2, e_3 \rangle$ is isomorphic to T_{1u}^3 and that the symmetric square $T_{1u}^3 \otimes_S T_{1u}^3 \cong A_g^1 \oplus H_g^5$ contains a copy of the H_g^5 irrep we are interested in. So we pick vibrational coordinates s_1, s_2, s_3, s_4, s_5 (and conjugate momenta p_i) such that the action of I_h is just like the action of I_h on this H_g^5 subspace with basis

$$\begin{gathered} \tfrac{1}{\sqrt{2}} \left(e_2 \otimes e_3 + e_3 \otimes e_2\right), \tfrac{1}{\sqrt{2}} \left(e_1 \otimes e_3 + e_3 \otimes e_1\right), \\ \tfrac{1}{\sqrt{2}} \left(e_1 \otimes e_2 + e_2 \otimes e_1\right), \tfrac{1}{\sqrt{6}} \left(2e_3 \otimes e_3 - e_1 \otimes e_1 - e_2 \otimes e_2\right), \\ \tfrac{1}{\sqrt{2}} \left(e_1 \otimes e_1 - e_2 \otimes e_2\right). \end{gathered} \tag{2.48}$$

In these coordinates we can compute singlets, giving

$$\mathbf{A}_1 = \frac{\eta_L}{2\Lambda_L} \left(-s_5 - \sqrt{3}s_4, -s_3, s_2, 0, 0, 0\right)^T + \frac{\eta_K}{2\Lambda_K} \left(0, 0, 0, -s_5, -s_3, 2s_2\right)^T \tag{2.49}$$

26

$$\mathbf{A}_2 = \frac{\eta_L}{2\Lambda_L} \left(s_3, \sqrt{3}s_4 - s_5, -s_1, 0, 0, 0 \right)^T + \frac{\eta_K}{2\Lambda_K} \left(0, 0, 0, -s_3, s_5, -2s_1 \right)^T \tag{2.50}$$

$$\mathbf{A}_3 = \frac{\eta_L}{2\Lambda_L} \left(-s_2, s_1, 2s_5, 0, 0, 0 \right)^T + \frac{\eta_K}{2\Lambda_K} \left(0, 0, 0, s_2 - \sqrt{3}s_4, s_1, -s_5 \right)^T \tag{2.51}$$

$$\mathbf{A}_4 = \frac{\eta_L}{2\Lambda_L} \left(\sqrt{3}s_1, -\sqrt{3}s_2, 0, 0, 0, 0 \right)^T + \frac{\eta_K}{2\Lambda_K} \left(0, 0, 0, \sqrt{3}s_3, \sqrt{3}s_5, 0 \right)^T \tag{2.52}$$

$$\mathbf{A}_5 = \frac{\eta_L}{2\Lambda_L} \left(s_1, s_2, -2s_3, 0, 0, 0 \right)^T + \frac{\eta_K}{2\Lambda_K} \left(0, 0, 0, s_1, -s_2 - \sqrt{3}s_4, s_3 \right)^T \tag{2.53}$$

where η_L and η_K are constants. This leads to a Hamiltonian

$$\begin{aligned} \mathcal{H} &= \frac{1}{2}\mathbf{p}^2 + \frac{1}{2}\omega^2\mathbf{s}^2 + \frac{1}{2\Lambda_L}\mathbf{L}^2 + \frac{1}{2\Lambda_K}\mathbf{K}^2 \\ &\quad - \left(\frac{\eta_L}{2\Lambda_L}\mathbf{L} \cdot \mathbf{J}_\mathbf{s}^L + \frac{\eta_K}{2\Lambda_K}\mathbf{K} \cdot \mathbf{J}_\mathbf{s}^K \right) + \left(\frac{\eta_L^2}{4\Lambda_L}\mathbf{J}_\mathbf{s}^L \cdot \mathbf{J}_\mathbf{s}^L + \frac{\eta_K^2}{4\Lambda_K}\mathbf{J}_\mathbf{s}^K \cdot \mathbf{J}_\mathbf{s}^K \right). \end{aligned} \tag{2.54}$$

involving the vibrational angular momentum operators

$$\mathbf{J}_\mathbf{s}^L = \begin{pmatrix} -M_{23} + M_{15} + \sqrt{3}M_{14} \\ M_{13} - \sqrt{3}M_{24} + M_{25} \\ -M_{12} - 2M_{35} \end{pmatrix} \tag{2.55}$$

and

$$\mathbf{J}_\mathbf{s}^K = \begin{pmatrix} M_{15} + M_{23} + \sqrt{3}M_{34} \\ M_{13} - M_{25} - \sqrt{3}M_{45} \\ -2M_{12} + M_{35} \end{pmatrix} \tag{2.56}$$

where $M_{ij} = s_i p_j - s_j p_i$. $\mathbf{J}_\mathbf{s}^L$ and $\mathbf{J}_\mathbf{s}^K$ generate rotations in what is now a five-dimensional vibrational space and generalise the vibrational angular momentum $\mathbf{J}_\mathbf{s}$ of (2.35). We are interested in eigenstates of (2.54), which can be classified by $\mathbf{L}^2$, $\mathbf{K}^2$ and vibrational phonon-number. Consider one-phonon states: with respect to a Cartesian basis $\{s_k \exp(-\alpha\mathbf{s}^2)\}$ of vibrational wavefunctions, it is clear how the M_{ij} act:

$$M_{ij}s_k \exp\left(-\alpha\mathbf{s}^2\right) = -i\left(\delta_{il}\delta_{jk} - \delta_{jl}\delta_{ik}\right) s_l \exp\left(-\alpha\mathbf{s}^2\right) \tag{2.57}$$

and thus how $\mathbf{J}_\mathbf{s}^L$ and $\mathbf{J}_\mathbf{s}^K$ act. We diagonalise $\mathcal{H}$ numerically. The relevant group for imposing the F-R constraints is the universal cover of the icosahedral group I, namely the binary icosahedral group $2I \subset SU(2)$, which has presentation

$$\left\langle a, b | (ab)^2 = a^3 = b^5 \right\rangle. \tag{2.58}$$

F-R constraints tell us that physical states must transform trivially under the action of the

generators a and b, given in our coordinates by

$$s : \Psi \to e^{\frac{2\pi i}{3}\mathbf{n}_a^L \cdot \mathbf{L}} \otimes e^{\frac{2\pi i}{3}\mathbf{n}_a^K \cdot \mathbf{K}} \otimes \rho_{\text{vib}}(a)\, \Psi \tag{2.59}$$

$$t : \Psi \to e^{\frac{2\pi i}{5}\mathbf{n}_b^L \cdot \mathbf{L}} \otimes e^{\frac{6\pi i}{5}\mathbf{n}_b^K \cdot \mathbf{K}} \otimes \rho_{\text{vib}}(b)\, \Psi$$

where

$$\mathbf{n}_a^L = \begin{pmatrix} \sqrt{\frac{2}{15}\left(5-\sqrt{5}\right)} \\ 0 \\ \sqrt{\frac{1}{15}\left(5+2\sqrt{5}\right)} \end{pmatrix}, \mathbf{n}_a^K = \begin{pmatrix} -\sqrt{\frac{2}{15}\left(5+\sqrt{5}\right)} \\ 0 \\ -\sqrt{\frac{1}{15}\left(5-2\sqrt{5}\right)} \end{pmatrix}, \mathbf{n}_b^L = \begin{pmatrix} 0 \\ 0 \\ 1 \end{pmatrix}, \mathbf{n}_b^K = \begin{pmatrix} 0 \\ 0 \\ 1 \end{pmatrix}. \tag{2.60}$$

The first few allowed states are listed in Table 2.4 along with the expectation values of the Coriolis terms. These Coriolis terms represent our corrections to the spectrum found in [25] which assumed complete separation of rotations and vibrations. That work focused on the isospin $\frac{1}{2}$ sector: within this sector one obtains a zero-phonon state with spin $\frac{7}{2}$ (identified with a 4.6 MeV excitation of Lithium-7) and one-phonon states with spins $\frac{3}{2}$, $\frac{5}{2}$, and $\frac{7}{2}$ (identified with 0, 6.7 and 9.7 MeV excitations of Lithium-7). Ignoring Coriolis terms, the one-phonon states form a rotational band with energies following a simple $J(J+1)$ pattern. The experimental data doesn't fit this pattern particularly well: the rotational band energy ratio

$$\frac{E\left(J=\frac{7}{2}\right)-E\left(J=\frac{3}{2}\right)}{E\left(J=\frac{5}{2}\right)-E\left(J=\frac{3}{2}\right)} = \frac{7\times 9 - 3\times 5}{5\times 7 - 3\times 5} = 2.4 \tag{2.61}$$

which is to be compared with the experimental result $\frac{9.7}{6.7} \approx 1.4$. We now consider the effect of including Coriolis terms for these isospin $\frac{1}{2}$ states. Recall that, for the $B=7$ Skyrmion, $\frac{\Lambda_K}{\Lambda_L} \sim 0.1$ as found in [13]. So it is reasonable to assume that, for the one-phonon states, the most important effect of the Coriolis terms is the energy splitting of size $\frac{\eta_K}{\Lambda_K}$ which (for $\eta_K > 0$) lowers the energy of the spin $\frac{3}{2}$ state while raising the energies of the spin $\frac{5}{2}$ and $\frac{7}{2}$ states. We now get

$$\frac{E\left(J=\frac{7}{2}\right)-E\left(J=\frac{3}{2}\right)}{E\left(J=\frac{5}{2}\right)-E\left(J=\frac{3}{2}\right)} = \frac{7\times 9 - 3\times 5 + \frac{8\eta_K \Lambda_L}{\Lambda_K}}{5\times 7 - 3\times 5 + \frac{8\eta_K \Lambda_L}{\Lambda_K}} \tag{2.62}$$

which reproduces the experimental ratio of 1.4 for a Coriolis parameter of $\eta_K \approx \frac{25}{4}\frac{\Lambda_K}{\Lambda_L} \sim 0.5$. It would be interesting to calculate η_K explicitly from the Skyrme model and compare to this value.

We have learnt from this example that, in situations where the isospin moment of inertia is much smaller than the spin moment of inertia, the isospin Coriolis corrections can compete with the usual $\frac{1}{2\Lambda_L}J(J+1)$ rotational band splittings. This kind of effect is particularly important for odd B Skyrmions like the $B=7$, where non-zero isospin is inevitable (isospin

Spin/Isospin	Energy without Coriolis terms	Coriolis terms
$\left(\frac{7}{2}/\frac{1}{2}\right)_{0-\text{phonon}}$	$\frac{5}{2}\omega + \frac{1}{2\Lambda_L}\frac{7}{2}\frac{9}{2} + \frac{1}{2\Lambda_K}\frac{1}{2}\frac{3}{2}$	0
$\left(\frac{3}{2}/\frac{1}{2}\right)_{1-\text{phonon}}$	$\frac{7}{2}\omega + \frac{1}{2\Lambda_L}\frac{3}{2}\frac{5}{2} + \frac{1}{2\Lambda_K}\frac{1}{2}\frac{3}{2}$	$3\frac{\eta_L}{2\Lambda_L} - \frac{3}{2}\frac{\eta_K}{2\Lambda_K} + 6\frac{\eta_L^2}{4\Lambda_L} + 6\frac{\eta_K^2}{4\Lambda_K}$
$\left(\frac{5}{2}/\frac{1}{2}\right)_{1-\text{phonon}}$	$\frac{7}{2}\omega + \frac{1}{2\Lambda_L}\frac{5}{2}\frac{7}{2} + \frac{1}{2\Lambda_K}\frac{1}{2}\frac{3}{2}$	$\frac{1}{2}\frac{\eta_L}{2\Lambda_L} + \frac{\eta_K}{2\Lambda_K} + 6\frac{\eta_L^2}{4\Lambda_L} + 6\frac{\eta_K^2}{4\Lambda_K}$
$\left(\frac{7}{2}/\frac{1}{2}\right)_{1-\text{phonon}}$	$\frac{7}{2}\omega + \frac{1}{2\Lambda_L}\frac{7}{2}\frac{9}{2} + \frac{1}{2\Lambda_K}\frac{1}{2}\frac{3}{2}$	$-3\frac{\eta_L}{2\Lambda_L} + \frac{\eta_K}{2\Lambda_K} + 6\frac{\eta_L^2}{4\Lambda_L} + 6\frac{\eta_K^2}{4\Lambda_K}$
$\left(\frac{3}{2}/\frac{3}{2}\right)_{0-\text{phonon}}$	$\frac{5}{2}\omega + \frac{1}{2\Lambda_L}\frac{3}{2}\frac{5}{2} + \frac{1}{2\Lambda_K}\frac{3}{2}\frac{5}{2}$	0
$\left(\frac{1}{2}/\frac{3}{2}\right)_{1-\text{phonon}}$	$\frac{7}{2}\omega + \frac{1}{2\Lambda_L}\frac{1}{2}\frac{3}{2} + \frac{1}{2\Lambda_K}\frac{3}{2}\frac{5}{2}$	$-\frac{3}{2}\frac{\eta_L}{2\Lambda_L} + 3\frac{\eta_K}{2\Lambda_K} + 6\frac{\eta_L^2}{4\Lambda_L} + 6\frac{\eta_K^2}{4\Lambda_K}$
$\left(\frac{3}{2}/\frac{3}{2}\right)_{1-\text{phonon}}$	$\frac{7}{2}\omega + \frac{1}{2\Lambda_L}\frac{3}{2}\frac{5}{2} + \frac{1}{2\Lambda_K}\frac{3}{2}\frac{5}{2}$	$-3\frac{\eta_L}{2\Lambda_L} - 3\frac{\eta_K}{2\Lambda_K} + 6\frac{\eta_L^2}{4\Lambda_L} + 6\frac{\eta_K^2}{4\Lambda_K}$

Table 2.4: $B = 7$ Skyrmion energy spectrum including one-phonon H_g^5 excitations.

taking half-integer values). This fits with the fact that the rotational band picture has been much more successful for even B nuclei than for odd B nuclei.

2.6 Conclusions and further work

We have developed a model of Helium-4 based on F_2 and A_2 vibrations of the cubic $B = 4$ Skyrmion. Our model includes interactions between rotations and vibrations in the form of Coriolis terms. The spectrum gives a good match to the experimental data, with the Coriolis terms significantly improving the fit. The lowest state not captured by the model is a 0^- state at 28.6 MeV, and we predict one so far unobserved 0^+ state at 23.4 MeV. We have also extended these ideas to the $B = 7$ Skyrmion, clarifying the role of isospin-vibration coupling.

The example in section 2.5 suggests a general feature which should occur in vibrational quantization of Skyrmions with non-zero isospin. It has been noted (e.g. in [26]) that for large B the isospin moments of inertia for Skyrmions are much smaller than the spin moments of inertia, with $\Lambda_K \sim B$ and $\Lambda_L \sim B^{\frac{5}{3}}$. So, for large B, isospin Coriolis corrections can become more important than the usual $\frac{1}{2\Lambda_L}J(J+1)$ rotational band splittings. The stable large nuclei all have large isospin and so these ideas are important for the Skyrme model description of many real nuclei.

It would be interesting to calculate the actual values for the Coriolis coefficients η numerically within the Skyrme model. This requires explicit field configurations for vibrating Skyrmions but such configurations have been calculated before in e.g. [11]. It would also be interesting to study the effect of the gauge field $\mathbf{A}_i$ for a situation in which shape space includes large deformations (not just small vibrations).

Finally, it should be noted that, while our ideas have been outlined within the context of the Skyrme model, this work is very general and these ideas could be applied to other soliton systems in which one is interested in the interplay between zero and non-zero modes.

Chapter 3

An α-particle model for Carbon-12

This chapter is based on the single-author paper [27].

3.1 Motivation

Theoretical studies of the Carbon-12 nucleus have a long and interesting history. Most famously, in the 1950s Fred Hoyle predicted that Carbon-12 should have a positive-parity resonance just above the threshold for breakup into Beryllium-8 and Helium-4 [28]. He argued that such a state would lead to resonant enhancement of Carbon-12 production during stellar nuclear synthesis, explaining the abundance of Carbon-12 in our universe. His prediction was confirmed experimentally with the discovery of the 7.7 MeV 0^+ excitation [29, 30], now known as the Hoyle state.

It is widely agreed that Carbon-12 can be usefully thought of in terms of α-clusters. There is a band in the observed energy spectrum containing states with the characteristic spin and parity combinations 0^+, 2^+, 3^-, $4^\pm$,... , often referred to as the ground state band. These are exactly the states which arise from a rotating equilateral triangle of α-particles, and are physically interpreted as such. There has been less agreement on the physical interpretation of the Hoyle state (and the other observed low-lying excited states outside of the ground state band) with many interpretations offered including a rigid linear chain [31], a bent arm [32], a breathing vibration [33] of an equilateral triangle and even a diffuse gas of α-particles [34].

The Skyrme model, which we introduced in Chapter 2, has two well-known Skyrmion solutions with Baryon number $B = 12$. They have symmetry groups D_{3h} and D_{4h} and can be viewed as three $B = 4$ Skyrmions (analogous to α-particles) arranged in an equilateral triangle and a linear chain respectively (Figure 3.1). When quantized individually as rigid bodies, each contributes a rotational band to the energy spectrum. The allowed spin and parity combinations of the quantum states appearing in each band are determined by the

corresponding symmetry group (D_{3h} or D_{4h}).
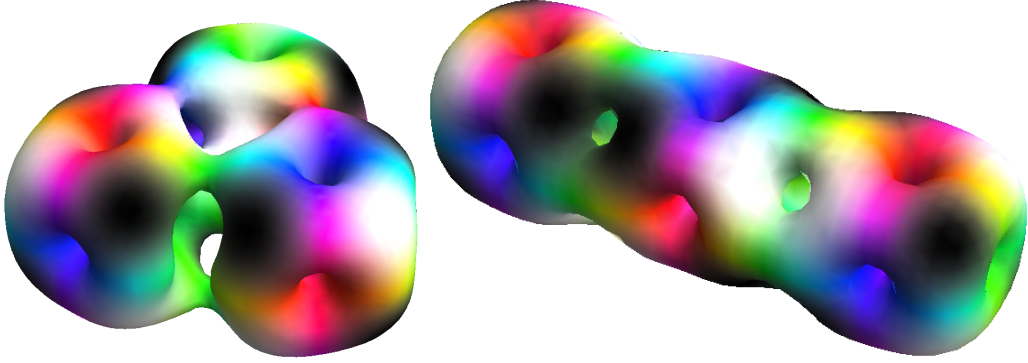
Figure 3.1: $B = 12$ Skyrmions with D_{3h} symmetry (left) and D_{4h} symmetry (right). Figures courtesy of Dankrad Feist.

The energy levels found by this approach [31] match some of the experimentally observed Carbon-12 states [14]. The D_{3h}-symmetric Skyrmion gives rise to a rotational band with spin and parity combinations 0^+, 2^+, 3^-, 4^-, 4^+ (and higher spins). This is a feature of any model based on an equilateral triangle of α-particles. A particular success of the Skyrme model prediction is the characteristic pattern 0^+, 2^+, 4^+ of the Hoyle band [35], which arises from rotational excitations of the D_{4h}-symmetric linear chain. An alternative possibility is to identify the Hoyle band with rotational excitations of a breathing (symmetrically vibrating) equilateral triangle, as has been done within the context of the algebraic cluster model (ACM) [36]. However, this would imply the existence of additional 3^- and 4^- states within the rotational band which have not been observed. It is the D_{4h} symmetry group of the Skyrmion which excludes such states. This suggests that a linear chain configuration of alpha particles could play an important role in the structure of the low-lying states of Carbon-12, as well as the more familiar equilateral triangular configuration.

However, the rigid body picture is overly restrictive: several low-lying states (seen in addition to the rigid body rotational bands) are completely missing as all of the configurations considered have a lot of symmetry. Large symmetry groups lead to severe restrictions on the possible spin and parity combinations. It is clear that we need to go beyond rigid body quantization: we need to allow the nucleus to deform. Such an approach has been successful in studying the excited states of other nuclei such as Oxygen-16 [7].

We propose a simplified model for the Carbon-12 nucleus, viewed as three point particles. Building on the ideas outlined above, we allow both the equilateral triangle and the linear chain. The difference is that they sit within a larger configuration space which includes shapes that interpolate between these two highly symmetric configurations. This extra degree of freedom allows more spin and parity combinations than rigid body quantization.

A key assumption is that the potential energy landscape is quite flat in the shape-

deforming direction where the equilateral triangle becomes a linear chain. If it is not so flat, then for sufficiently low energies an analysis of small vibrations about the equilateral triangle (or about the linear chain) should be appropriate. This approximation leads to far more low-lying states than have been experimentally observed. We propose that this approximation is inappropriate: at the energies we are interested in, the triangle can deform significantly and a global approach is required.

3.2   The configuration space, $\mathcal{C}$

We start with the configuration space for three point particles,

$$\{(\mathbf{x_1}, \mathbf{x_2}, \mathbf{x_3}) \in \mathbb{R}^9\}$$

equipped with the Euclidean metric. We can separate the centre of mass motion, as usual, restricting to $\sum_{i=1}^{3} \mathbf{x_i} = 0$. We further restrict to configurations where the area of the triangle formed by the three particles has a particular shape-dependent value. Physically, this is reasonable if we assume that the energy associated with the triangle expanding compared to some equilibrium size is large compared to the energies we are interested in. The equilibrium size will be taken to vary in such a way that the ratio of the moments of inertia for the equilateral triangle and the linear chain (which determines the ratio of slopes of the corresponding rotational bands) reproduces the result from the Skyrme model.
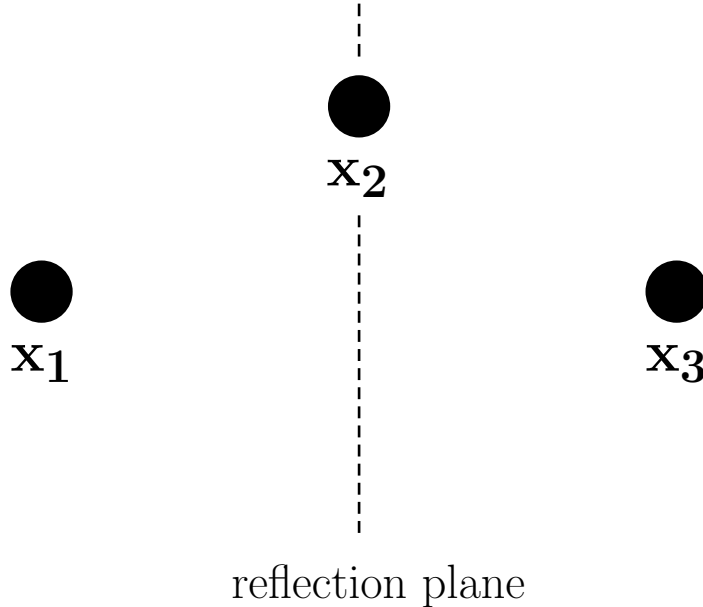
Figure 3.2: $\mathcal{C}_i$ consists of isosceles configurations with particle number i lying in the plane of reflection symmetry. Thus $\mathcal{C}_2$ contains the above configuration.
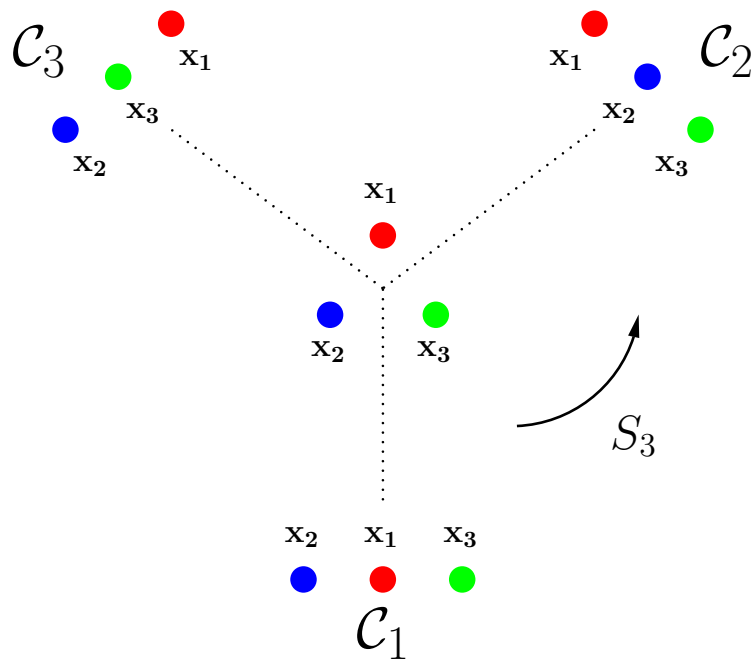
Figure 3.3: Graph structure of $\mathcal{C} = \cup_i \mathcal{C}_i$.

Finally, we make one further restriction: we will consider only a certain subset of configurations, in which the three particles lie at the vertices of an isosceles triangle. The shapes we restrict to are precisely those isosceles triangles which interpolate between an equilateral triangle and a linear chain. Thus we only include the direction in which the equilateral triangle becomes an obtuse triangle, assuming that changing shape in the other direction corresponds to a sharp increase in potential energy due to trying to bring two α-particles very close together. The resulting configuration space, denoted $\mathcal{C}$, is best pictured as the union of three 4-manifolds, $\mathcal{C} = \cup_i \mathcal{C}_i$. Here $\mathcal{C}_i$ corresponds to those isosceles configurations with particle number i lying in the plane of reflection symmetry. This is illustrated in Figures 3.2 and 3.3. The $\mathcal{C}_i$ intersect at a 3-manifold corresponding to the equilateral triangles (this intersection can be thought of as a copy of the group manifold $SO(3)$, since this group acts on the set of equilateral triangular configurations).

The particles should be indistinguishable: this will be imposed at the quantum level by demanding that states are taken to lie in the trivial representation of the group S_3 which acts on $\mathcal{C}$ by permuting the three particles.

The structure of $\mathcal{C}$ is reminiscent of configuration spaces appearing in QGT. We will use ideas from that area to motivate our definition of quantum mechanics on $\mathcal{C}$, thinking of the $\mathcal{C}_i$ as edges which intersect at a vertex [37]. Approximating a quantum system as a graph is an idea that dates back to Pauling [38], who studied the dynamics of free electrons in hydrocarbons by considering motion in a network with edges corresponding to carbon-carbon bonds and vertices corresponding to carbon atoms.

3.3 The metric on $\mathcal{C}_1$

We begin by focusing on $\mathcal{C}_1$. This is the only part of $\mathcal{C}$ that we need to think about since all points in $\mathcal{C}$ are generated by the action of S_3 on $\mathcal{C}_1$. The group of rotations in physical space acts on $\mathcal{C}_1$ as a symmetry, so we pick coordinates (s, θ, ϕ, ψ) consisting of a shape parameter s together with Euler angles θ, ϕ, ψ specifying the orientation of the shape. Corresponding to $\theta = \phi = \psi = 0$, we need to pick a set of reference orientations for each $SO(3)$ orbit. These reference configurations give a submanifold $\mathcal{C}_{\text{shapes}}$. We define $\mathcal{C}_{\text{shapes}}$ as follows: let the choice $(s, 0, 0, 0)$ correspond to the configuration

$$\mathbf{x_1} = (0, s, 0), \; \mathbf{x_2} = \left(-\frac{1}{2}\sqrt{2 - 3s^2}, -\frac{1}{2}s, 0\right), \; \mathbf{x_3} = \left(\frac{1}{2}\sqrt{2 - 3s^2}, -\frac{1}{2}s, 0\right). \qquad (3.1)$$

i.e. we rotate the triangle so that particle 1 lies on the positive y-axis with the plane of reflection symmetry being the $y - z$-plane. The range we consider is $s \in [0, s_{\text{max}}]$ where $s_{\text{max}} = \frac{1}{\sqrt{3}}$. Note that $s = 0$ gives a linear chain and as we increase s we approach an equilateral triangle at $s = s_{\text{max}}$. This particular choice of reference orientations has the nice property that the metric on $\mathcal{C}_1$, in these coordinates, takes the simple block-diagonal form

$$G_{\mathcal{C}_1} = \begin{pmatrix} g_{\text{rot}} & 0 \\ 0 & g \end{pmatrix}. \qquad (3.2)$$

In the principal bundle language of the previous chapter, we have picked a gauge in which the connection $\mathbf{A}$ (which is related to the cross-terms between rotations and vibrations) vanishes. This simplification can be seen as follows: as we move through the reference configurations, there is enough symmetry (reflection in the xy-plane and in the yz-plane) that no angular momentum is generated by the corresponding motion of the particles. Therefore the motion in shape space decouples from the rotational motion (no cross-terms in the metric) and its only effect is through the shape-dependent moments of inertia which appear in g_{rot}. The function g corresponds to the pull-back of the Euclidean metric on $\mathbb{R}^9$ arising from the inclusion $\mathcal{C}_{\text{shapes}} \hookrightarrow \mathbb{R}^9$.

3.4 Quantum Mechanics on $\mathcal{C}$

3.4.1 Computing the quantum Hamiltonian

Recall that in Chapter 2, we showed that a general metric of the form

$$\tilde{g} = \begin{pmatrix} \sigma & ds_i \end{pmatrix} \begin{pmatrix} \Lambda & \Lambda \mathbf{A}_j \\ \mathbf{A}_i^T \Lambda & g_{ij} + \mathbf{A}_i \cdot \Lambda \cdot \mathbf{A}_j \end{pmatrix} \begin{pmatrix} \sigma \\ ds_j \end{pmatrix} \qquad (3.3)$$

leads, via computation of the Laplace-Beltrami operator, to a quantum Hamiltonian

$$\mathcal{H} = \frac{1}{2}\mathbf{L} \cdot \Lambda^{-1} \cdot \mathbf{L} + \frac{1}{2}(p_i - \mathbf{L} \cdot \mathbf{A}_i)\, g_{ij}^{-1}(p_j - \mathbf{L} \cdot \mathbf{A}_j) + V_2(s) + V(s) \tag{3.4}$$

where

$$V_2(s) = \frac{\hbar^2}{2}(|\Lambda|\,|g_{ij}|)^{-\frac{1}{4}}\, \partial_i\left(g_{ij}^{-1}\partial_j\,(|\Lambda|\,|g_{ij}|)^{\frac{1}{4}}\right). \tag{3.5}$$

In the present context, we have only one shape degree of freedom $s = s_i$ along the graph edge and we have also argued in Section 3.3 that the connection $\mathbf{A}$ vanishes due to our gauge choice. So we see that the metric (3.2) leads to a quantum Hamiltonian

$$\mathcal{H} = \frac{1}{2}\mathbf{L} \cdot \Lambda^{-1} \cdot \mathbf{L} + \frac{1}{2}pg^{-1}p + V_2(s) + V(s) \tag{3.6}$$

where we have also included a potential $V(s)$ on configuration space and where

$$V_2(s) = \frac{\hbar^2}{2}(|\Lambda|\,|g|)^{-\frac{1}{4}}\, \partial_s\left(g^{-1}\partial_s\,(|\Lambda|\,|g|)^{\frac{1}{4}}\right). \tag{3.7}$$

Using the explicit particle positions given in 3.1, we can compute the functions appearing in (3.6) such as the moment of inertia tensor

$$\Lambda_{ij}(s) = \sum_{k=1}^{3}(\mathbf{x}_k^2\delta_{ij} - (\mathbf{x}_k)_i\,(\mathbf{x}_k)_j) = \begin{pmatrix} \frac{3}{2}s^2 & 0 & 0 \\ 0 & 1 - \frac{3}{2}s^2 & 0 \\ 0 & 0 & 1 \end{pmatrix} \tag{3.8}$$

and the pull-back of the Euclidean metric to shape space

$$g(s) = \sum_{i=1}^{3}\left(\frac{d\mathbf{x}_k}{ds}\right)^2 = \frac{3}{2} + \frac{9s^2}{2(2 - 3s^2)}. \tag{3.9}$$

Exploiting rotational symmetry, we can classify the energy eigenstates of (3.6) by J (where $J(J+1)$ is the eigenvalue of $\mathbf{J}^2$ in the usual way) and J_3. Recall from rigid-body theory that a complete set of commuting operators for the rotational part of the problem is given by $\mathbf{J}^2, J_3, L_3$ and so within a particular (J, J_3) sector we can expand the total wavefunction

$$\Psi = \sum_{L_3=-J}^{+J} \chi_{L_3}(s)\,|JJ_3L_3\rangle. \tag{3.10}$$

Substituting the expansion for Ψ above into the Hamiltonian, we obtain the Schrödinger

35

equation

$$\frac{1}{2}\mathbf{L} \cdot \Lambda^{-1} \cdot \mathbf{L} \begin{pmatrix} \chi_{-J}(s) \\ \vdots \\ \chi_J(s) \end{pmatrix} + \frac{1}{2}pg^{-1}p \begin{pmatrix} \chi_{-J}(s) \\ \vdots \\ \chi_J(s) \end{pmatrix} \tag{3.11}$$

$$+ (V_2(s) + V(s) - E) \begin{pmatrix} \chi_{-J}(s) \\ \vdots \\ \chi_J(s) \end{pmatrix} = 0$$

where now the operators $\mathbf{L}$ act by matrix multiplication.

3.4.2 Discrete symmetries

There are additional discrete symmetries present: the system is symmetric under permutations of the three particles and the action of parity. Note that parity is realised by a rotation through π about the body-fixed 3-axis since the configurations are planar. The parity transformation commutes with the permutations and so together these transformations generate a symmetry group isomorphic to $S_3 \times C_2$ which acts on each (J, J_3) sector. Thus we can further classify states into irreducible representations of the discrete group $S_3 \times C_2$. These are precisely the tensor products $\rho_{S_3} \otimes \rho_{C_2}$ of irreducible representations ρ_{S_3} and ρ_{C_2} of S_3 and C_2 respectively. We want the particles to be indistinguishable, so we choose those representations for which the first factor is the trivial representation: $\rho_{S_3} = 1$. If we let ρ_{trivial} and ρ_{sign} denote the (familiar) irreducible representations of C_2, then this means that states can be taken to lie in representations isomorphic to $1 \otimes \rho_{\text{trivial}}$ or $1 \otimes \rho_{\text{sign}}$. Those transforming in the representation $1 \otimes \rho_{\text{trivial}}$ will be referred to as positive parity states, J^+, and those transforming in $1 \otimes \rho_{\text{sign}}$ as negative parity states J^-.

Note that equation (3.11) is a system of coupled equations for the effective one-dimensional problem on shape space. The simplest case to consider is $J = 0$. Note that in this subspace only positive parity states 0^+ exist. $\mathbf{L}$ acts on these states as the zero operator which leaves us with a single ordinary differential equation in s:

$$\left(\frac{1}{2}pg^{-1}p\right)\chi_0 = (E - V - V_2)\chi_0. \tag{3.12}$$

Solving this equation for χ_0 gives the total wavefunction

$$\Psi(s, \theta, \psi, \psi) = \chi_0(s) \ket{0, 0}. \tag{3.13}$$

(From here on we suppress the space-fixed angular momentum label J_3). For higher J the term of the form $(\mathbf{L} \cdot \Lambda^{-1} \cdot \mathbf{L})\Psi$ appearing in the Schrödinger equation will mix states with

different L_3 values, leading to systems of coupled ordinary differential equations. Let us consider $J = 2$ as an example. We begin by writing down the most general element in the $J = 2$ sector:

$$\Psi = \chi_{-2} \left|2, -2\right\rangle + \chi_{-1} \left|2, -1\right\rangle + \chi_0 \left|2, 0\right\rangle + \chi_1 \left|2, 1\right\rangle + \chi_2 \left|2, 2\right\rangle. \tag{3.14}$$

Suppose we are interested in positive parity states 2^+. Such states transform in the representation $1 \otimes \rho_{\text{trivial}}$ of $S_3 \times C_2$. In particular, they should transform trivially under the action of both $\exp(i\pi L_2)$ (swapping particles 2 and 3) and $\exp(i\pi L_3)$ (parity). So they lie in a two-dimensional subspace spanned by the set $\{\left|2, 0\right\rangle, \left|2, -2\right\rangle + \left|2, 2\right\rangle\}$. In other words, the 2^+ states have the restricted form

$$\Psi = \chi_0 \left|2, 0\right\rangle + \chi_2 (\left|2, -2\right\rangle + \left|2, 2\right\rangle). \tag{3.15}$$

It can be checked that the combination $\mathbf{L} \cdot \Lambda^{-1} \cdot \mathbf{L}$ appearing in (3.11) then takes the explicit form

$$(\mathbf{L} \cdot \Lambda^{-1} \cdot \mathbf{L})\Psi = \begin{pmatrix} 3(\Lambda_{11}^{-1} + \Lambda_{22}^{-1}) & \sqrt{6}(\Lambda_{11}^{-1} - \Lambda_{22}^{-1}) \\ \frac{\sqrt{6}}{2}(\Lambda_{11}^{-1} - \Lambda_{22}^{-1}) & \Lambda_{11}^{-1} + \Lambda_{22}^{-1} + 4\Lambda_{33}^{-1} \end{pmatrix} \begin{pmatrix} \chi_0 \\ \chi_2 \end{pmatrix}. \tag{3.16}$$

The off-diagonal terms in the matrix are non-zero so we have a coupled system for the two functions χ_0 and χ_2.

More generally, for spin J states the operator $\exp(i\pi L_2)$ has the following diagonal matrix form with respect to the basis $\{\left|J, -J\right\rangle, \ldots, \left|J, J\right\rangle\}$:

$$\exp(i\pi L_2) = (-1)^J \begin{pmatrix} & & & & & & & (-1)^J \\ & & & & & & \cdot^{\cdot^{\cdot}} & \\ & & & & & 1 & & \\ & & & & -1 & & & \\ & & & 1 & & & & \\ & & -1 & & & & & \\ & 1 & & & & & & \\ \cdot^{\cdot^{\cdot}} & & & & & & & \\ (-1)^J & & & & & & & \end{pmatrix}. \tag{3.17}$$

This observation makes it very easy to compute a basis for allowed states of a given spin and parity, summarised in Table 3.1.

3.4.3 Boundary conditions

We can solve these equations numerically, once we have specified suitable boundary conditions on the wavefunction. The boundary conditions we impose at the intersection of the C_i are

J^P	basis	J^P	basis
0^+	$\lvert 0,0\rangle$	0^-	
1^+		1^-	$\lvert 1,-1\rangle + \lvert 1,1\rangle$
2^+	$\lvert 2,-2\rangle + \lvert 2,2\rangle$ $\lvert 2,0\rangle$	2^-	$\lvert 2,-1\rangle - \lvert 2,1\rangle$
3^+	$\lvert 3,-2\rangle - \lvert 3,2\rangle$	3^-	$\lvert 3,-3\rangle + \lvert 3,3\rangle$ $\lvert 3,-1\rangle + \lvert 3,1\rangle$
4^+	$\lvert 4,-4\rangle + \lvert 4,4\rangle$ $\lvert 4,-2\rangle + \lvert 4,2\rangle$ $\lvert 4,0\rangle$	4^-	$\lvert 4,-3\rangle - \lvert 4,3\rangle$ $\lvert 4,-1\rangle - \lvert 4,1\rangle$
5^+	$\lvert 5,-4\rangle - \lvert 5,4\rangle$ $\lvert 5,-2\rangle - \lvert 5,2\rangle$	5^-	$\lvert 5,-5\rangle + \lvert 5,5\rangle$ $\lvert 5,-3\rangle + \lvert 5,3\rangle$ $\lvert 5,-1\rangle + \lvert 5,1\rangle$

Table 3.1: Bases for allowed states.

as described in Chapter 1: following the quantum graph literature, we demand that the wavefunction is continuous at the equilateral triangle ($s = s_{max} = \frac{1}{\sqrt{3}} \approx 0.58$) with outgoing derivatives along the three edges (the $\mathcal{C}_i$) summing to zero. The latter condition ensures the conservation of the probability current [39]. By the outgoing derivative along an edge we mean the derivative in the direction orthogonal to the fibre generated by the action of the rotation group: in the case of $\mathcal{C}_1$, for which we have constructed explicit coordinates, this just means the partial derivative with respect to the coordinate s (the block-diagonal form of the metric $G_{\mathcal{C}_1}$ makes it clear that this direction is orthogonal to the action of rotations).

In our problem, we have the additional requirement of indistinguishability: S_3 must act trivially on physical states. This means that the wavefunction on $\mathcal{C}_2$ and $\mathcal{C}_3$ is determined by the wavefunction on $\mathcal{C}_1$, and so these boundary conditions are in every case equivalent to some boundary condition on the χ_{L_3} (which are functions defined only on the smaller set $\mathcal{C}_1$). To make this clearer, consider Figure 3.4.

Suppose we have constructed local coordinates (t, θ, ϕ, ψ) on $\mathcal{C}_3$ just as on $\mathcal{C}_1$ and that the illustrated configurations correspond to the cross-section of $\mathcal{C}$ given by $\theta = \phi = \psi = 0$. It is clear from the diagram that indistinguishability implies that the wavefunction on $\mathcal{C}_3$ should be related to the wavefunction on $\mathcal{C}_1$ by

$$\Psi^{\mathcal{C}_3} = \exp\left(i\frac{2\pi}{3}L_3\right)\Psi^{\mathcal{C}_1}, \tag{3.18}$$

i.e. if we rotate the configurations shown in $\mathcal{C}_1$ by $\frac{2\pi}{3}$ then they agree with the configurations shown in $\mathcal{C}_3$ up to relabelling of particle number and so are physically indistinguishable. Going back to our 2^+ example, we had that

$$\Psi^{\mathcal{C}_1} = \chi_0\lvert 2,0\rangle + \chi_2(\lvert 2,-2\rangle + \lvert 2,2\rangle). \tag{3.19}$$
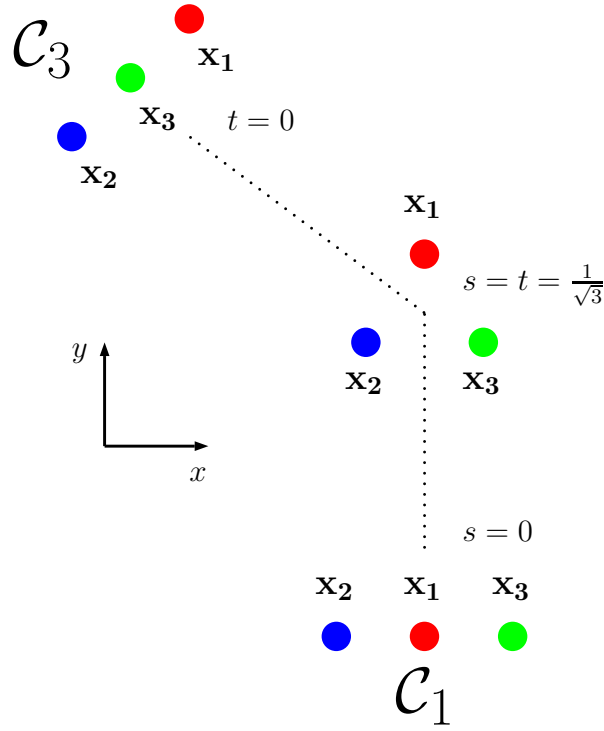
Figure 3.4: Cross-section of part of $\mathcal{C}$ with $\theta = \phi = \psi = 0$.

So

$$\exp\left(i\frac{2\pi}{3}L_3\right)\Psi^{\mathcal{C}_1} = \chi_0 \left|2,0\right\rangle + \chi_2(\exp\left(-i\frac{4\pi}{3}\right)\left|2,-2\right\rangle + \exp\left(i\frac{4\pi}{3}\right)\left|2,2\right\rangle). \qquad (3.20)$$

Continuity of the wavefunction then implies χ_2 vanishes at the equilateral triangle while the derivative condition implies the derivative of χ_0 vanishes at the equilateral triangle. An example of such a solution can be seen later in Figure 3.7.

3.5   Wavefunctions and energy levels

We want a potential $V(s)$ which has local minima at the linear chain and the equilateral triangle. A simple choice is a quartic polynomial (Figure 3.5). This involves picking five coefficients, but the two conditions just mentioned together with the freedom to specify a zero-point energy means that such a potential has only two free parameters. These can be thought of as the energy difference between the two minima and the height of the potential barrier between them.

We fix our energy units by matching the energy difference between the lowest-lying 0^+ and 2^+ states of Carbon-12 to experiment, and adjust the values of the two parameters in the potential to give a spectrum which is closest to the experimentally observed energies.
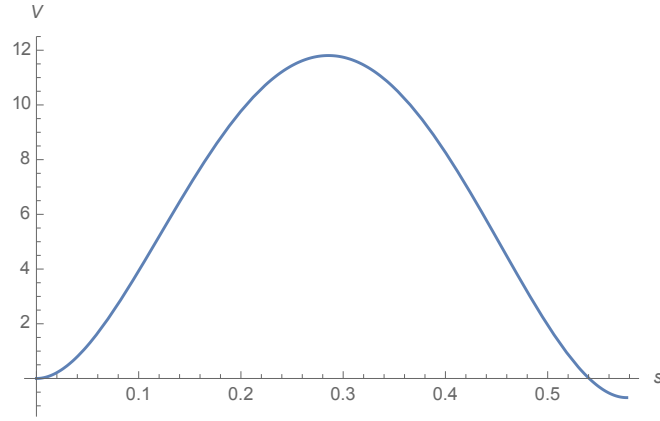
Figure 3.5: Potential $V(s)$. This particular V corresponds to our final choice of parameters, and is expressed in MeV.

The potential illustrated in Figure 3.5 corresponds to our choice of parameters.

3.5.1 Asymptotic rigid body regime

Before presenting our results, we pause to explore the limit of our model where we take the barrier height between the equilateral and the linear chain to be much larger than in Figure 3.5. In this limit, we recover the usual rigid body picture [27], whose spectrum is shown in Figure 3.6.
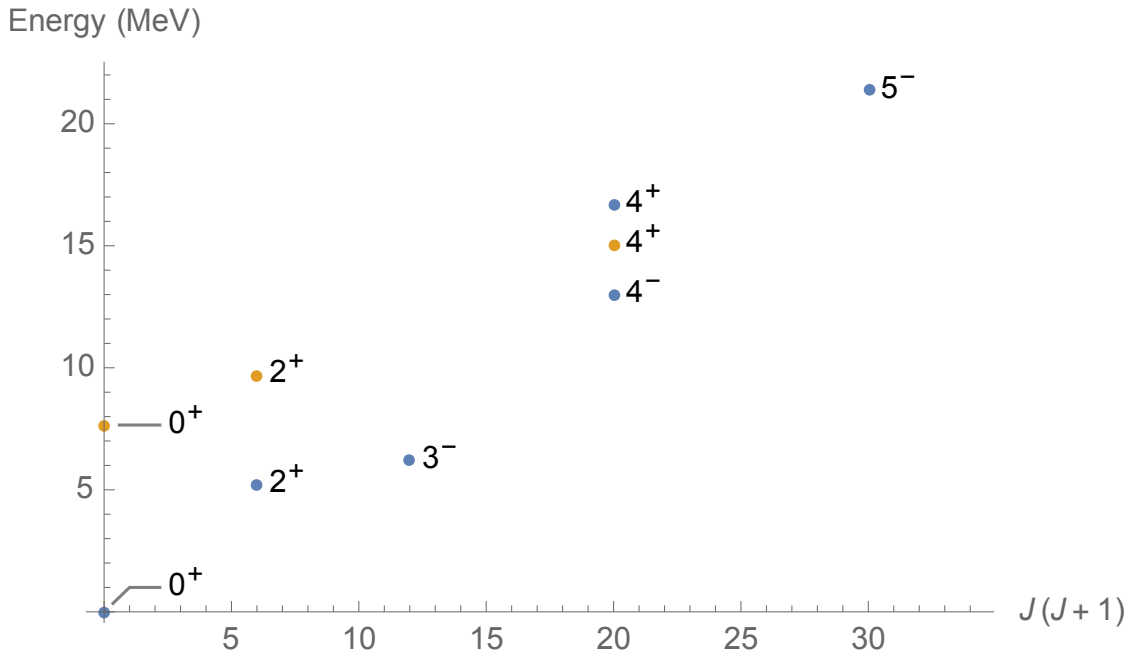
Figure 3.6: Energy spectrum in the rigid body regime.

The rigid body picture is inadequate as it is unable to explain the experimentally observed

40

low-lying 1^- and 2^- states, both of which are known to have energies less than 15 MeV. In this asymptotic regime, the wavefunctions become concentrated on either the equilateral triangle (blue, often referred to as the ground state band) or the linear chain (yellow, often referred to as the Hoyle band) for spins and parities that are allowed at those shapes. Recall that the energy levels of a symmetric top (having moments of inertia $V_{11} = V_{22}$, V_{33}) are given by

$$E = \frac{1}{2V_{11}} J(J+1) + \left(\frac{1}{2V_{33}} - \frac{1}{2V_{11}} \right) L_3^2. \tag{3.21}$$

The Hoyle band states in the plot all have body-fixed spin projection $|L_3| = 0$ and so the corresponding energy values lie on a straight line. The ground state band includes states with $|L_3| = 0$ and $|L_3| = 3$, with the $|L_3| = 0$ states lying on a straight line and the $|L_3| = 3$ states just below this line. Some examples of these wavefunctions are in Figure 3.7.
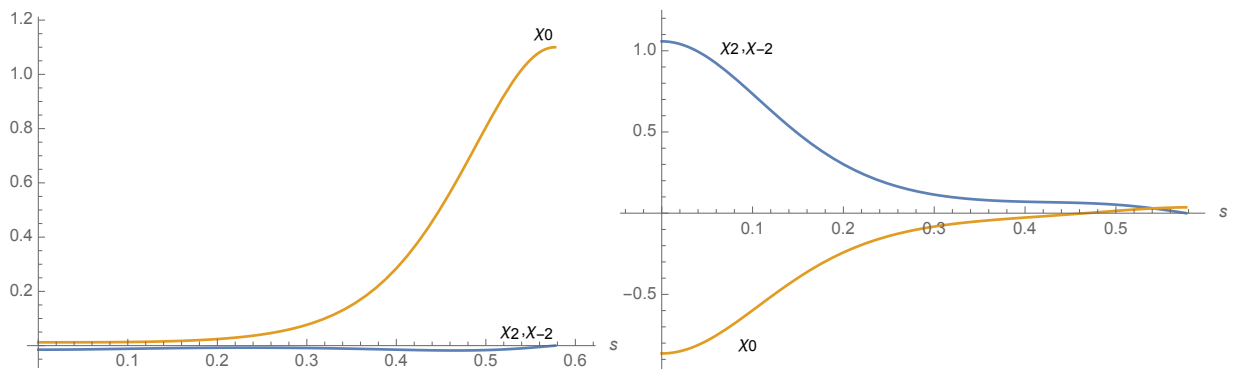
Figure 3.7: Wavefunctions of the lowest-lying 2^+ states in the rigid body regime, concentrated on the equilateral triangle (left) and the linear chain (right).

Our model allows additional states, including spin and parity combinations such as 1^-, 2^- and 3^+. These new states have the same quantum numbers as (some of) those found by the ACM approach [36]. However, in the rigid body regime, they have high energy since they must vanish at both the equilateral triangle and linear chain. They are peaked at intermediate configurations which have very high energy.

3.5.2   Results

Starting from parameters corresponding to the rigid body regime, we consider the effect of lowering the size of the barrier. States concentrated at the equilateral triangle or the linear chain start to mix if they have the same quantum numbers. This means that the 0^+ and 2^+ states concentrated at the equilateral triangle become a superposition of triangular and linear chain states (Figure 3.8). Very little mixing can occur for states such as the 3^- and 5^-, however, as they are only allowed at the equilateral triangle and not at the linear chain
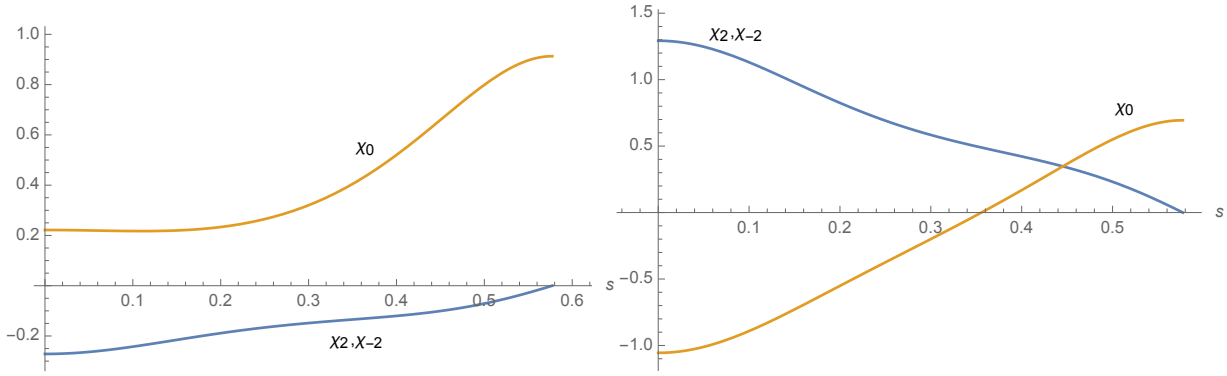
Figure 3.8: Wavefunction of the lowest-lying 2^+ states: these correspond to superpositions of the equilateral triangle and linear chain states in Figure 3.7, reflecting the relaxation of the rigid body assumption.

(Figure 3.9).
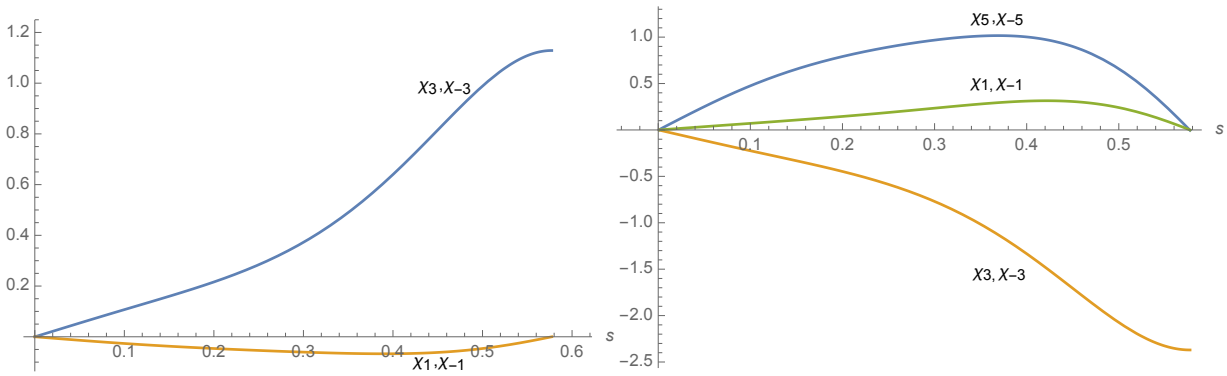
Figure 3.9: Wavefunctions of the 3^- state and the 5^- state. Note that they must vanish at the linear chain $s = 0$.

The energy of the new 1^- state decreases and we stop lowering the barrier when the experimental value is reached. The final spectrum is displayed in Figure 3.10.

This is a significant improvement on the rigid body spectrum previously discussed. Many observed states that were missing are now present. These include the low-lying 1^- and 2^- states as well as a second 3^- state and a third 2^+ state slightly higher up (Figure 3.11). The spectrum also includes a 3^+ state and a 4^-, 4^+ pair (at energies 19.8 MeV, 21.3 MeV and 22.2 MeV), which have not yet been observed experimentally. There is an approximate correspondence between these states and the ACM rotational band labelled by $\left(v_1, v_2^{l_2}\right) = (0, 1^1)$, which has the same sequence of allowed spin and parity combinations. In the ACM picture, these states are associated with the doubly degenerate vibration of the equilateral triangle with E symmetry (with $v_2 = 1$ denoting one unit of vibrational excitation).

Our wavefunctions give further insight into the nature of the excited states. The 1^-,
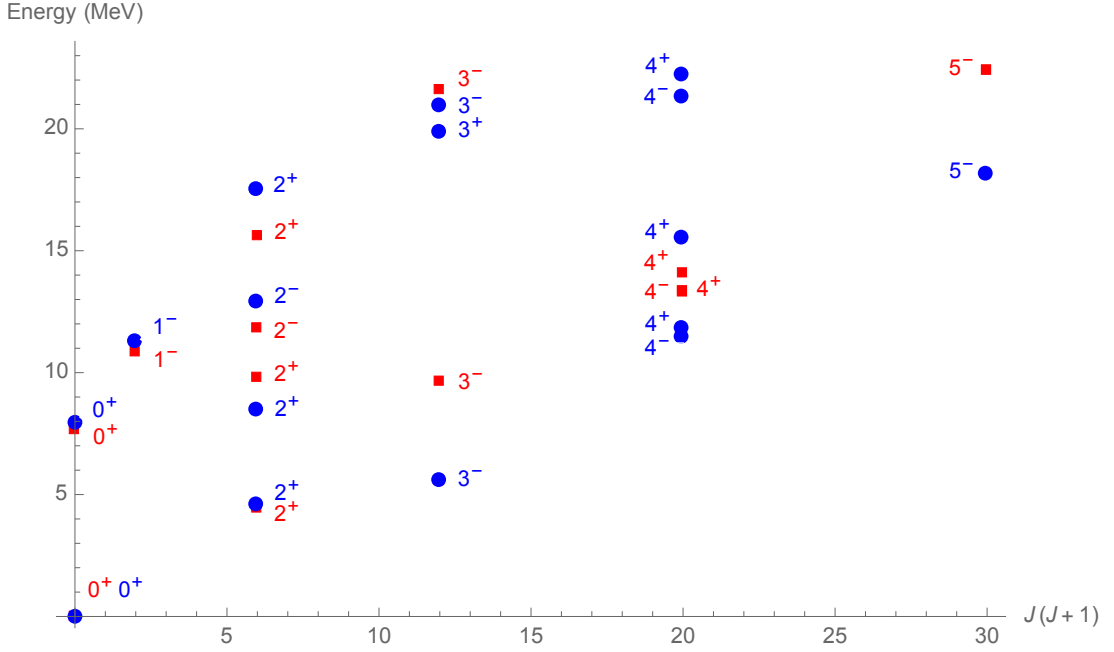
Figure 3.10: Spectrum of our model (blue points) compared to experimental data (red points).
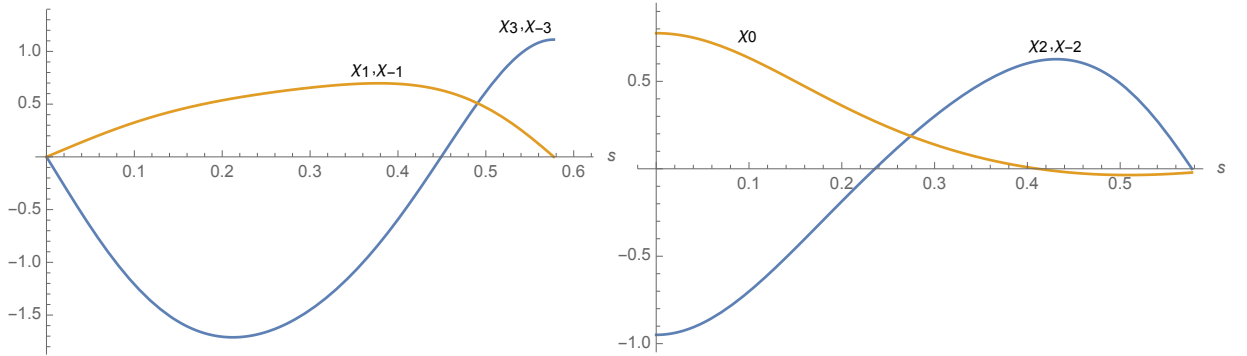
Figure 3.11: Wavefunctions of the second 3^- state and the third 2^+ state.

2^- and 3^+ are concentrated at a bent arm configuration (Figure 3.12), a shape between the equilateral triangle and the linear chain in our configuration space. They vanish at the equilateral triangle and the linear chain, with their wavefunction peaking at $s \approx 0.4$ which corresponds to an approximately right-angled triangle. The different spins correspond to rotational excitations of such a state.

The remaining low-lying states do involve the equilateral triangle and the linear chain. The wavefunctions of the 0^+ ground state and the 0^+ Hoyle state are plotted in Figure 3.13. It is interesting to compare these wavefunctions with the findings of recent lattice calculations [32] which suggest the 0^+ ground state and the 0^+ Hoyle state have a strong overlap with a compact triangular and a bent arm configuration respectively. Our wavefunctions are consistent with this picture: the ground state wavefunction peaks at the equilateral triangle

43
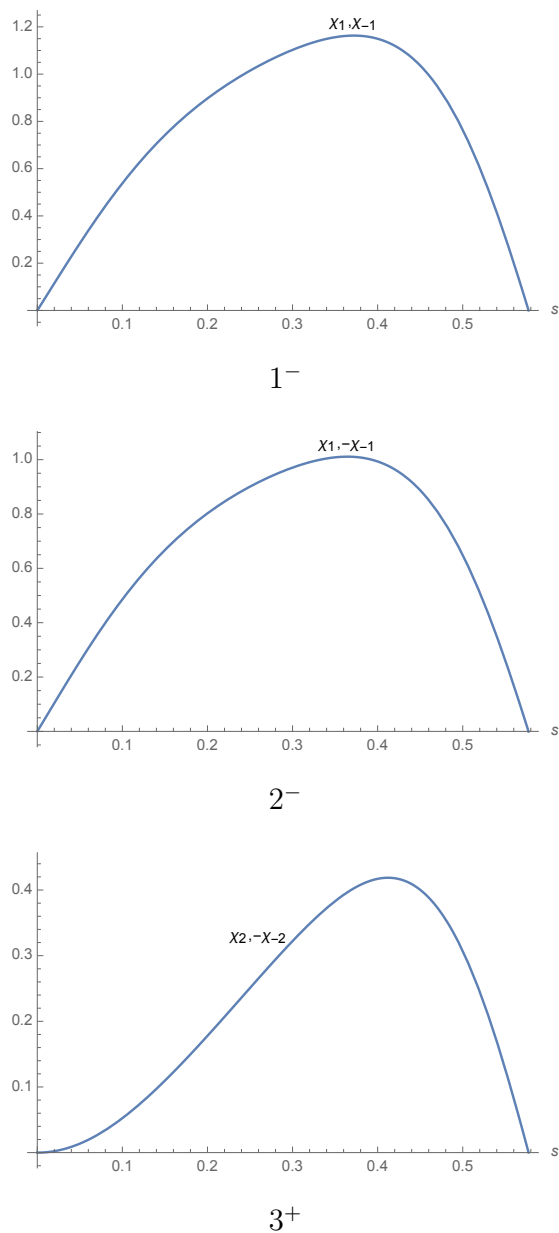
Figure 3.12: Wavefunctions of the lowest 1^-, 2^- and 3^+ states.

and falls away fairly rapidly towards the linear chain, while the Hoyle state wavefunction peaks at the linear chain and is more spread out, remaining significant over a range of bent arm configurations.

3.6 Conclusions

We have improved upon a previous analysis which attempted to explain the low-lying spectrum of Carbon-12 in terms of a rigidly rotating equilateral triangle or linear chain [27]. This
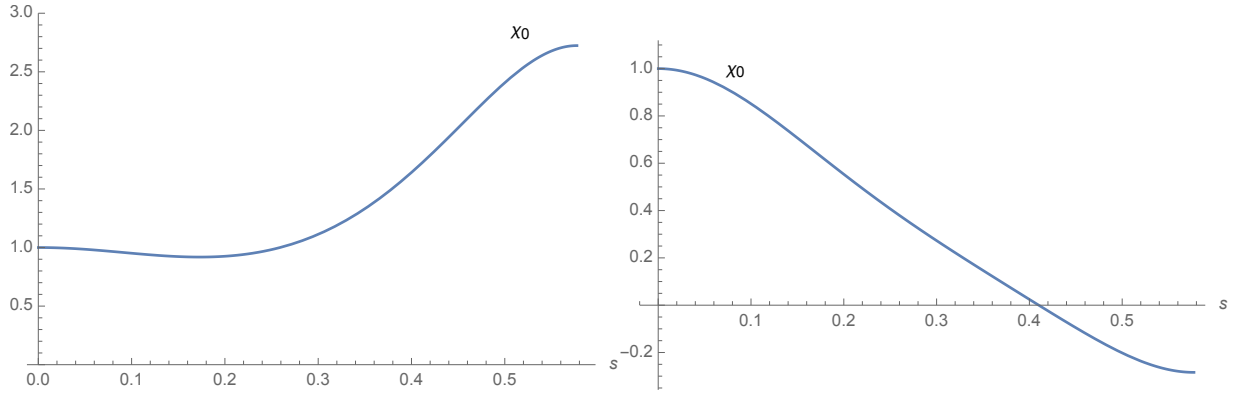
Figure 3.13: Wavefunctions of the 0^+ ground state (left) and the 0^+ Hoyle state (right).

analysis assumed a high degree of symmetry for the configurations relevant at low energies, leading to very few low-lying states and missing out several spin and parity combinations. By contrast, a model based on a local analysis of small vibrations leads to a spectrum with too many low-lying states [36].

These problems are resolved once we allow shapes which interpolate between the equilateral triangle and the linear chain. The model presented in this chapter, which utilises QGT, takes larger deformations seriously and gives us a different picture of the excited states. States which were considered independent in the rigid body picture can mix in our model, leading to superpositions of equilateral triangular and linear chain states. Other states which were not present in the rigid body picture have wavefunctions peaked at an intermediate bent arm configuration, rather than looking like a vibrational excitation of an equilateral triangle. We also predict three new energy levels for the Carbon-12 nucleus at around 20 MeV, with spin and parity combinations 3^+, 4^- and 4^+.

Chapter 4

Electromagnetic transition rates of Carbon-12 and Oxygen-16 in rovibrational models

This chapter is based on the joint paper with C. J. Halcrow [40].

4.1 Introduction

Understanding the intrinsic structure of nuclei is one of the central problems in nuclear physics. There is still much debate about the nature of light nuclei, even for stable abundant nuclei such as Carbon-12 and Oxygen-16. These are often described using α-particle models [6]. Here, nucleons cluster into groups of four (α-particles) and the nuclei have the symmetry of a simple geometric shape – the α-particles lying on the shape's vertices. Carbon-12 and Oxygen-16 are described as a triangle and tetrahedron respectively. The triangular model, as discussed in the previous chapter, includes a low lying rotational band with spins $0^+, 2^+, 3^-, 4^\pm, ...$ for Carbon-12 while the tetrahedral model has one with spins $0^+, 3^-, 4^+, ...$ for Oxygen-16. Both are seen experimentally, confirmed after the recent clarification of a 4^- state at 11.83 MeV for Carbon-12 [41]. There is much debate about the higher energy states. For example, Carbon-12 has an approximate higher energy rotational band with spins $0^+, 2^+, 4^+, ...$. In Chapter 3 we modelled this band in terms of admixtures of several shapes but other suggestions include a "breathing" excitation of the triangle [33] or a chain of α-particles [31]. All these models can reproduce the energy spectrum reasonably well.

Rotational bands are not the only indicator of collective, geometric behaviour. Electromagnetic (EM) transition rates measure γ-decay between two nuclear states. Here, the higher energy state emits a photon which carries away spin and energy. This type of electromagnetic decay is only seen below (or nearby) the strong decay threshold. Above this threshold, strong

interactions dominate the decay paths. Theoretically the EM rates depend on the overlap of wavefunctions and the charge density multipole tensor. Generically, a large transition rate indicates collective behaviour. For instance, the large E3 transition rate between the low lying 3^- and 0^+ states of Oxygen-16 is a motivation for the continuing interest in α-particle models [42]. Its size is unexplained in the basic shell model, where the decay strength should be close to a single Weisskopf unit. Its size is also not described in basic collective models, where the nucleus is described as a vibrating bag of nuclear matter [43].

Just as the EM transitions can help differentiate collective behaviour from single-particle behaviour, in this paper we will try and use them to differentiate between particular α-particle models. Since the transition rates depend on the structure of the wavefunctions, physically different models should provide different results. To see these differences, we calculate the EM rates for the Quantum Graph Model (QGM) for Carbon-12 and a recently proposed model for Oxygen-16 [7], both of which were inspired by nuclear dynamics in the Skyrme model. In these, sets of configurations are constructed which include several low lying shapes: the triangle and chain for Carbon-12 and the tetrahedron and square for Oxygen-16. The wavefunctions take values across the entire set of shapes, and can be interpreted physically as mixtures of the different geometric shapes.

The wavefunctions are rotational-vibrational states. The rotational symmetry of space manifests itself through rigid body wavefunctions and these are combined with vibrational wavefunctions, which account for deformations. We develop a formalism to calculate the transition rates for wavefunctions of this kind. The formalism applies to any model with an underlying "shape" degree of freedom. The rigid-body case, a common simplifying assumption in the Skyrme model [44] and α-particle models [45], is a limiting case in our calculation. After developing this formalism in Section 4.2, we apply it to models of Carbon-12 and Oxygen-16 in Sections 4.3 and 4.4 respectively. These applications show the general nature of our work. The models are based on very different shape spaces: one is a one-dimensional graph made up of three edges joined at a single vertex while the other is a two-dimensional manifold. We compare our results to experimental data, as well as other nuclear models. Overall, each model gives very different results with different successes and failures when compared to data. We hope this theoretical work may motivate new experimental progress, as the latest data was taken in the early 1980s [46, 47]. We conclude with some further work and ideas in Section 4.5.

4.2   General formalism

We wish to describe nuclear dynamics by considering a large set of nuclear configurations with many possible shapes (the shape can be thought of as the nucleon distribution). We then choose a low energy subset of these configurations which we parametrise by a set of shape

coordinates **s**. We also consider all possible orientations of these configurations in physical space. Define coordinates as follows: for each shape, choose a certain standard orientation of that shape in space (equivalently, a body-fixed frame). Then parametrise all rotated versions of that shape by Euler angles θ_i which specify the rotation that relates the body-fixed frame to a space-fixed frame. In this fashion, we can define coordinates $(\mathbf{s}, \theta_i)$.

The rotational symmetry of space means that quantum states can be classified by a total angular momentum J together with a space-fixed angular momentum projection $J_3 \in \{-J, \ldots, +J\}$. States $|\Psi\rangle$ within a given (J, J_3) sector take the form

$$|\Psi\rangle = \sum_{L_3=-J}^{+J} \chi_{L_3}(\mathbf{s}) |JJ_3L_3\rangle \,, \tag{4.1}$$

where we have expanded in a basis $\{|JJ_3L_3\rangle\}$ of rigid-body wavefunctions which involve the body-fixed angular momentum projection $L_3 \in \{-J, \ldots, +J\}$. These capture the θ_i dependence of the state. The coefficient wavefunctions $\chi_{L_3}(\mathbf{s})$ satisfy a Schrödinger equation defined on the space of shapes. We will see examples of this in the specific models for Carbon-12 and Oxygen-16 considered in Sections 4.3 and 4.4.

4.2.1 Electromagnetic transition rates

In the long-wavelength limit, the reduced transition probability for electric multipole radiation between an initial state $|i\rangle$ of spin J and a final state $|f\rangle$ of spin $\tilde{J}$ is given by

$$B(El, i \to f) = \frac{1}{2J+1} \sum_{J_3, \tilde{J}_3, m} \left| \int d^3r \, \langle f| \, \rho(\mathbf{s}, \mathbf{r}, \theta_i) \, r^l Y_{lm}^*(\Omega) |i\rangle \right|^2 \tag{4.2}$$

where $\mathbf{r}$ are space-fixed coordinates (with Ω the angular coordinates in $\mathbf{r}$-space) and where $\rho(\mathbf{s}, \mathbf{r}, \theta_i)$ is the charge density of the configuration with shape $\mathbf{s}$ in orientation θ_i. Note that the above expression involves a sum over space-fixed spin projections $\tilde{J}_3$ for the final state and an average over space-fixed spin projections J_3 for the initial state. The quantity $B(El, i \to f)$ is related to the total transition rate $T(E, i \to f)$ (decays per second) for electric multipole radiation by

$$T(E, i \to f) = \sum_l \frac{8\pi(l+1)}{l[(2l+1)!!]^2} \frac{k^{2l+1}}{\hbar} B(El, i \to f) \tag{4.3}$$

where k is the wavenumber of the emitted photon. This sum is dominated by the contribution from the lowest-allowed l [48] for each transition and so we only calculate these.

We wish to calculate transition probabilities using (4.2) for states of the form (4.1). The rigid-body wavefunctions $|JJ_3L_3\rangle$ depend on Euler angles θ_i and so it will help if we first

simplify the θ_i dependence of the charge density ρ. Expand ρ, evaluated at $\theta_i = 0$, in terms of spherical harmonics:

$$\rho\left(\mathbf{s}, \mathbf{r}, \mathbf{0}\right) = \sum_{l'=0}^{\infty} \sum_{m'=-l'}^{l'} c_{l'm'}\left(r\right) Y_{l'm'}\left(\Omega\right) \tag{4.4}$$

where

$$c_{l'm'}\left(r\right) = \int d\Omega \, Y_{l'm'}^*\left(\Omega\right) \rho\left(\mathbf{s}, \mathbf{r}, \mathbf{0}\right). \tag{4.5}$$

The spherical harmonics transform in a simple way under rotations, giving the expression

$$\rho\left(\mathbf{s}, \mathbf{r}, \theta_i\right) = \sum_{l'} \sum_{m'} \sum_{m''} c_{l'm'}\left(r\right) Y_{l'm''}\left(\Omega\right) D_{m''m'}^{l'}\left(\theta_i\right) \tag{4.6}$$

for the charge density in an arbitrary orientation θ_i. Substituting this into our original expression for $B\left(El, i \rightarrow f\right)$ gives

$$B\left(El, i \rightarrow f\right) = \frac{1}{2J+1} \sum_{J_3, \tilde{J}_3, m} \left| \langle f | \sum_{m'} D_{mm'}^l\left(\theta_i\right) \mathcal{Q}_{lm'}\left(\mathbf{s}\right) | i \rangle \right|^2 \tag{4.7}$$

where

$$\mathcal{Q}_{lm}\left(\mathbf{s}\right) = \int d^3r \, \rho\left(\mathbf{s}, \mathbf{r}, \mathbf{0}\right) r^l Y_{lm}^*\left(\Omega\right) \tag{4.8}$$

is the multipole tensor associated with the charge density. This means that, for the initial state

$$|i\rangle = \sum_{L_3=-J}^{+J} \chi_{L_3}\left(\mathbf{s}\right) |JJ_3L_3\rangle \tag{4.9}$$

and final state

$$|f\rangle = \sum_{\tilde{L}_3=-\tilde{J}}^{+\tilde{J}} \tilde{\chi}_{\tilde{L}_3}\left(\mathbf{s}\right) |\tilde{J}\tilde{J}_3\tilde{L}_3\rangle, \tag{4.10}$$

we have that

$$B\left(El, i \to f\right) = \frac{1}{2J+1} \sum_{J_3, \tilde{J}_3, m} \left| \sum_{m'} \langle f | D^l_{mm'}\left(\theta_i\right) \mathcal{Q}_{lm'}\left(\mathbf{s}\right) | i \rangle \right|^2$$

$$= \frac{1}{2J+1} \sum_{J_3, \tilde{J}_3, m} \left| \int d\mathbf{s} \sum_{m', L_3, \tilde{L}_3} \tilde{\chi}^*_{\tilde{L}_3}\left(\mathbf{s}\right) \chi_{L_3}\left(\mathbf{s}\right) \mathcal{Q}_{lm'}\left(\mathbf{s}\right) \langle \tilde{J} \tilde{J}_3 \tilde{L}_3 | D^l_{mm'}\left(\theta_i\right) | J J_3 L_3 \rangle \right|^2$$

$$= \frac{2\tilde{J}+1}{(2J+1)^2} \sum_{J_3, \tilde{J}_3, m} \left| \int d\mathbf{s} \sum_{m', L_3, \tilde{L}_3} \tilde{\chi}^*_{\tilde{L}_3}\left(\mathbf{s}\right) \chi_{L_3}\left(\mathbf{s}\right) \mathcal{Q}_{lm'}\left(\mathbf{s}\right) \langle \tilde{J} \tilde{J}_3 lm | J J_3 \rangle \langle \tilde{J} \tilde{L}_3 lm' | J L_3 \rangle \right|^2$$

$$= \frac{2\tilde{J}+1}{2J+1} \left| \int d\mathbf{s} \sum_{m', L_3, \tilde{L}_3} \tilde{\chi}^*_{\tilde{L}_3}\left(\mathbf{s}\right) \chi_{L_3}\left(\mathbf{s}\right) \mathcal{Q}_{lm'}\left(\mathbf{s}\right) \langle \tilde{J} \tilde{L}_3 lm' | J L_3 \rangle \right|^2 \tag{4.11}$$

where $\langle \tilde{J} \tilde{J}_3 lm | J J_3 \rangle$ are Clebsch-Gordan coefficients and in the final equality we have used the fact that

$$\sum_{J_3, \tilde{J}_3, m} \left| \langle \tilde{J} \tilde{J}_3 lm | J J_3 \rangle \right|^2 = 2J+1 \tag{4.12}$$

whenever $J = \tilde{J}+l, \ldots, |\tilde{J}-l|$. For values of J outside of this range, the Clebsch-Gordan coefficients all vanish and the transition rate is zero. We have now written the original expression in terms of an overlap between vibrational wavefunctions, weighted by the charge density multipole tensor and some Clebsch-Gordan coefficients. All these are relatively straightforward to calculate, even if the expression is rather complicated. Note that for $\tilde{J} = 0$ the expression (2.10) simplifies (using $\langle 00 lm' | J L_3 \rangle = \delta_{Jl} \delta_{L_3 m'}$) to give

$$B\left(El, i \to f\right) = \frac{\delta_{Jl}}{2J+1} \left| \int d\mathbf{s} \, \tilde{\chi}^*_0\left(\mathbf{s}\right) \sum_{L_3} \chi_{L_3}\left(\mathbf{s}\right) \mathcal{Q}_{lL_3}\left(\mathbf{s}\right) \right|^2 , \tag{4.13}$$

which mimics the structure of the initial wavefunction (4.9).

We also note here that

$$B\left(El, f \to i\right) = \frac{2J+1}{2\tilde{J}+1} \left| \int d\mathbf{s} \sum_{m', L_3, \tilde{L}_3} \tilde{\chi}^*_{L_3}\left(\mathbf{s}\right) \chi_{\tilde{L}_3}\left(\mathbf{s}\right) \mathcal{Q}_{lm'}\left(\mathbf{s}\right) \langle J L_3 lm' | \tilde{J} \tilde{L}_3 \rangle \right|^2$$

$$= \left| \int d\mathbf{s} \sum_{m', L_3, \tilde{L}_3} \tilde{\chi}^*_{L_3}\left(\mathbf{s}\right) \chi_{\tilde{L}_3}\left(\mathbf{s}\right) \mathcal{Q}_{lm'}\left(\mathbf{s}\right) (-1)^{m'} \langle \tilde{J} \tilde{L}_3 l \left(-m'\right) | J L_3 \rangle \right|^2$$

$$= \frac{2J+1}{2\tilde{J}+1} B\left(El, i \to f\right) , \tag{4.14}$$

where we have used symmetry properties of the Clebsch-Gordan coefficients together with

the identity $Y_{lm}^* (\Omega) = (-1)^m Y_{l(-m)} (\Omega)$.

4.2.2 Estimating $\mathcal{Q}$ for point α-particle models

The nuclear models we will consider in Sections 4.3 and 4.4 are based on configurations of α-particles. For the purposes of calculating electromagnetic transition rates, we will treat these α-particles as point charges. For α-particles at positions $\mathbf{x}_1 (\mathbf{s}), \ldots, \mathbf{x}_N (\mathbf{s})$, we therefore approximate the charge density by

$$\rho (\mathbf{s}, \mathbf{r}, \mathbf{0}) = \sum_{i=1}^{N} 2 \delta^{(3)} (\mathbf{x}_i (\mathbf{s}) - \mathbf{r}). \tag{4.15}$$

This leads to the multipole tensor

$$\mathcal{Q}_{lm} (\mathbf{s}) = \sum_{i=1}^{N} 2 x_i (\mathbf{s})^l Y_{lm}^* (\hat{\mathbf{x}}_i (\mathbf{s})). \tag{4.16}$$

4.3 The Quantum Graph Model for Carbon-12

4.3.1 Introduction

In Chapter 3 we introduced the Quantum Graph Model (QGM) for Carbon-12 which is based on the quantized dynamics of three point α-particles. We recall some of the details of the model here. The QGM allows for isosceles triangles of α-particles which interpolate between the equilateral triangle and linear chain clusters and so includes both of these highly symmetric configurations along with the intermediate bent arm (obtuse triangle) configurations. There are three ways in which an equilateral triangle cluster of α-particles can be deformed into a chain because any one of the three α-particles can become the middle α-particle in the chain. Thus the space of allowed shapes corresponds to a three-edged graph as shown in Figure 4.1.

The equilateral triangle corresponds to the vertex of the graph. The equilateral triangle can deform in three ways, corresponding to the three edges leaving the vertex. Focusing on a particular edge, $\mathcal{C}_1$, we define a shape coordinate s on this edge such that the positions $\mathbf{x}_i (s)$ of the three α-particles are

$$\mathbf{x}_1 = (0, s, 0) \tag{4.17}$$

$$\mathbf{x}_2 = \left(-\frac{1}{2} \sqrt{2 - 3s^2}, -\frac{1}{2} s, 0 \right) \tag{4.18}$$

$$\mathbf{x}_3 = \left(\frac{1}{2} \sqrt{2 - 3s^2}, -\frac{1}{2} s, 0 \right). \tag{4.19}$$
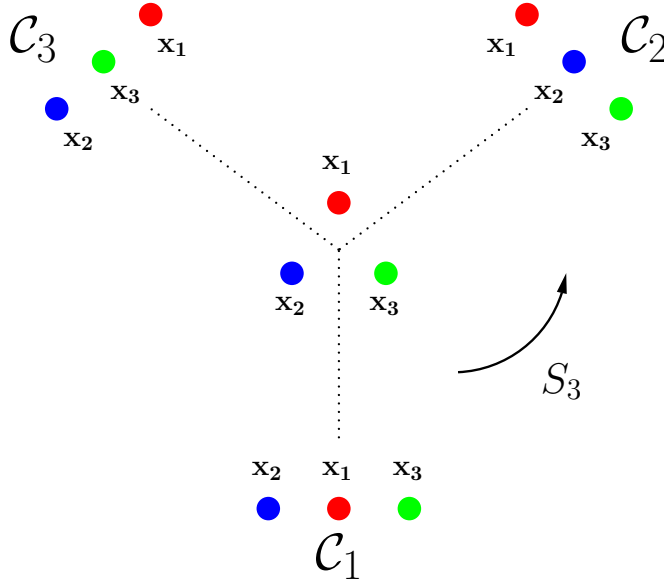
Figure 4.1: The graph of shapes for the QGM of Carbon-12. The central shape is an equilateral triangle. This becomes three different chains along the three graph edges.

The $\mathbf{x}_i$ determine the standard orientation at the point s on the graph. We use coordinates (s, θ_i) with Euler angles θ_i describing the rotation relating a given configuration to these standard configurations. The wavefunction on edge $\mathcal{C}_1$ can be expanded in terms of rigid body states as

$$|\Psi\rangle = \sum_{L_3=-J}^{+J} \chi_{L_3}(\mathbf{s}) |JJ_3L_3\rangle \tag{4.20}$$

where the χ_{L_3} satisfy a Schrödinger equation, and QGT boundary conditions are imposed at the vertex.

The allowed states, relevant for our calculation, are listed in Table 4.1. For each state, we calculate a shape probability density, defined as

$$P_\Psi(\boldsymbol{s}) = \sum_{L_3=-J}^{J} |\chi_{L_3}(\boldsymbol{s})|^2 . \tag{4.21}$$

We plot the shape probability density function for each of the wavefunctions in Figure 4.2. The physical interpretation of states can be seen by looking at which shapes these are concentrated at. For example, the 0_1^+ state is interpreted as an equilateral triangular state while the 0_2^+ state is concentrated at the linear chain. The 1_1^- state is forbidden at both of these shapes and is instead concentrated at an intermediate bent arm configuration.

J^P	Wavefunction	E (MeV)	E_{exp} (MeV)
0_1^+	$\chi_0^{(0_1)}(s)\,\lvert 0,0\rangle$	0	0
0_2^+	$\chi_0^{(0_2)}(s)\,\lvert 0,0\rangle$	7.9	7.7
1_1^-	$\chi_1^{(1_1)}(s)\,(\lvert 1,1\rangle + \lvert 1,-1\rangle)$	11.2	10.8
2_1^+	$\chi_2^{(2_1)}(s)\,(\lvert 2,2\rangle + \lvert 2,-2\rangle) + \chi_0^{(2_1)}(s)\,\lvert 2,0\rangle$	4.6	4.4
2_2^+	$\chi_2^{(2_2)}(s)\,(\lvert 2,2\rangle + \lvert 2,-2\rangle) + \chi_0^{(2_2)}(s)\,\lvert 2,0\rangle$	8.4	9.9
2_3^+	$\chi_2^{(2_3)}(s)\,(\lvert 2,2\rangle + \lvert 2,-2\rangle) + \chi_0^{(2_3)}(s)\,\lvert 2,0\rangle$	17.4	16.1
3_1^-	$\chi_3^{(3_1)}(s)\,(\lvert 3,3\rangle + \lvert 3,-3\rangle) + \chi_1^{(3_1)}(s)\,(\lvert 3,1\rangle + \lvert 3,-1\rangle)$	5.6	9.6
4_1^+	$\chi_4^{(4_1)}(s)\,(\lvert 4,4\rangle + \lvert 4,-4\rangle) + \chi_2^{(4_1)}(s)\,(\lvert 4,2\rangle + \lvert 4,-2\rangle)$ $+\chi_0^{(4_1)}(s)\,\lvert 4,0\rangle$	11.8	13.3
4_2^+	$\chi_4^{(4_2)}(s)\,(\lvert 4,4\rangle + \lvert 4,-4\rangle) + \chi_2^{(4_2)}(s)\,(\lvert 4,2\rangle + \lvert 4,-2\rangle)$ $+\chi_0^{(4_2)}(s)\,\lvert 4,0\rangle$	15.6	14.1

Table 4.1: The wavefunctions, in terms of vibrational wavefunctions and spin states, for each of the states considered in this chapter. Each model state is identified with an experimental state, whose energy is also tabulated. We suppress the J_3 label for ease of reading.
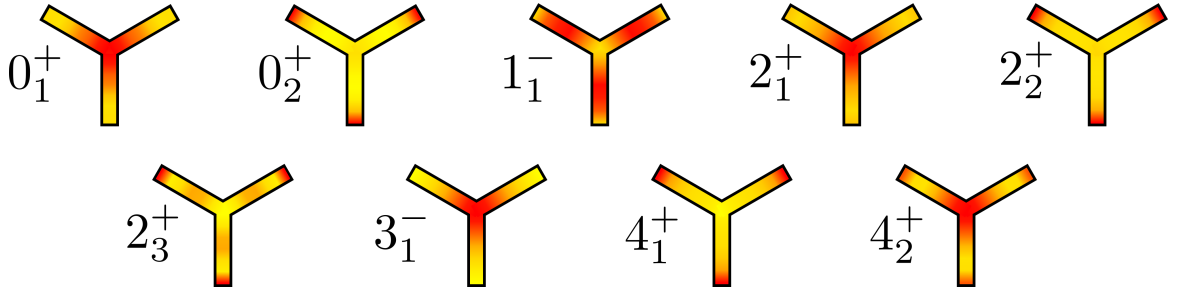
Figure 4.2: Shape probability densities. The colours red and yellow correspond to regions of high and low probability density. Each density is rescaled so that the maximum of the wavefunction is red. Hence, for example, the 0_2^+ state is highly concentrated while the 1_1^- state is more evenly spread.

4.3.2 Calculating $B(El)$ transition rates

As an example, suppose we are interested in calculating $B\left(E3, 3_1^- \to 0_1^+\right)$ where 3_1^- denotes the lowest energy $J^P = 3^-$ state and 0_1^+ denotes the lowest $J^P = 0^+$ state. The initial and final state wavefunctions are

$$\lvert 3_1^-\rangle = \chi_3^{(3_1)}(s)\,(\lvert 3J_3 3\rangle + \lvert 3J_3 -1\rangle) + \chi_1^{(3_1)}(s)\,(\lvert 3J_3 1\rangle + \lvert 3J_3 -1\rangle) \tag{4.22}$$

and

$$\lvert 0_1^+\rangle = \chi_0^{(0_1)}(s)\,\lvert 000\rangle. \tag{4.23}$$

The expression (2.10) from Section 2 gives

$$B\left(E3, 3_1^- \to 0_1^+\right) = \frac{1}{7} \left| \int ds\, \chi_0^{(0_1)^*}(s)\, \chi_3^{(3_1)}(s) \left(\mathcal{Q}_{33}(s) + \mathcal{Q}_{3-3}(s)\right) \right.$$

$$\left. + \chi_0^{(0_1)^*}(s)\, \chi_1^{(3_1)}(s) \left(\mathcal{Q}_{31}(s) + \mathcal{Q}_{3-1}(s)\right) \right|^2. \tag{4.24}$$

To evaluate this integral we use the analytic expression for

$$\mathcal{Q}_{lm}(s) = \sum_{i=1}^{3} 2R_i(s)^l\, Y_{lm}^*(\hat{\mathbf{x}}_i(s))\,, \tag{4.25}$$

treating the α-particles as point particles as described in Section 2. The integration against the numerical wavefunctions $\chi_{L_3}(s)$ takes place over a single edge of the graph.

4.3.3 Results

The electromagnetic transition rates for the QGM are displayed in Table 4.2. We pick the conversion factor between fm and the length units in our model to be $\kappa = \sqrt{10}$. Our results are displayed alongside results from an ab initio calculation [32] and the Algebraic Cluster Model (ACM) [33], along with a comparison to available experimental data. The ACM makes use of a bosonic quantization approach to the many-body problem. It is based on an equilibrium configuration of α-particles at the vertices of an equilateral triangle, although allowing for large rotation-vibration effects. The ab initio results are from Monte Carlo lattice calculations based on chiral effective field theory. The authors only consider four states: 0_1^+, 2_1^+, 0_2^+ and 2_2^+. The 0_1^+ and 2_1^+ states have a large overlap with a compact triangular arrangement of α-particles, so are interpreted physically as triangular states. In particular, the 2_1^+ is interpreted as a rotational excitation of the 0_1^+ state. The 0_2^+ and 2_2^+ states have a large overlap with a bent arm configuration (an obtuse triangle) of α-particles and are interpreted as the first two states on a rotational band of this shape.

Along the ground state band (0_1^+, 2_1^+, 3_1^-, ...) there is no major discrepancy between the various models. The agreement is expected as all the models have a similar interpretation of the ground state band as arising from a rotating equilateral triangle. The results along the ground state band are also in broad agreement with experimental data, although all models slightly underestimate the $E3$ transition.

The $B\left(E1, 2^+ \to 3^-\right)$ and $B\left(E1, 2^+ \to 1^-\right)$ transition strengths come out as zero in our model due to the symmetries of the wavefunctions. This is consistent with the very small observed values $\sim 10^{-3}\, e^2\text{fm}^2$. For the states that have been experimentally measured, there is little to distinguish the models. Because of this, we must instead look at transitions for

54

$B\left(El, i \to f\right)$	QGM $\left(\kappa = \sqrt{10}\right)$	ab initio [32]	ACM [33]	experiment $\left[e^2\text{fm}^{2l}\right]$[46]
$B\left(E2, 2_1^+ \to 0_1^+\right)$	11.7	5	8.4	7.6 ± 0.42
$B\left(E3, 3_1^- \to 0_1^+\right)$	62.4		44	103 ± 13.7
$B\left(E4, 4_1^+ \to 0_1^+\right)$	170		73	
$B\left(E2, 2_2^+ \to 0_1^+\right)$	1.16	2		
$B\left(E4, 4_2^+ \to 0_1^+\right)$	11.6			
$B\left(E2, 2_3^+ \to 0_1^+\right)$	0.408			0.67 ± 0.13
$B\left(E2, 2_1^+ \to 0_2^+\right)$	1.10	1.5	0.26	2.7 ± 0.28
$B\left(E2, 2_2^+ \to 0_2^+\right)$	24.7	6		
$B\left(E1, 2_3^+ \to 1_1^-\right)$	0			$(3.1 \pm 0.78) \times 10^{-3}$
$B\left(E1, 2_3^+ \to 3_1^-\right)$	0			$(1.1 \pm 0.20) \times 10^{-3}$
$B\left(E1, 2_1^+ \to 3_1^-\right)$	0			

Table 4.2: EM transition rates $B\left(El, i \to f\right)$ for Carbon-12. We tabulate the results for the model described in this section, the ab initio calculation and the algebraic cluster model, as well as the available experimental data. All values are in units of $e^2\text{fm}^{2l}$.

states that have not yet been measured. The $B(E2; 2_2^+ \to 0_2^+)$ transition is four times larger for us compared to the ab initio prediction. We expect the transition will also be smaller in the ACM. This transition is, therefore, a key data point which would distinguish the various models.

The most significant difference between experiment and theory is seen for the transition between the Hoyle state and the ground state band $B\left(E2, 2_1^+ \to 0_2^+\right)$. Here the ACM value is too small by a factor of 10 or so. Our model and the ab initio calculation do better than the ACM here, although we still underestimate the value slightly. Recall that the ab initio approach finds a large overlap of the Hoyle state with an obtuse triangular configuration. Our work supports this interpretation, with the 0_2^+ wavefunction peaking at the linear chain but allowing a superposition of shapes near to the chain. The picture in the ACM is different, with the Hoyle state interpreted as a breathing excitation of the equilateral triangle. More data is needed, both experimental and from competing models, to make further comparisons and we hope that our calculations will stimulate further work in this direction.

4.4   Oxygen-16

Since Wheeler's pioneering work, Oxygen-16 has often been modelled as a tetrahedron of α-particles [6]. Later, sophisticated α-models found that other low energy geometric configurations exist, including the 4α-chain, the flat square and the bent square [49]. There is general agreement on the tetrahedral nature of the 0^+ ground state of Oxygen-16, but the structure of the excited states continues to pose a challenge for nuclear physicists. The lowest excitation is a 0^+ state, analogous to the Hoyle state of Carbon-12, and various suggestions

have been made for its structure including a breathing mode excitation of the tetrahedron or a state based on a flat square or bent rhomb configuration.

A recent α-particle model constructed by Halcrow, King and Manton [7] includes all of these shapes. We give a brief review of the model here. Like the QGM for Carbon-12, it is inspired by Skyrme field configurations which have a clear interpretation in terms of α-particles. Consider the dynamical mode illustrated in Figure 4.3. Reading the figure from left to right, two pairs of α-particles approach each other and form a tetrahedron, then a flat square, then the dual tetrahedron before separating into two pairs of α-particles again. Now note that the tetrahedron has three distinct pairs of opposing edges which can pull apart. Together, the different possibilities generate a two-dimensional space of deformations which we will refer to as the E-manifold. It is an extension of the local two-dimensional E-vibration of the tetrahedron to a global two-dimensional manifold of shapes which includes the important tetrahedron, flat square and bent rhomb configurations.

The E-manifold is modelled as the 6-punctured sphere with negative constant curvature. The position on the punctured sphere (x, y, z) corresponds to the position of one of the α-particles. The other three then lie at $(x, -y, -z), (-x, y, -z)$ and $(-x, -y, z)$. This fixes the standard orientation of the configurations. For instance, the point $(x, y, z) = (1, 1, 1)$ corresponds to a tetrahedron, while the point $(x, y, z) = (1, 1, 0)$ represents a flat square.
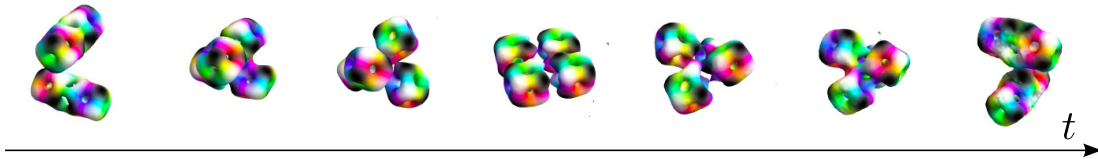
Figure 4.3: A numerically generated scattering path which links asymptotic configurations to the tetrahedron, the flat square and the dual tetrahedron. Time evolution is read left to right.

Since knowing one particle's position automatically fixes the other three, one can focus on a quarter of the sphere. Using hyperbolic geometry this quarter sphere is projected onto a portion of the complex plane. This mapping is displayed in Figure 4.4, where the positions of the geometric shapes, as well as the dynamical path from Figure 4.3, are also plotted. $\zeta = \eta + i\epsilon$ are coordinates on the complex plane.

The EM transition rates depend on the wavefunction and the multipole moments of the charge density, $\mathcal{Q}_{lm}$. Hence we must write these in terms of η and ϵ. As explained in Section 2.2, we can write $\mathcal{Q}_{lm}$ in terms of the positions of the particles, so we must find the mapping between the particle positions and the complex variables. We do this now. Given a point ζ on the complex plane, the position on a unit sphere is given by

$$(X, Y, Z) = \frac{1}{1 + |H(\zeta)|^2} \left(2\operatorname{Re}(H(\zeta)), 2\operatorname{Im}(H(\zeta)), 1 - |H(\zeta)|^2 \right) , \tag{4.26}$$

56
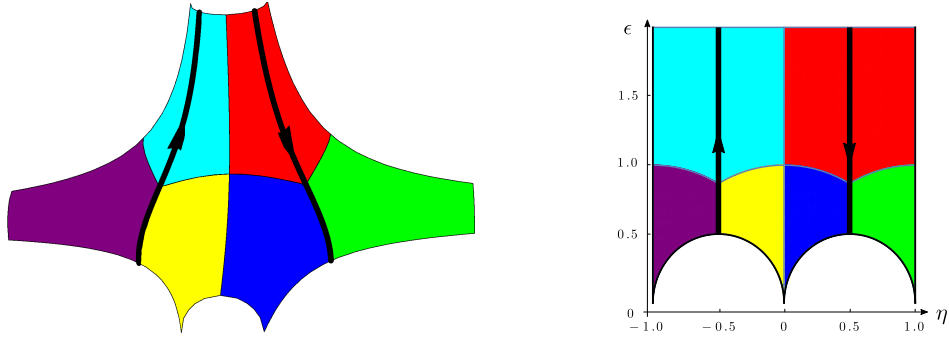
Figure 4.4: The relation between a quarter of the six-punctured sphere (left) and a portion of the complex plane (right). Tetrahedral configurations are at the points where three coloured regions meet while the square configurations are at points where four coloured regions meet. The scattering mode from Fig. 4.3 is represented by the thick black lines.

where

$$H(\zeta) = \left(\frac{\Theta_3 \left(\pi/4, \exp\left(i\pi\zeta\right) \right)}{\exp\left(\pi i(1+\zeta)/4 \right) \Theta_3 \left(\pi(1+2\zeta)/4, \exp(i\pi\zeta) \right)} \right)^2, \tag{4.27}$$

and Θ_3 is a Jacobi theta function. This is the unique metric-preserving map, up to Möbius transformations on $\mathbb{C}$. Having found the positions on a unit sphere, these should now be projected onto a sphere with punctures. We have some choice in this map but are constrained physically. We know the moments of inertia of the tetrahedron and square within the Skyrme model [25]. Additionally, once the configuration breaks into two clusters (as in the far left and far right of Figure 4.3) one of the moments must become constant and the other two grow quadratically with distance. The following projection satisfies all the aforementioned conditions

$$\mathbf{x}_1 = \frac{\kappa}{\sqrt{1 - (\max(X, Y, Z))^2}} (X, Y, Z) . \tag{4.28}$$

The constant κ gives the scale of the configuration. As an example, to calculate the positions of the α-particles at $\zeta = 0 + i$, we first calculate $H(i) = 1 + \sqrt{2}$, giving a unit sphere coordinate $(2^{-1/2}, 0, -2^{-1/2})$. We then map this to the position $\mathbf{x}_1 = \kappa(1, 0, -1)$. This is the position of one of the particles; the other three lie at $\boldsymbol{x}_2 = \kappa(1, 0, 1), \boldsymbol{x}_3 = \kappa(-1, 0, -1)$ and $\boldsymbol{x}_4 = \kappa(-1, 0, 1)$. Hence the point $\zeta = i$ corresponds to a flat square, lying in the x-z plane. We use these values of $\mathbf{x}_i$ to calculate $\mathcal{Q}_{lm}(\zeta)$ using equation (4.16). The scale parameter κ is later fixed, to match the $B(E3; 3_1^- \rightarrow 0_1^+)$ transition rate.

To find quantum states we must first calculate vibrational wavefunctions on the complex plane. These satisfy a Schrödinger equation which in turn depends on a metric and potential on the E-manifold of configurations. These were fixed in [7] and the Schrödinger equation takes the form

$$-\frac{\hbar^2}{2}\epsilon^2 \left(\frac{\partial^2}{\partial \eta^2} + \frac{\partial^2}{\partial \epsilon^2} \right) \psi + \epsilon^2 \left(\frac{1}{2}\omega^2 \left(\eta - \frac{1}{2} \right)^2 + \mu^2 \right) \psi = E_{\text{vib}} \psi , \tag{4.29}$$

J^P	Wavefunction	E (MeV)	E_{exp} (MeV)
0_1^+	$\psi_{T0}^+ \lvert 0,0 \rangle$	0	0
0_2^+	$\psi_{T2}^+ \lvert 0,0 \rangle$	6.1	6.0
2_1^+	$\frac{1}{\sqrt{8}}(u_1^+ - v_1^+)(\lvert 2,2\rangle + \lvert 2,-2\rangle) - \frac{\sqrt{3}}{2}(u_1^+ + v_1^+)\lvert 2,0\rangle$	6.7	6.9
3_1^-	$\psi_{S0}^- \frac{1}{\sqrt{2}}(\lvert 3,2\rangle - \lvert 3,-2\rangle)$	6.5	6.1
4_1^+	$\sqrt{\frac{5}{24}}\psi_{T0}^+\left(\lvert 4,4\rangle + \sqrt{\frac{14}{5}}\lvert 4,0\rangle + \lvert 4,-4\rangle\right)$	10.4	10.4
4_2^+	$\sqrt{\frac{7}{32}}(u_1^+ + v_1^+)(\lvert 4,4\rangle + \lvert 4,-4\rangle)$ $-\frac{1}{\sqrt{8}}(u_1^+ - v_1^+)(\lvert 4,2\rangle + \lvert 4,-2\rangle) - \frac{\sqrt{5}}{4}(u_1^+ + v_1^+)\lvert 4,0\rangle$	12.6	11.1

Table 4.3: The wavefunctions, in terms of vibrational wavefunctions and spin states, for each of the states considered in this chapter. Each model state is identified with an experimental state, whose energy is also tabulated. We suppress the J_3 label for ease of reading.

where ω and μ are phenomenological parameters. The potential was chosen so that the tetrahedra have minimal energy, the squares have higher energy (by around 6 MeV) and the asymptotic configurations have even higher energy. The expression (4.29) is only valid in the red region of the complex plane (for the colouring, see Figure 4.4). The wavefunctions were calculated in [7] and classified further in [50]. Four of them will be relevant for our calculation - labelled $\psi_{T0}^+, \psi_{T1}^+, \psi_{S0}^-$ and (u_1^+, v_1^+). These are combined with rigid-body wavefunctions to create physical states. The allowed states, relevant for our calculation, are listed in Table 4.3. We plot the shape probability density function on the complex plane for each of the wavefunctions in Figure 4.5. We sometimes say that a state is "tetrahedral" or "square-like". This means that the corresponding probability density is concentrated at those configurations. The states $0_1^+, 3_1^-, 4_1^+$ are all tetrahedral and form an approximate rotational band. The states 2_1^+ and 4_1^+ are both strongly concentrated at the squares and should be thought of as rotational excitations of a square configuration. The 0_2^+ state is concentrated at both the squares and tetrahedra and is interpreted as an admixture of both these geometries.

To help analyse and compare results, it is helpful to introduce the idealised rigid body as a benchmark model. Here, the nucleus is described as four α-particles that form a rigid geometric shape which is allowed to rotate as a whole. This rotational motion is quantised and leads to rotational bands. Different shapes can lead to different rotational bands. For Oxygen-16, the $0_1^+, 3_1^-, 4_1^+$ states are understood as the rotational band of a tetrahedron while the $0_2^+, 2_1^+, 4_2^+$ states arise as the rotational band of a square (or possibly a chain [49], though this idea was recently dismissed experimentally [51]). The most important parameter in this model is the ratio of the separation between the particles which form the tetrahedron r_t and the separation between the particles which form the square r_s. We take

$$\frac{r_s}{r_t} = 1.5\,, \tag{4.30}$$

0_1^+ and 4_1^+ $\qquad\qquad$ 0_2^+ $\qquad\qquad$ 3_1^- $\qquad\qquad$ 2_1^+ and 4_2^+
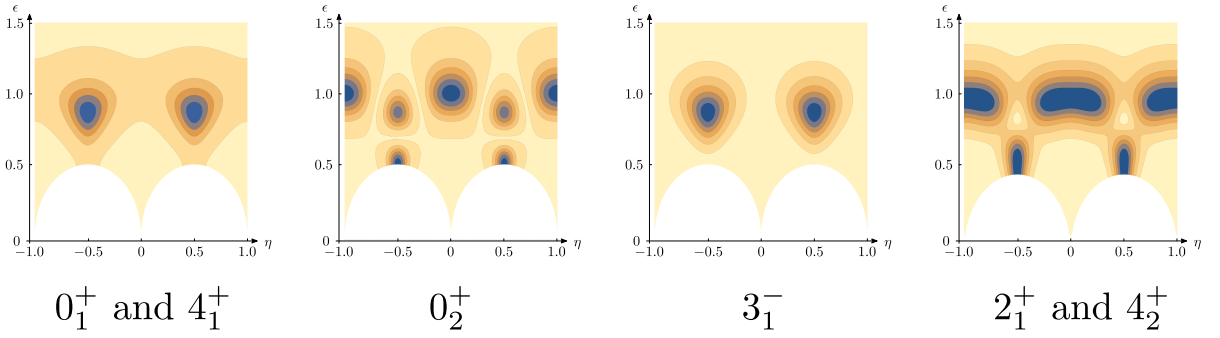
Figure 4.5: Shape probability densities for each wavefunction, plotted on a region of the complex ζ-plane. Blue regions correspond to large densities while pale regions have small densities.

and then fix r_t to match the $B(E3; 3_1^- \to 0_1^+)$ transition. This is likely not a realistic model but displays some important features that highlight the physics at play.

4.4.1 Results

The electromagnetic transition rates for our model, the rigid body model, the ab initio calculation [52] and the ACM [53] are displayed in Table 4.4. They should be compared to the experimental data, which is also tabulated.

The transition rates along the lowest-lying band are in good agreement with experimental data in our model. These states are constructed from ψ_{T0}^+, which is concentrated at the tetrahedron. Hence, this result supports the idea that these states are tetrahedral. The value for the $E6$ transition is close to the value from the ACM. This is to be expected, as the states have similar descriptions in both models.

The rigid body model highlights some important physics, though is an extreme approximation as can be seen from the enormous $E6$ transition. Since the square is more spread out than the tetrahedron, the square-like states (such as 0_2^+, 2_1^+ and 4_2^+) have large transition rates between them. Similarly, the states in our vibrational model which contain significant square contributions lead to larger transition rates. For instance $B(E2; 2_1^+ \to 0_2^+) > B(E2; 2_1^+ \to 0_1^+)$, since 0_2^+ is physically a mixture of the two shapes while 0_1^+ contains little square contribution. This ordering is seen experimentally but the magnitudes of the transition rates are wrong in our model. For instance, the $B(E2, 2_1^+ \to 0_2^+)$ is too small.

This shortcoming may be due to the approximations made in constructing the wavefunctions. We neglect the effect that a changing shape has on the structure of the wavefunction. This is because we take a constant moment of inertia tensor over the space of configurations. Hence, the 2_1^+ wavefunction doesn't account for the fact that the square is much flatter than the tetrahedron. If we did account for this, the wavefunction would be more concentrated at the square and the transition rate would be enhanced. Note that the Carbon-12 calculation

$B\left(El, i \to f\right)$	our model	rigid body model	"rescaled" ab initio [52]	ACM [45]	experiment $\left[e^2\text{fm}^{2l}\right]$ [47]
$B\left(E3, 3_1^- \to 0_1^+\right)$	205	205		215	205 ± 11
$B\left(E4, 4_1^+ \to 0_1^+\right)$	320	633		425	378 ± 133
$B\left(E6, 6_1^+ \to 0_1^+\right)$	11263	23764		9626	
$B\left(E1, 2_1^+ \to 3_1^-\right)$	0	0			$< 1.6 \times 10^{-5}$
$B\left(E1, 4_1^+ \to 3_1^-\right)$	0	0			$< 1.2 \times 10^{-5}$
$B\left(E1, 4_2^+ \to 3_1^-\right)$	0	0			$(2.4 \pm 1) \times 10^{-5}$
$B\left(E2, 2_1^+ \to 0_1^+\right)$	16	0	6.2 ± 1.6	26	7.4 ± 0.2
$B\left(E2, 2_1^+ \to 0_2^+\right)$	22	70	46 ± 8	6	65 ± 7
$B\left(E2, 2_1^- \to 3_1^-\right)$	–	0		10	13.4 ± 3.8
$B\left(E2, 4_1^+ \to 2_1^+\right)$	13	0		0	146 ± 17
$B\left(E2, 4_2^+ \to 2_1^+\right)$	7	100		36	2.4 ± 0.7
$B\left(E4, 4_1^+ \to 0_2^+\right)$	24	0			
$B\left(E4, 4_2^+ \to 0_1^+\right)$	592	0			
$B\left(E4, 4_2^+ \to 0_2^+\right)$	1632	8801			

Table 4.4: EM transition rates $B\left(El, i \to f\right)$ for Oxygen-16. We tabulate the results for the model described in this section, the ab initio calculation and the algebraic cluster model, as well as the available experimental data. All values are in units of $e^2\text{fm}^{2l}$.

does account for this effect. To do the same calculation for the Oxygen-16 case, it would be necessary to solve the full Schrödinger equation on the two-dimensional six-punctured sphere or develop a quantum graph model. This partially explains the discrepancy between the vibrational and rigid body models. The problem is even more pronounced in the $B(E2; 4_2^+ \to 2_1^+)$ transition rate. Naively, one would expect this to be large: physically, both states are square-like. As we can see from the rigid body model, this should lead to a large transition rate. But the wavefunctions are both diminished due to our approximation.

Although the rigid body model can generate large transition rates (which are seen in nature), it also predicts many erroneous zero results. This is easily understood: states can only decay along rotational bands. This is not seen in the experimental data and suggests the model is too constrained. Similarly, the ACM predicts many small or zero results which are not in agreement with data. The vibrational model allows for greater overlap between wavefunctions and hence there are no zero results for any transitions, except the $E1$ transitions. Unfortunately, the true amount of mixing is underestimated in all models.

There is one major discrepancy between all models and data. The $B(E2; 4_1^+ \to 2_1^+)$ transition has a value of $(146 \pm 17)e^2\text{fm}^4$, while the rigid body, ACM and vibrational models give predictions of $0, 0$ and 13 respectively: at best an order of 10 out. Such a large transition rate is very rare, so to find any possible explanation is worthwhile. One idea is that the 4_1^+ state has been historically mischaracterised as a tetrahedral state. Suppose instead that the low lying $0_2^+, 2_1^+, 4_1^+$ band is a rotational band, of either the square or chain configurations.

Then there is the following relationship for transition rates between states on the band

$$\frac{B(E2; 4_1^+ \to 2_1^+)}{B(E2; 2_1^+ \to 0_2^+)} = \frac{10}{7} \approx 1.43\,. \tag{4.31}$$

In reality, the experimental ratio is

$$\frac{146 \pm 17}{65 \pm 7} = 2.25 \pm 0.5\,. \tag{4.32}$$

This large ratio highlights the difficulty in describing the $B(E2; 4_1^+ \to 2_1^+)$ transition. The rigid body model, which should exaggerate this type of transition, still underestimates it. If one were to re-characterise the 4_1^+ state as a rotational excitation of the square, the 4_2^+ would then be interpreted as a tetrahedral state. The energy difference between the 4_1^+ and 4_2^+ states is only 0.74 MeV, so their relabeling is reasonable on energetic grounds. As can be seen in Table 4.4, the 4_2^+ state can still have a large E4 transition in the vibrational model, so this new interpretation may not spoil the positive results along the ground state band. To investigate further, one should improve the vibrational model to allow for a changing moment of inertia tensor, as described above. This should give more accurate results and will avoid underestimation. Secondly, it may be worthwhile to redo the transition rate experiments. These were last undertaken in the 1970s and early 1980s. Modern techniques would allow us to fill out Table 4.4 more fully. We are suggesting the spin 4 states may be mischaracterised, so having more information about the decay from the spin 4 states would be particularly useful.

4.5 Summary and further work

Electromagnetic transition rates offer a wealth of information about the intrinsic structure of atomic nuclei. EM transitions help us to differentiate between the vast number of nuclear models on offer: shell model approaches, collective models, and the ACM to name a few. In this chapter we developed a general formalism for computing EM transition rates within the framework of rotational-vibrational nuclear models.

Within this formalism, we calculated EM transition rates for two models of Carbon-12 and Oxygen-16 inspired by nuclear dynamics in the Skyrme model. We found reasonable agreement with experimental data and highlighted important differences between our model's predictions and those of other models.

For Carbon-12 both our model and other models reproduce the existing data well. To differentiate the models more data is needed. We hope that this study provides fresh motivation to measure more EM transition rates for Carbon-12. The results for Oxygen-16 are less promising, for all models. We suggested that some discrepancies between experimental data

and our model could be traced to our approximations. These may be improved by including a varying moment of inertia in our Schrödinger equation, or by developing a quantum graph model for the nucleus. We will explore this possibility in Chapter 5. No model comes close to full agreement with experimental data so there is still work to be done, even for these abundant nuclei. Further experimental data will help us to uncover their detailed structure.

We have focused on E transitions but M transitions are also seen experimentally. While E transitions depend on the charge density of the nucleus, the M transitions depend on the current density. These have been studied for Helium-3 and Hydrogen-3 within the Skyrme model [54] but are not well understood in general.

Chapter 5

Quantum graphs and Oxygen-16

In the previous chapter we introduced the E-manifold model for Oxygen-16 originally proposed by Halcrow, King and Manton [7]. In this chapter we explore a simple quantum graph model for Oxygen-16 inspired by their work. The original model is an α-particle model in which the local E-vibration of the tetrahedron is extended to a global two-dimensional manifold of shapes. We construct a graph Γ which is designed to capture the most important shapes on the E-manifold, namely the paths connecting the tetrahedron to its dual via a flat square. In this simple toy model, we explore some of the subtleties involved in picking a body-fixed frame convention for each of the shapes on Γ. In the language of principal bundles, this means picking a section of an SO(3)-bundle over Γ. We find that the choice made by the authors of [7] does not lead to a globally well-defined section. This subtlety was overlooked in more recent extensions to the model [50], and we suggest that some states have been missed as a consequence.

5.1   Quantum graph model for E-manifold

Recall the E-manifold model for Oxygen-16, outlined in Chapter 4. The model is based on the quantized dynamics of four (point) α-particles which are restricted to take shapes in the so-called E-manifold. We are interested in a subset of these shapes, with the subset taking the form of a three-edged graph which can be embedded in the two-dimensional E-manifold. We consider shapes which interpolate between a tetrahedron and its dual via a flat square, inspired by the corresponding dynamical mode in the Skyrme model. The α-particles are indistinguishable, but we take them to be distinguishable (indistinguishability can always be imposed at the end by only considering quantum states which transform trivially under permutation of the particles). The relevant graph of shapes, Γ, is illustrated in Figure 5.1. Vertex A corresponds to a tetrahedron and vertex B its dual. The midpoints of each edge represent square configurations. This is illustrated in Figures 5.2 and 5.3. We emphasise
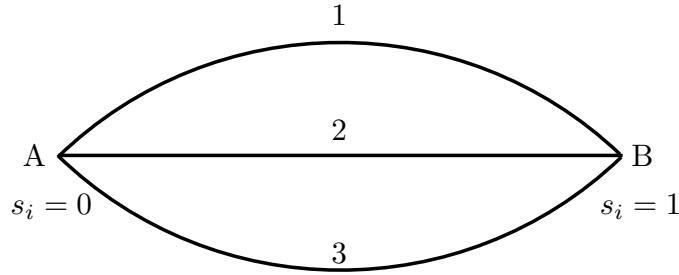
Figure 5.1: Shape space Γ.

that the square configurations on distinct edges are not related to each other by rotations since the particles are distinguishable.

Including all possible orientations, the resulting configuration space $\mathcal{C}$ has the structure of an $SO(3)$-bundle, with the projection

$$\pi : \mathcal{C} \to \Gamma$$

sending an oriented configuration to its (unoriented) shape $s \in \Gamma$. We call Γ shape space.

Picking coordinates on $\mathcal{C}$ amounts to specifying a (reference) orientation, or equivalently a body-fixed frame, for each point on Γ. This is just the same thing as specifying a section of the SO(3)-bundle $\mathcal{C}$. Following Halcrow, King and Manton, we choose these reference orientations in a way which preserves a fixed D_2-symmetry. This choice is illustrated in Figures 5.2 and 5.3.

Note, however, that this choice isn't well-defined globally on Γ: starting at A, the orientation we arrive at when we get to B *depends on* which edge we traverse. This is clear from considering the rightmost configurations in Figure 5.2. In other words, this body-fixed frame convention doesn't amount to a global section of the bundle $\mathcal{C}$. This subtlety was not mentioned in the original analysis presented in [7] as the authors worked with indistinguishable particles from the start. We will see, however, that it matters once we introduce additional vibrations which take the shape away from Γ.

We can still work with this choice even though it isn't globally well-defined: we simply choose to work on two separate patches, with one excluding vertex B and the other excluding vertex A. Within each patch, we can write down sensible coordinates by following the body-fixed frame convention just described. Appropriate transition functions relate the coordinates where these patches overlap. For our choice of local sections, illustrated in Figures 5.2 and 5.3, these transition functions correspond to rotations by π about the $1, 2, 3$-axes on edges $1, 2, 3$ respectively.

The main motivation for the D_2-symmetric body-fixed frame convention of Halcrow, King
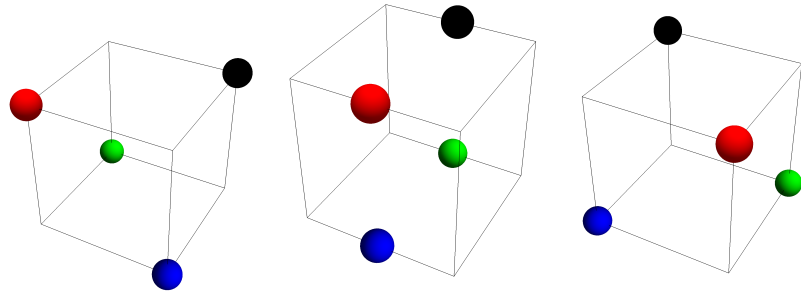
(a) edge 1
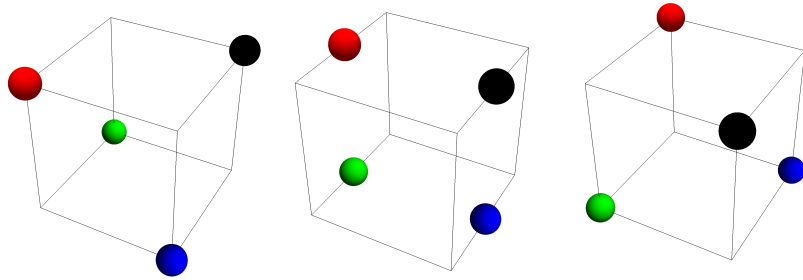
(b) edge 2
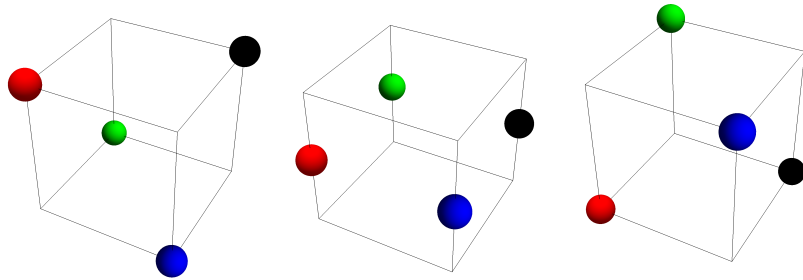
(c) edge 3

Figure 5.2: Reference orientations in patch excluding B (left to right corresponds to moving from vertex A to vertex B).
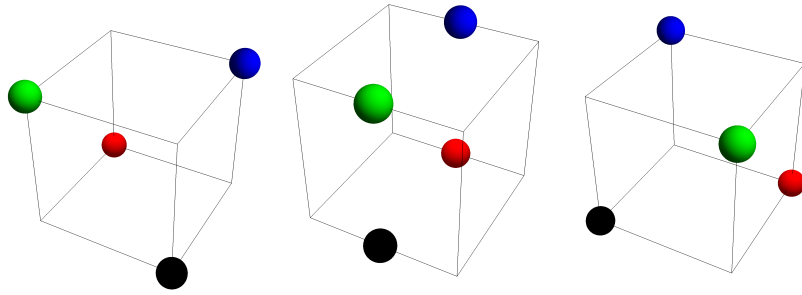
(a) edge 1
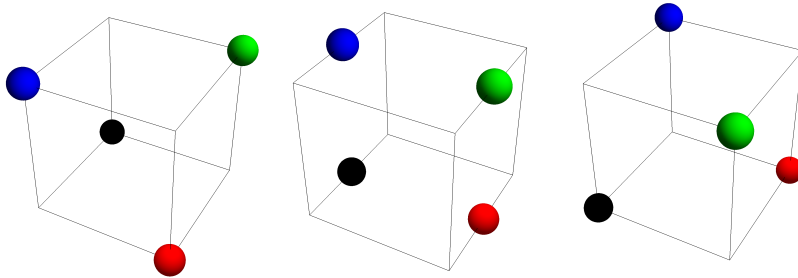
(b) edge 2
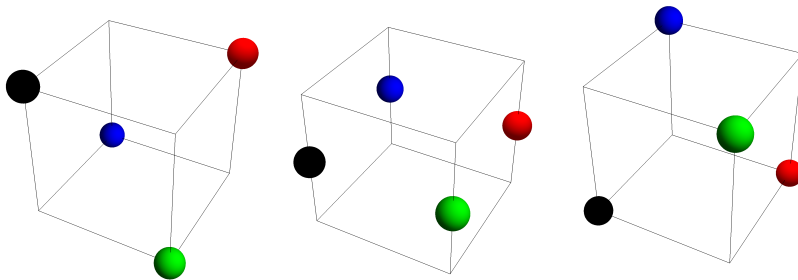
(c) edge 3

Figure 5.3: Reference orientations in patch excluding A (left to right corresponds to moving from vertex A to vertex B).

and Manton is that it guarantees that there is no rotation-vibration coupling: in this gauge, vibrations are orthogonal to rotations (i.e. the fibres). To simplify the model even further we will assume that the dynamics are given by free motion on the graph edges together with spherical top motion in the orientational coordinates:

$$\mathcal{H} = -\frac{1}{2}\frac{d^2}{ds^2} + \frac{1}{2\mathcal{I}}\mathbf{L}^2.$$
(5.1)

Here s is a coordinate along the edge with range $s \in (0,1)$ and $\mathcal{I}$ is a constant moment of inertia. Energy eigenfunctions (in a particular patch) therefore take the form

$$(a \exp(iks) + b \exp(ik(1-s))) |JJ_3L_3\rangle$$

on each edge. The corresponding energy eigenvalue is

$$E = \frac{k^2}{2} + \frac{J(J+1)}{2\mathcal{I}}$$
(5.2)

which depends only on the angular momentum J and the edge momentum k.

We impose quantum graph boundary conditions at the vertices of the graph, which implies linear constraints on the various coefficients like a and b (as outlined in the introduction to QGT in Chapter 1). Also, we require compatibility of the wavefunctions in different patches in the usual sense, with the wavefunctions agreeing on the overlaps after application of the relevant transition function.

The resulting states can be classified by parity and by S_4 symmetry (corresponding to permutations of the α-particle identities). An example of this type of calculation is presented in Section 5.2. The resulting spectrum is shown in Table 5.1. For Oxygen-16 states, we want the *trivial* irrep A_1 of S_4 so we see that we obtain 0^+, 2^+ and 3^- states for the range of J and k considered in the table. The states transforming in the other irreps of S_4 will be of use when we include the A and F vibrations later on.

5.2   Example calculation

Suppose we are looking for a spin 1 state. Parametrise each edge by s which ranges from $s = 0$ (vertex A) to $s = 1$ (vertex B). On the patch which excludes vertex B, suppose we seek a state with wavefunction of the form

$$(a_i \exp(iks) + b_i \exp(ik(1-s))) |1, 0\rangle$$

k	J	S_4^P
0	0	A_1^+
	2	E^+
	3	A_2^+
	4	$A_1^+ \oplus E^+$
ζ	1	F_2^-
	2	F_1^-
	3	$F_1^- \oplus F_2^-$
	4	$F_1^- \oplus F_2^-$
$\pi - \zeta$	1	F_1^+
	2	F_2^+
	3	$F_1^+ \oplus F_2^+$
	4	$F_1^+ \oplus F_2^+$
π	0	$A_2^- \oplus E^+$
	1	F_2^-
	2	$E^- \oplus E^+ \oplus A_1^+ \oplus A_2^+ \oplus F_1^-$
	3	$A_1^- \oplus E^+ \oplus F_1^- \oplus F_2^-$
	4	$E^+ \oplus E^- \oplus E^+ \oplus A_1^+ \oplus A_2^+ \oplus F_1^- \oplus F_2^-$
$\pi + \zeta$	1	F_1^+
	2	F_2^+
	3	$F_1^+ \oplus F_2^+$
	4	$F_1^+ \oplus F_2^+$
$2\pi - \zeta$	1	F_2^-
	2	F_1^-
	3	$F_1^- \oplus F_2^-$
	4	$F_1^- \oplus F_2^-$
2π	0	$A_1^+ \oplus E^-$
	1	F_1^+
	2	$E^+ \oplus A_1^- \oplus A_2^- \oplus E^- \oplus F_2^+$
	3	$A_2^+ \oplus E^- \oplus F_1^+ \oplus F_2^+$
	4	$A_1^+ \oplus E^- \oplus E^+ \oplus A_1^- \oplus A_2^- \oplus E^- \oplus F_1^+ \oplus F_2^+$

Table 5.1: States up to angular momentum $J = 4$ and edge momentum $k = 2\pi$. The final column S_4^P gives the parity P of the states together with the S_4 irrep corresponding to permutations of the four α-particles.

on each edge i. (For clarity we have suppressed the space-fixed angular momentum J_3 which can freely take any of the values $1, 0, -1$). The transition functions act as

$$\exp\left(-i\pi L_1\right),$$

$$\exp\left(-i\pi L_2\right),$$

and

$$\exp\left(-i\pi L_3\right)$$

on edge 1, 2 and 3 respectively. The matrix representations for these operators are

$$\begin{pmatrix} -1 & 0 & 0 \\ 0 & -1 & 0 \\ 0 & 0 & 1 \end{pmatrix},$$

$$\begin{pmatrix} 1 & 0 & 0 \\ 0 & -1 & 0 \\ 0 & 0 & -1 \end{pmatrix}$$

and

$$\begin{pmatrix} -1 & 0 & 0 \\ 0 & 1 & 0 \\ 0 & 0 & -1 \end{pmatrix}$$

with respect to the basis $\left\{ \frac{1}{\sqrt{2}}\left(|1,1\rangle + |1,-1\rangle\right), |1,0\rangle, \frac{1}{\sqrt{2}}\left(|1,1\rangle - |1,-1\rangle\right)\right\}$. Therefore our wavefunction

$$\left(a_i \exp\left(iks\right) + b_i \exp\left(ik\left(1-s\right)\right)\right)|1,0\rangle$$

picks up a minus sign under the action of the transition functions on edges 1 and 2 but is invariant on edge 3. It follows that in the other patch, which excludes vertex A, the wavefunction must have the form

$$\left(-a_1 \exp\left(iks\right) - b_1 \exp\left(ik\left(1-s\right)\right)\right)|1,0\rangle$$

$$\left(-a_2 \exp\left(iks\right) - b_2 \exp\left(ik\left(1-s\right)\right)\right)|1,0\rangle$$

$$\left(a_3 \exp\left(iks\right) + b_3 \exp\left(ik\left(1-s\right)\right)\right)|1,0\rangle$$

on edges 1, 2 and 3 respectively. The vertex conditions (see Chapter 1) at B imply the linear constraints

$$-a_1 \exp\left(ik\right) - b_1 = -a_2 \exp\left(ik\right) - b_2 = a_3 \exp\left(ik\right) + b_3 \qquad (5.3)$$

and

$$-a_1 \exp(ik) + b_1 - a_2 \exp(ik) + b_2 + a_3 \exp(ik) - b_3 = 0 \tag{5.4}$$

which are to be combined with the linear constraints at vertex A, which are

$$a_1 + b_1 \exp(ik) = a_2 + b_2 \exp(ik) = a_3 + b_3 \exp(ik) \tag{5.5}$$

and

$$a_1 - b_1 \exp(ik) + a_2 - b_2 \exp(ik) + a_3 - b_3 \exp(ik) = 0. \tag{5.6}$$

Altogether,

$$\begin{pmatrix} -e^{ik} & -e^{ik} & e^{ik} & 1 & 1 & -1 \\ 1 & 1 & 1 & -e^{ik} & -e^{ik} & -e^{ik} \\ 1 & -1 & 0 & e^{ik} & -e^{ik} & 0 \\ 1 & 0 & -1 & e^{ik} & 0 & -e^{ik} \\ e^{ik} & -e^{ik} & 0 & 1 & -1 & 0 \\ e^{ik} & 0 & e^{ik} & 1 & 0 & 1 \end{pmatrix} \begin{pmatrix} a_1 \\ a_2 \\ a_3 \\ b_1 \\ b_2 \\ b_3 \end{pmatrix} = \begin{pmatrix} 0 \\ 0 \\ 0 \\ 0 \\ 0 \\ 0 \end{pmatrix}. \tag{5.7}$$

These are very similar conditions to those considered for the three-edged graph in Chapter 1 - the only difference is the appearance of extra minus signs coming from the action of the transition functions. The determinant of the matrix on the LHS is simply

$$\det = -9 \left(\exp(2ik) - 1 \right) \left(\exp(2ik) + \frac{7 + 4i\sqrt{2}}{9} \right) \left(\exp(2ik) + \frac{7 - 4i\sqrt{2}}{9} \right) \tag{5.8}$$

which is zero when $\frac{k}{\pi} \in \mathbb{Z}^+$ or when k differs from an integer multiple of π by ζ where

$$\zeta = \tan^{-1}\left(2\sqrt{2}\right). \tag{5.9}$$

Each of these values of the edge momentum k leads to a spin 1 state. These are included in Table 1 along with their transformation properties under the action of S_4 permutations and parity.

5.3 A and F

In addition to $\mathcal{C}$, we may include other vibrations which take the shape away from those on the graph Γ. In [50] the authors considered additional vibrations A and F corresponding to vibrations of the tetrahedron which transform as A and F irreps under the tetrahedral symmetry group. The A vibration corresponds to a simple global rescaling. The F vibration corresponds to a three-dimensional space of deformations and a basis $\{v_1, v_2, v_3\}$ for this
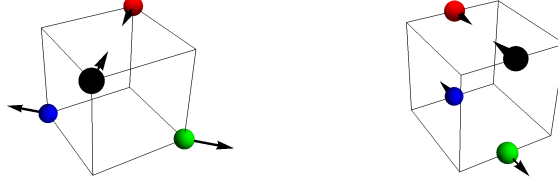
Figure 5.4: One direction in the three-dimensional F-vibration space: red and black move together while blue and green move apart.

space can be defined as follows:

v_1: particles 1 and 4 move together while particles 2 and 3 move apart.

v_2: particles 2 and 4 move together while particles 1 and 3 move apart.

v_3: particles 3 and 4 move together while particles 1 and 2 move apart.

One such vector is illustrated in Figure 5.4, with the different colours representing the different particle labels.

Suppose we treat A and F in a harmonic approximation, giving the enlarged configuration space

$$\mathcal{C} \times \mathbb{R} \times \mathbb{R}^3.$$

We want to construct states on this enlarged space. We can treat the three factors independently: the total wavefunction belongs to the tensor product space $V_{\mathcal{C}} \otimes V_A \otimes V_F$ where $V_{\mathcal{C}}$, V_A and V_F denote the spaces of wavefunctions on $\mathcal{C}$, $\mathbb{R}$ and $\mathbb{R}^3$ respectively. For Oxygen-16, we seek singlets under the combined action of S_4 on $V_{\mathcal{C}} \otimes V_A \otimes V_F$. We have already classified wavefunctions on $\mathcal{C}$ by their S_4 representations.

Consider states with n_F F-phonons and n_A A-phonons. Note that particle permutations in S_4 act on the $\mathbb{R}^3$ as F_2 and so harmonic oscillator states in V_F with n_F phonons transform as the symmetric tensor product $F_2^{\otimes_S n_F}$ (since vibrational phonons behave as identical bosons). Similarly, S_4 acts on the $\mathbb{R}$ as the trivial irrep A_1 and so harmonic oscillator states in V_A with n_A phonons transform as A_1. To give a singlet overall, we need to combine these with a wavefunction on $\mathcal{C}$ which transforms as R such that the tensor product $R \otimes F_2^{\otimes_S n_F} \otimes A_1$ contains a singlet.

For example, suppose we seek a state with one F-phonon and one A-phonon. Then we require a wavefunction on $\mathcal{C}$ which transforms as F_2 under S_4. Looking at Table 5.1, we find that we can make $1^-, 3^-, 2^+, 3^+, 2^-, 3^-$ states (for angular momentum $J \leq 3$ and ordered by ascending edge momentum k).

5.4 Discussion

It would be possible to derive a full energy spectrum from this model and fit parameters such as the moment of inertia $\mathcal{I}$ and the vibrational frequencies by comparison to experimental data for Oxygen-16. However, our model is very crude (including assumptions such as free motion along the edges and a constant spherical top moment of inertia) and so further refinements would be required to give an accurate model. The main purpose of this chapter was to illustrate some subtleties present in the E-manifold model for Oxygen-16 which have so far gone unnoticed. In particular, we argued that the body-fixed frame convention for E-manifold shapes (here approximated by our three-edged graph Γ) used in previous work does not correspond to a genuine global section of the total configuration space. The E-manifold (and the extension by small vibrations such as A and F) should be thought of as the *base space* of an $\mathrm{SO}\,(3)$-bundle. One consequence is that the total wavefunction should not be thought of as simply a product of a shape wavefunction and a rotational wavefunction (i.e. a product of a function on the base space and a function on the fibre). Rather, the shape wavefunction should be thought of as a section of a bundle over shape space satisfying appropriate compatibility conditions involving bundle transition functions. As a result, in [50] states have been missed including all those states in Table 5.1 which transform in the F_1 or F_2 irreps of S_4. We hope that our approach, making the bundle structure of the configuration space explicit, clarifies these subtleties and that these ideas will be of use in future rovibrational nuclear models.

Chapter 6

Rovibrational states of protonated methane

This chapter is based on the single-author paper [55].

6.1 Introduction

In this chapter we turn to molecular physics, using QGT to model the low-energy dynamics of the protonated methane molecular ion (CH_5^+). CH_5^+ was discovered in 1950 by mass spectrometry [56]. There is great interest in the rovibrational states of CH_5^+ [57] as it has astrochemical significance, appearing as an intermediate in reactions which produce polyatomic molecules in interstellar clouds [58]. The associated Born-Oppenheimer potential energy surface has a global minimum with C_s symmetry [59], usually thought of as a H_2 unit sitting on top of a CH_3^+ tripod. The next highest saddle points have C_s and C_{2v} symmetry, with energies larger than the minimum by roughly $40cm^{-1}$ and $280cm^{-1}$ [60]. Thus the potential energy surface is extremely flat. In fact, it has been shown that even the quantum zero-point energies for the nuclear vibrations [61] are sufficiently large to completely overcome these energy barriers. This implies that, even in the quantum ground state, CH_5^+ does not have a single definite structure but moves between the various stationary points of the potential energy surface.

In the following sections, we outline and extend the quantum graph model for CH_5^+ which was first introduced in [5]. This model uses QGT to describe the low-energy dynamics of CH_5^+ in a similar spirit to the nuclear models of the previous chapters. The original calculations were restricted to $J = 0$ states as orientational degrees of freedom were neglected. We extend these calculations to the $J > 0$ sector, allowing us to explore fully rovibrational states in the quantum graph model for the first time.

High-resolution infrared (IR) spectra of CH_5^+ in the region relevant to the C-H stretching

band have been measured several times including in [62] and [63]. These spectra contain thousands of lines and are difficult to interpret as the traditional ideas in vibrational spectroscopy do not apply to this floppy molecular ion. Great progress was made in recent experimental work [63] in which samples were probed at temperatures as low as 10K and 4K. At these temperatures only the very lowest quantum states are occupied, and so it is possible to infer the energy differences between them through the method of combination differences (comparing two transitions which involve a single common state). Despite this recent success, the experimental data concerning the low-energy rovibrational states is too sparse to make a comparison with our model worthwhile, and so we will compare our model results to the sophisticated quantum-chemical calculations of [64] which found states up to spin $J = 3$. The drastic reduction in the number of degrees of freedom in our model compared to other approaches allows us to compute states which have been inaccessible to all previous calculations. We illustrate this by computing $J = 4$ rovibrational states for the first time.

6.2 Quantum graph model

In [5] it was proposed that the low-energy vibrational states of CH_5^+ can be understood using QGT. The authors computed the energies and symmetry properties of the vibrational states, comparing the results with more sophisticated quantum-chemical calculations. The agreement is remarkable given the simplicity of the quantum graph model, in which only two kinds of bending motion for CH_5^+ are considered (to be compared with seven-dimensional [64, 65] and even twelve-dimensional calculations [66]).

The 120-vertex metric graph Γ (see Figure 1), introduced in [5], is illustrated in Figures 6.1 and 6.2. Each point on the graph represents a possible molecular shape for CH_5^+, with the vertices corresponding to the 120 distinct versions of the equilibrium structure and the edges representing low-energy paths between them. The equilibrium structure (the minimum on the Born-Oppenheimer potential energy surface) of CH_5^+ has a C_s point-group symmetry and can be thought of as a H_2 unit sitting on top of a CH_3^+ tripod. Each version of the equilibrium structure is connected to three other versions, with two different kinds of paths occurring, indicated by the red and blue edges. Blue edges have length L_1 and red edges have length L_2. The blue edges correspond to internal rotation of the H_2 relative to the tripod (this motion takes the configuration through a C_s-symmetric saddle point). The red edges correspond to a flip motion which exchanges a pair of protons between the H_2 and CH_3^+ units (taking the configuration through a C_{2v}-symmetric saddle point). These paths are illustrated in Figure 6.2.

We assume that, even at low energies, the molecule can explore all of this graph by changing its shape. The molecule also has rotational degrees of freedom. So the space $\mathcal{C}$ of all possible configurations of the molecule can be thought of as an SO(3)-bundle with base
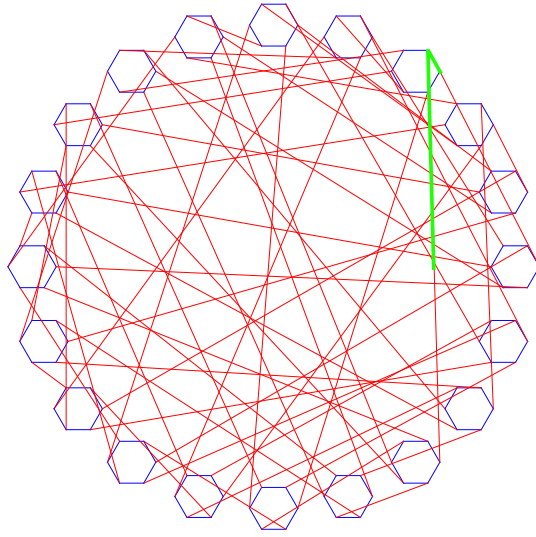
Figure 6.1: Quantum graph Γ. Figure courtesy of Csaba Fábri and Attila G. Császár.

space Γ. Our strategy is to map the (very complex) quantum dynamics of CH_5^+ onto the motion of a particle confined to $\mathcal{C}$.

6.2.1 Motion on $\mathcal{C}$ and symmetries

The motion of a particle confined to $\mathcal{C}$ is already a drastic simplification compared to the full quantum dynamics of CH_5^+. However, by exploiting symmetries, we can make the problem even simpler. The Molecular Symmetry (MS) group of CH_5^+ is S_5^*, generated by permutations of the 5 protons together with spatial inversion. Each permutation $\pi \in S_5^*$ acts on $\mathcal{C}$, taking configurations at a given point p on the graph Γ and mapping them to configurations at a new point $\pi(p)$ on the graph. In fact, by acting with permutation elements of S_5^* we can generate the entire graph from only two edges, or even one edge and one half-edge. An example of a choice is highlighted in green in Figure 6.1. We will refer to this green part of $\mathcal{C}$ as the *fundamental domain*, and the vertex where the two green edges meet as V. Note that S_5^* is a symmetry of $\mathcal{C}$ and so the quantum states can be classified by irreps of S_5^*. Working within a particular irrep, the wavefunctions on $\mathcal{C}$ must transform in a definite way under the action of S_5^* and this allows us to deduce the value of the wavefunction on all of $\mathcal{C}$ so long as we know the value of the wavefunction on the fundamental domain. So we only need to determine the wavefunction on the fundamental domain (once an irrep has been chosen), not on all of $\mathcal{C}$: the rest is determined by symmetry.

75
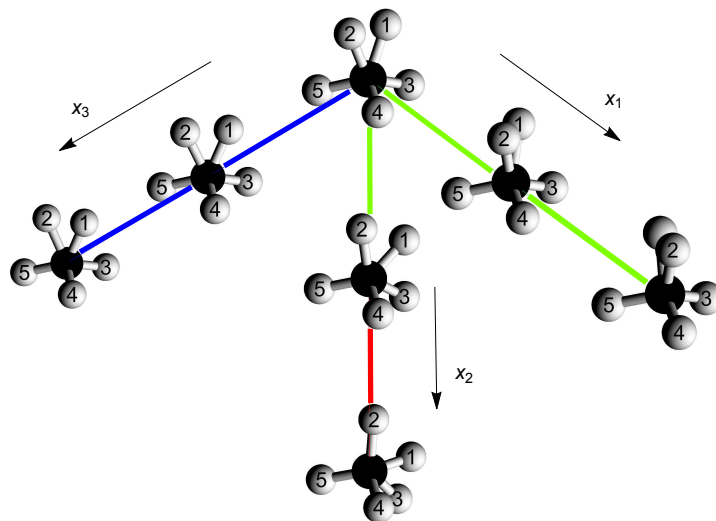
Figure 6.2: Low-energy paths between distinct versions of the equilibrium structure.

6.2.2 Defining the problem on the fundamental domain

We need to write down an appropriate Hamiltonian on each edge. This should involve a kinetic energy contribution and a potential. To make the model as simple as possible we will set the potential to zero. In general, one expects the kinetic energy to involve contributions from both vibrational motion (motion along the graph) and rotational motion as well as rovibrational cross-terms, as we have seen in the previous chapters. But there is quite a lot of freedom in which coordinates we choose and so we can exploit this freedom to eliminate the cross-terms: essentially, we want vibrational motions to be orthogonal to rotational motions.

Start by picking a coordinate x' along the edge of the graph. We will use Euler angles for the orientational degrees of freedom, so altogether we have coordinates (x', θ, ϕ, ψ). The Euler angles (θ, ϕ, ψ) tell us (in the usual way) the rotation relating the body-fixed frame of the molecule to a space-fixed frame. But we must still specify a choice of body-fixed frame for each shape along the edge. In the language of Chapter 2, we need to make a gauge choice. It is clear that we can make this choice, as we go along the edge, in such a way that makes the gauge field $\mathbf{A}$ vanish on this edge and so eliminates any cross-terms. So we may assume that in the coordinates (x', θ, ϕ, ψ) the kinetic energy operator has only a purely vibrational contribution and a purely rotational contribution. Now we can further transform the coordinate $x' \to x(x')$ to make the vibrational kinetic operator simply $-\frac{1}{2}\frac{d^2}{dx^2}$ (this relies on the fact that the vibration is only one-dimensional). As for the rotational kinetic energy, we assume that the moments of inertia do not vary much and so we use the approximate kinetic energy operator $\frac{1}{2I}\hat{\mathbf{J}}^2$ where $\hat{\mathbf{J}}$ is the generator of body-fixed rotations and I is a

constant moment of inertia. Thus we have

$$\mathcal{H} = -\frac{1}{2}\frac{d^2}{dx^2} + \frac{1}{2I}\hat{\mathbf{J}}^2. \tag{6.1}$$

We are now in a position to set up the problem on the fundamental domain.

A vicinity of the fundamental domain is shown in Figure 2, consisting of the vertex V together with the three edges leaving it. Let $x_1, x_3 \in [0, L_1]$ and $x_2 \in [0, L_2]$ be coordinates along the edges leaving the vertex, with the (green) fundamental domain corresponding to $x_1 \in [0, L_1]$ and $x_2 \in \left[0, \frac{L_2}{2}\right]$. Suppose $\Psi^{(T)}$ is a state which transforms in the irrep T of S_5^* (so has degeneracy $\dim T$) and that for every permutation $\pi \in S_5^*$ we have the corresponding matrix action on the state

$$\Psi_n^{(T)} \to \sum_{m=1}^{\dim T} T\left(\pi\right)_{nm} \Psi_m^{(T)}. \tag{6.2}$$

On edge $j \in \{1, 2, 3\}$ the Hamiltonian is

$$\mathcal{H}_j = -\frac{1}{2}\frac{d^2}{dx_j^2} + \frac{1}{2I}\hat{\mathbf{J}}^2. \tag{6.3}$$

Rotational symmetry implies that states can be classified by quantum numbers J (total angular momentum) and $M \in \{-J, \ldots, +J\}$ (space-fixed angular momentum projection). So we assume that $\Psi_n^{(T)}$ is a (J, M) state. We can expand the wavefunction on edge j in terms of (J, M) symmetric-top eigenfunctions (with body-fixed angular momentum projection $K \in \{-J, \ldots, +J\}$) and plane waves:

$$\sum_{K=-J}^{J} \left(a_{njK}e^{ikx_j} + b_{njK}e^{ik(L_j-x_j)}\right)|JKM\rangle \tag{6.4}$$

with corresponding energy eigenvalues $E = \frac{1}{2}k^2 + \frac{1}{2I}J(J+1)$.

Now recall that we have S_5^* symmetry: for example, the permutation $(12)(543) \in S_5^*$ maps configurations on edge 1 with $x_1 = x$ to configurations on edge 3 with $x_3 = L_1 - x$. The orientations differ by some rotation $R = \exp\left(-i\alpha\hat{\mathbf{n}} \cdot \hat{\mathbf{J}}\right)$ (α and $\hat{\mathbf{n}}$ are estimated in Appendix 6.A). We can, therefore, deduce the wavefunction on edge 3 from the wavefunction on edge 1. Explicitly, it is

$$\sum_{m=1}^{\dim T}\sum_{K'=-J}^{J}\sum_{K=-J}^{J} T\left((12)(543)\right)_{nm} \exp\left(-i\alpha\hat{\mathbf{n}} \cdot \hat{\mathbf{J}}\right)_{KK'} \tag{6.5}$$

$$\left(a_{m1K'}e^{ik(L_1-x_3)} + b_{m1K'}e^{ikx_3}\right)|JKM\rangle.$$

77

Now we impose quantum graph boundary conditions at the vertex V joining edges $1, 2$ and 3. As we have expressed the wavefunction on edge 3 in terms of its values on edges 1 and 2, these boundary conditions give us some new conditions relating just the wavefunctions on edges 1 and 2 which have to be satisfied. For example, continuity of the wavefunction at V ($x_1 = x_2 = x_3 = 0$) leads to

$$\sum_{m=1}^{\dim T} \sum_{K'=-J}^{J} T\left((12)(543)\right)_{nm} \exp\left(-i\alpha\hat{\mathbf{n}} \cdot \hat{\mathbf{J}}\right)_{KK'} \left(a_{m1K'}e^{ikL_1} + b_{m1K'}\right)$$
$$= \left(a_{n1K} + b_{n1K}e^{ikL_1}\right) = \left(a_{n2K} + b_{n2K}e^{ikL_2}\right). \qquad (6.6)$$

A similar calculation, considering the permutation $(23)(45)$, gives boundary conditions at the midpoint of edge 2. Thus we end up with a set of linear equations in the variables $a_{n1K}, a_{n2K}, b_{n1K}, b_{n2K}$ which, as we see in (6.6), depend on momentum k. These are our quantization conditions and can be handled numerically.

The parities of the resulting states can be deduced by noting that, on edge 2, spatial inversion can be realised by the combined action of the permutation $(45) \in S_5$ followed by a rotation by π about the axis normal to the plane of C_s reflection symmetry.

6.3 Results and discussion

We display the lowest-lying rovibrational states in Tables 1-5, listed against reference data from the seven-dimensional variational calculation in [64]. The states which are Pauli-allowed are indicated in bold. Recall that CH_5^+ involves five identical protons (fermions) and so, by Pauli-allowed, we mean rovibrational states which are compatible with Pauli exchange statistics. In more detail, the total wavefunction involves both rovibrational degrees of freedom as well as spin degrees of freedom for the protons. The five protons have spin $\frac{1}{2}$ and so the spin wavefunction for the total system lies in the irrep

$$V_{\text{spin}} = \frac{\mathbf{1}}{\mathbf{2}} \otimes \frac{\mathbf{1}}{\mathbf{2}} \otimes \frac{\mathbf{1}}{\mathbf{2}} \otimes \frac{\mathbf{1}}{\mathbf{2}} \otimes \frac{\mathbf{1}}{\mathbf{2}} \cong \frac{\mathbf{5}}{\mathbf{2}} \oplus 4\frac{\mathbf{3}}{\mathbf{2}} \oplus 5\frac{\mathbf{1}}{\mathbf{2}}.$$

The permutation group S_5 acts on the proton identities, under which the above space has the irrep decomposition

$$V_{\text{spin}} = 6A_1 \oplus 4G_1 \oplus 2H_1.$$

Spin states lying in this space are to be combined with our rovibrational wavefunctions in a way which reflects the correct statistics for identical protons: the combined wavefunction must transform as A_2 under S_5 permutations. One finds that spin states in the irreps A_1, G_1, H_1 can be combined with rovibrational states in the irreps A_2, G_2, H_2 respectively. Therefore

Irrep	$E(\text{cm}^{-1})$	E_{ref}	Irrep	$E(\text{cm}^{-1})$	E_{ref}
A_1^+	0.0	0.0	G_2^-	**11.4**	**9.9**
H_1^+	22.2	20.4	H_2^-	**39.6**	**41.1**
G_1^+	44.8	49.4	I^-	49.7	58.4
H_2^+	**50.2**	**59.3**	H_1^-	96.0	113.7
I^+	95.2	112.0	G_2^-	**100.9**	**112.7**
H_1^+	112.4	122.0	H_2^-	**148.8**	**139.4**

Table 6.1: Lowest $J = 0$ states for quantum graph model (exactly reproducing the results in [5]), together with a comparison to reference data E_{ref} up to 150 cm^{-1} taken from [64]. Pauli-allowed states are in bold.

only the rovibrational states which transform in the irreps $A_2^\pm$, $G_2^\pm$ and $H_2^\pm$ are physically allowed and these are the states which are in bold in our tables.

We have used the values $L_1 = 61.2\sqrt{m_e}a_0$ and $L_2 = 1.0\sqrt{m_e}a_0$, following the suggestion in [5], to give the best fit to the $J = 0$ data (here m_e is the electron mass and a_0 the Bohr radius). For the moment of inertia, we have picked a physically reasonable value $\frac{1}{I} = 8$ cm^{-1} [67].

We see that the quantum graph states give a good qualitative fit to the reference data even when we extend to $J > 0$, with correct S_5^* irrep assignments along with reasonable energy values. The agreement is remarkable considering the simplicity of the quantum graph model. We expect the model to break down at higher energies, where neglected degrees of freedom become important, but these results demonstrate that the graph model is sufficient to understand many states in the low-energy regime. Our $J = 4$ states go beyond those computed in [64], in which only states with $J \leq 3$ were considered. Based on the agreement in the $J \leq 3$ sector, we expect our $J = 4$ data to give a reliable description of the states of CH_5^+.

6.4 Summary and conclusions

In this chapter we have introduced a rovibrational quantum graph model for the nuclear dynamics of the CH_5^+ molecular ion. The model is based on just two low-energy bending motions which take the molecular ion between versions of its equilibrium structure. These distinct versions are represented as the vertices of a metric graph, with the low-energy pathways represented as edges of the graph. We have shown that the rovibrational quantum graph model can describe a large number of rovibrational states in good agreement with reference data. Our computed states go beyond other calculations and we have reported our predictions for the $J = 4$ Pauli-allowed states of CH_5^+.

Irrep	E	E_{ref}	Irrep	E	E_{ref}
I^+	15.3	14.7	G_1^-	11.6	11.3
G_2^+	**25.5**	**23.0**	H_2^-	**27.3**	**24.9**
H_2^+	**32.5**	**31.9**	I^-	30.9	29.7
I^+	43.9	46.5	H_1^-	38.4	40.3
G_2^+	**51.4**	**57.9**	A_1^-	49.9	55.4
H_1^+	53.4	57.1	G_2^-	**52.6**	**62.1**
G_1^+	54.1	61.3	I^-	55.3	59.6
H_2^+	**62.9**	**72.0**	H_1^-	57.3	67.1
I^+	64.1	72.1	G_1^-	58.8	62.3
H_1^+	92.7	115.1	H_2^-	**66.6**	**75.5**
G_2^+	**101.4**	**117.1**	I^-	94.9	115.0
H_2^+	**103.1**	**117.2**	H_1^-	96.8	115.9
I^+	107.2	122.7	G_2^-	**107.8**	**122.5**
G_1^+	112.3	126.5	H_2^-	**109.9**	**122.6**
A_2^+	**113.5**	**125.8**	G_1^-	113.8	126.3
H_2^+	**137.0**	**138.7**	I^-	127.1	134.0
I^+	154.2	145.2	H_1^-	149.9	143.4

Table 6.2: Lowest $J = 1$ states for quantum graph model, together with a comparison to reference data E_{ref} up to 150 cm^{-1} taken from [64]. Pauli-allowed states are in bold.

Irrep	E	E_{ref}	Irrep	E	E_{ref}
H_1^+	29.5	29.1	H_2^-	**32.1**	**31.6**
G_1^+	32.2	32.2	I^-	34.2	33.2
H_2^+	**40.7**	**39.5**	H_1^-	36.4	36.9
H_1^+	46.3	46.7	A_2^-	**50.9**	**45.0**
G_2^+	**52.7**	**48.5**	G_2^-	**52.2**	**50.0**
I^+	53.4	53.9	I^-	53.3	54.6
H_2^+	**54.8**	**59.3**	H_2^-	**55.3**	**56.4**
G_1^+	55.8	59.2	G_2^-	**58.1**	**64.8**
A_2^+	**62.0**	**73.3**	G_1^-	60.8	66.1
I^+	68.5	76.5	H_1^-	67.4	73.4
H_2^+	**72.5**	**78.9**	I^-	68.8	74.5
H_1^+	74.3	82.6	H_1^-	76.9	82.5
G_1^+	74.9	78.1	H_2^-	**79.8**	**86.7**
I^+	82.5	88.5	I^-	84.0	94.4
H_1^+	86.8	95.0	G_2^-	**87.7**	**96.4**
G_2^+	**88.5**	**98.5**	G_1^-	87.8	92.0
A_1^+	90.4	92.2	A_2^-	**99.7**	**126.2**
G_1^+	102.1	126.1	G_1^-	101.6	126.8
G_2^+	**102.6**	**127.9**	H_2^-	**103.4**	**126.3**
I^+	105.7	126.5	I^-	108.0	128.0
H_1^+	111.5	129.8	H_2^-	**117.6**	**132.9**
H_2^+	**115.4**	**134.7**	G_2^-	**118.2**	**133.3**
I^+	127.2	138.8	H_1^-	121.1	137.6
H_2^+	**128.7**	**140.9**	I^-	127.6	141.3
G_2^+	**140.1**	**147.6**	A_1^-	139.9	150.6
G_1^+	146.8	152.7	G_2^-	**148.8**	**152.0**
H_1^+	151.3	151.6	H_1^-	152.4	155.2
I^+	154.6	154.3	I^-	155.1	154.8
G_1^+	158.0	157.0	G_1^-	157.8	152.4
A_1^+	161.8	148.4	H_2^-	**171.1**	**162.3**

Table 6.3: Lowest $J = 2$ states for quantum graph model, together with a comparison to reference data E_{ref} up to 170 cm^{-1} taken from [64]. Pauli-allowed states are in bold.

Irrep	E	E_{ref}	Irrep	E	Irrep	E	E_{ref}	Irrep	E
I^+	56.1		G_1^+	113.1	H_1^-	54.6		A_2^-	**115.9**
H_1^+	59.0		H_1^+	115.3	G_1^-	56.4		I^-	115.9
G_2^+	**61.6**	**60.2**	G_2^+	**118.6**	I^-	59.2		H_2^-	**117.7**
H_2^+	**61.9**	**61.1**	I^+	119.8	G_2^-	**66.9**	**65.0**	I^-	117.8
I^+	63.0		H_1^+	120.2	H_1^-	67.2		G_1^-	118.7
G_1^+	68.1		A_1^+	121.1	A_1^-	68.0		H_2^-	**122.8**
H_2^+	**78.4**	**83.5**	I^+	122.1	I^-	68.7		G_2^-	**124.4**
G_2^+	**79.3**	**81.1**	H_2^+	**125.6**	H_2^-	**74.6**	**74.8**	H_1^-	124.8
I^+	80.4		H_1^+	131.9	H_1^-	79.3		G_1^-	125.4
A_2^+	**82.0**	**81.6**	G_2^+	**140.0**	G_1^-	79.7		I^-	135.7
I^+	83.3		H_2^+	**143.3**	H_2^-	**81.5**	**84.5**	H_2^-	**140.6**
G_1^+	88.1		I^+	143.9	G_2^-	**81.6**	**84.5**	H_1^-	152.5
G_2^+	**89.6**	**88.1**	I^+	151.4	G_2^-	**90.0**	**98.1**	H_2^-	**154.3**
H_1^+	90.0		G_1^+	156.4	I^-	92.8		G_1^-	156.6
H_2^+	**92.3**	**97.2**	G_1^+	171.4	I^-	97.5		G_2^-	**157.7**
H_1^+	99.5		H_1^+	171.4	H_1^-	98.0		A_1^-	170.8
I^+	103.8		G_2^+	**173.6**	G_1^-	99.7		G_1^-	176.0
G_2^+	**111.7**		H_2^+	**174.5**	H_2^-	**106.0**		H_1^-	176.8
H_2^+	**112.7**				H_1^-	112.3			

Table 6.4: Lowest $J = 3$ states for quantum graph model, compared to reference data E_{ref} from [64] where available (and only for the Pauli-allowed states). Pauli-allowed states are in bold.

Irrep	E	Irrep	E	Irrep	E	Irrep	E
H_2^+	**89.1**	H_2^+	**147.0**	G_2^-	**90.0**	H_2^-	**136.2**
A_2^+	**97.5**	G_2^+	**151.0**	H_2^-	**91.1**	G_2^-	**140.5**
G_2^+	**101.1**	H_2^+	**153.0**	H_2^-	**95.7**	H_2^-	**144.3**
H_2^+	**101.4**	G_2^+	**154.2**	G_2^-	**96.4**	G_2^-	**150.2**
H_2^+	**111.3**	H_2^+	**156.1**	A_2^-	**111.2**	H_2^-	**151.8**
G_2^+	**114.9**	G_2^+	**171.3**	G_2^-	**113.7**	H_2^-	**158.0**
G_2^+	**124.2**	H_2^+	**190.7**	H_2^-	**119.2**	A_2^-	**172.0**
H_2^+	**127.6**	A_2^+	**193.7**	H_2^-	**123.5**	G_2^-	**172.8**
H_2^+	**135.6**	H_2^+	**226.5**	G_2^-	**130.7**	H_2^-	**175.0**

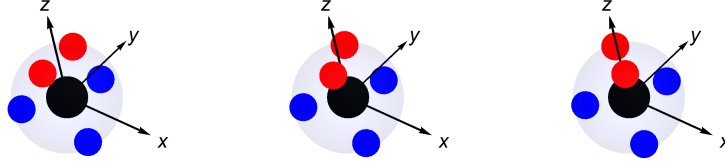Table 6.5: Lowest $J = 4$ Pauli-allowed states for quantum graph model.

Figure 6.3: Choice of body-fixed axes.

6.A   Appendix

Estimating R

Here we estimate the rotation R appearing in Section 6.2.2 which relates the orientations of the configurations appearing at each end of an edge. A reasonable approximation is to take the positions of the protons to be on the surface of a sphere (centred on the carbon nucleus) as illustrated in Figure 6.3. We take the bond angles to be those which give the closest match of the proton positions to *ab initio* values: the polar angle of the H_2 unit (in radians) is taken to be 0.42 while the polar angle of the other three protons is taken to be 1.89.

Consider configurations along edge 1. Our choice of body-fixed axes (x, y, z) are indicated in the picture: notice that as the H_2 unit rotates relative to the CH_3 tripod, the entire molecule also rotates at a rate such that the total angular momentum vanishes. The vanishing of the angular momentum ensures that, for this choice of body-fixed axes, there are no kinetic rotation-vibration cross-terms. The rates of rotation are related by the ratio of the moments of inertia, I_1 and I_2, of the H_2 and of the whole molecule. In particular, by the point that the H_2 unit has rotated a full $\frac{2\pi}{6}$ with respect to the CH_3 tripod, the molecule as a whole will have rotated in the opposite sense by $\Delta\theta = \left(\frac{I_1}{I_2}\right)\left(\frac{2\pi}{6}\right)$. Then the rotation relating the configurations at the two endpoints of edge 1 is a rotation by $\frac{2\pi}{3} + \Delta\theta \approx 2.21$ about the body-fixed z-axis, and so we take $R = \exp\left(-i\alpha\hat{\mathbf{n}} \cdot \hat{\mathbf{J}}\right)$ with $\alpha \approx 2.21, \hat{\mathbf{n}} = (0, 0, -1)$ in our boundary conditions.

Edge 2 is treated similarly, giving a rotation

$$\tilde{R} = \exp\left(-i\pi\,(0, 0, 1) \cdot \hat{\mathbf{J}}\right) \exp\left(-i\beta\hat{\mathbf{m}} \cdot \hat{\mathbf{J}}\right)$$

where $\beta \approx 1.39$, $\hat{\mathbf{m}} = (-1, 0, 0)$.

Chapter 7

Conclusions

In this thesis we investigated a variety of problems in both nuclear physics and molecular physics with an emphasis on rovibrational dynamics. In Chapter 2 we introduced the Skyrme model, a nonlinear field theory in which atomic nuclei are identified with topological solitons. We developed models of Helium-4 (i.e. the α-particle) and the Lithium-7/Beryllium-7 isodoublet based on quantised small vibrations of the corresponding Skyrmions. We incorporated Coriolis effects which had been previously neglected, deriving the form of these rotation-vibration interactions within a geometric point of view. The results match the experimental data very well, particularly for the α-particle, with the Coriolis terms significantly improving the fit. The model explains all observed α-particle states up to 28.6 MeV, and we predict one so far unobserved 0^+ state at 23.4 MeV. Our analysis of Lithium-7/Beryllium-7 clarifies the role of isospin-vibration coupling in Skyrmion quantization and we believe that the inclusion of such effects may be crucial for the Skyrme model description of large nuclei.

Having studied the α-particle in Chapter 2, we went on to study α-particle models for Carbon-12 and Oxygen-16 in Chapters 3, 4 and 5. These involve particular arrangements of α-particles which are known to correspond to low-energy Skyrmion solutions. The QGM for Carbon-12 was introduced in Chapter 3. This model is a significant improvement on a previous analysis which attempted to explain the low-lying states of Carbon-12 in terms of rigidly rotating Skyrmions with the symmetries of an equilateral triangle and a linear chain. Allowing for more general isosceles triangular arrangements with smaller symmetry groups, our model permits states with spins and parities which were previously unexplained within the Skyrme model approach. The associated wavefunctions are often peaked at a bent arm arrangement, consistent with the findings of sophisticated lattice calculations based on chiral effective field theory. Also, we predict three new energy levels for the Carbon-12 nucleus at around 20 MeV, with spin and parity combinations 3^+, 4^- and 4^+.

In Chapter 4 we developed a formalism for calculating electromagnetic transition rates between nuclear states. Within this formalism, applicable to a broad class of rovibrational

models, we calculated rates in the QGM as well as in a similar α-particle model for Oxygen-16 inspired by nuclear dynamics in the Skyrme model. For Carbon-12 both our model and other competing models reproduce the available experimental data well, and more experimental work is needed to further differentiate the models. The results for Oxygen-16 are less promising, although the situation may be improved by relaxing certain approximations. One way this might be done is by developing a quantum graph model for Oxygen-16. We began to explore this possibility in Chapter 5, in which we used a toy quantum graph model to illustrate some shortcomings of previous work. In particular, we showed that the body-fixed frame convention usually adopted is not globally well-defined. We offered a geometric perspective on the problem, regarding the total configuration space as an SO(3)-bundle and clarifying how to consistently construct sensible wavefunctions on this space.

Finally, we turned from nuclear to molecular physics. In Chapter 6 we used our insights developed in the previous chapters to model the low-energy rovibrational dynamics of protonated methane in terms of a quantum particle on a graph, or more precisely on an SO(3)-bundle over a graph. This led to a simple model for the very complex dynamics of protonated methane, allowing us to calculate rovibrational states up to spin $J = 4$ for the first time. Computation of these states was only possible as a result of the drastic reduction in the number of degrees of freedom offered by the novel quantum graph model. We found an excellent match to available reference data over a large number of rovibrational states up to $J = 3$. Our computed states go beyond the regime studied in other calculations, and we presented our predictions for over 30 new Pauli-allowed states with angular momentum $J = 4$. We hope that comparison to experiment (or at least other theoretical approaches) will be possible in the near future.

Bibliography

[1] R. S. Berry, "Correlation of Rates of Intramolecular Tunneling Processes, with Application to Some Group V Compounds," J. Chem. Phys. 32 (1960) 933.

[2] C. Raynaud et al., "Berry pseudorotation mechanism for the interpretation of the 19F NMR spectrum in PF_5 by Ab Initio molecular dynamics simulations," ChemPhysChem. 7 (2006) 407.

[3] P. R. Schreiner et al., "CH_5^+: The never-ending story or the final word?" J. Chem. Phys. 99 (1993) 3716.

[4] H. Schmiedt, P. Jensen and S. Schlemmer, "Collective Molecular Superrotation: A Model for Extremely Flexible Molecules Applied to Protonated Methane," Phys. Rev. Lett. 117 (2016) 223002.

[5] C. Fábri and A. G. Császár., "Vibrational quantum graphs and their application to the quantum dynamics of CH_5^+," Phys. Chem. Chem. Phys. 20 (2018) 16913.

[6] J. A. Wheeler, "Molecular viewpoints in nuclear structure," Phys. Rev. 52 (1937) 1083.

[7] C. J. Halcrow, C. King and N. S. Manton, "Dynamical $\alpha-$cluster model of ^{16}O," Phys. Rev. C 95 (2017) 031303.

[8] A. Shapere and F. Wilczek, "Gauge kinematics of deformable bodies," American J. of Phys. 57 (1989) 514.

[9] J. I. Rawlinson, "Coriolis terms in Skyrmion quantization," Nucl. Phys. B 949 (2019) 114800.

[10] R. G. Littlejohn and M. Reinsch, "Gauge fields in the separation of rotations and internal motions in the n-body problem," Rev. Mod. Phys. 69 (1997) 213.

[11] S. B. Gudnason and C. Halcrow, "Vibrational modes of Skyrmions," Phys. Rev. D 98 (2018) 125010.

[12] H. A. Jahn, "Note on Coriolis Coupling Terms in Polyatomic Molecules," Phys. Rev. 56 (1939) 680.

[13] O. V. Manko, N. S. Manton and S. W. Wood, "Light nuclei as quantized Skyrmions," Phys. Rev. C 76 (2007) 055203.

[14] TUNL Nuclear Data Evaluation Project, Energy Levels of Light Nuclei, A=3-20, www.tunl.duke.edu/nucldata.

[15] C. Barnes, K. Baskerville and N. Turok, "Normal Modes of the $B = 4$ Skyrme Soliton," Phys. Rev. Lett. 79 (1997) 367.

[16] Character tables for chemically important point groups, symmetry.jacobs-university.de.

[17] D. Finkelstein and J. Rubinstein, "Connection between spin, statistics, and kinks," J. Math. Phys. 9 (1968) 1762.

[18] S. Krusch, "Homotopy of rational maps and the quantization of Skyrmions," Ann. of Phys. 304 (2003) 103.

[19] R. F. Frosch et al., "Inelastic electron scattering from the alpha particle," Phys. Lett. 19 (1965) 155.

[20] C. Werntz and H. Uberall, "Collective Nuclear "Breathing Mode" Model with Application to Helium-4 Monopole State," Phys. Rev. 149 (1966) 762.

[21] S. Bacca et al., "Is the first excited state of the $\alpha-$particle a breathing mode?," Phys. Rev. C 91 (2015) 024303.

[22] A. de-Shalit and J. D. Walecka, "Nuclear Spectroscopy in the $\alpha-$particle," Phys. Rev. 147 (1966) 763.

[23] W. K. Baskerville, "Vibrational spectrum of the B = 7 Skyrme soliton," arXiv:hep-th/9906063.

[24] C. J. Halcrow, "Vibrational quantisation of the $B = 7$ Skyrmion," Nucl. Phys. B 904 (2016) 106.

[25] C. J. Halcrow, "Skyrmions - beyond rigid body quantisation," Doctoral thesis, Cambridge University (2017).

[26] C. J. Halcrow, N. S. Manton and J. I. Rawlinson, "Quantized Skyrmions from SU(4) weight diagrams," Phys. Rev. C 97 (2018) 034307.

[27] J. I. Rawlinson, "An alpha particle model for Carbon-12," Nucl. Phys. A 975 (2018) 122.

[28] F. Hoyle, "On Nuclear Reactions Occuring in Very Hot Stars. I. the Synthesis of Elements from Carbon to Nickel," Astrophys. J. Suppl. Ser. 1 (1954) 12.

[29] D. N. F. Dunbar et al., "The 7.68-MeV State in ^{12}C," Phys. Rev. 92 (1953) 649.

[30] C. W. Cook et al., "B^{12}, C^{12}, and the Red Giants," Phys. Rev. 107 (1957) 508.

[31] P. H. C. Lau and N. S. Manton, "States of Carbon-12 in the Skyrme Model," Phys. Rev. Lett. 113 (2014) 232503.

[32] E. Epelbaum et al., "Structure and Rotations of the Hoyle State," Phys. Rev. Lett. 109 (2012) 252501.

[33] R. Bijker and F. Iachello, "The Algebraic Cluster Model: Three-Body Clusters," Ann. of Phys. 298 (2002) 334.

[34] Y. Funaki et. al., "Resonance states in ^{12}C and α-particle condensation," Eur. Phys. J. A 24 (2005) 321.

[35] M. Freer and H. O. U. Fynbo, "The Hoyle state in ^{12}C," Prog. Part. Nucl. Phys. 78 (2014) 1.

[36] D. J. Marin-Lambarri et al., "Evidence for Triangular D_{3h} Symmetry in ^{12}C," Phys. Rev. Lett. 113 (2014) 012502.

[37] P. Kuchment, "Analysis on Graphs and its Applications," Proc. Symp. Pure Math. 77 (2008) 291.

[38] L. Pauling, "The Diamagnetic Anisotropy of Aromatic Molecules," J. Chem. Phys. 4 (1936) 673.

[39] M. J. Richardson and N. L. Balázs, "On the network model of molecules and solids," Ann. of Phys. 73 (1972) 308.

[40] C. J. Halcrow and J. I. Rawlinson, "Electromagnetic transition rates of Carbon-12 and Oxygen-16 in rotational-vibrational models," arXiv:2001.07595.

[41] M. Freer et al., "Re-examination of the excited states of ^{12}C," Phys. Rev. C 76 (2007) 034320.

[42] D. Robson, "Evidence for the tetrahedral nature of ^{16}O," Phys. Rev. Lett. 42 (1979) 876.

[43] A. M. Bergstrom et. al., "Electroexcitation of ^{16}O levels near 10 MeV excitation," Nucl. Phys. A 213 (1973) 609.

[44] G. S. Adkins, C. R. Nappi and E. Witten, "Static properties of nucleons in the Skyrme model," Nucl. Phys. B 228 (1983) 552.

[45] R. Bijker and F. Iachello, "Evidence for tetrahedral symmetry in ^{16}O," Phys. Rev. Lett. 112 (2014) 152501.

[46] J. H. Kelly, J. E. Purcell and C. G. Sheu, "Energy levels of light nuclei $A = 12$," Nucl. Phys. A 968 (2017) 71.

[47] D. R. Tiley, H. R. Weller and C. M. Cheves, "Energy levels of light nuclei $A = 16 - 17$," Nucl. Phys. A 565 (1993) 1.

[48] J. M. Blatt and V. W. Weisskopf, "Theoretical Nuclear Physics", John Wiley & Sons, New York (1952).

[49] W. Bauhoff, H. Schultheis and R. Schultheis, "Alpha cluster model and the spectrum of ^{16}O," Phys. Rev. C 29 (1984) 1046.

[50] C. J. Halcrow, C. King and N. S. Manton, "Oxygen-16 Spectrum from Tetrahedral Vibrations and their Rotational Excitations," Int. J. Mod. Phys. E 28 (2019) 1950026.

[51] N. Curtis et al., "Investigation of the 4-α linear chain state in ^{16}O," Phys. Rev. C 88 (2013) 064309.

[52] E. Epelbaum, H. Krebs, T. A. Lähde, D. Lee, U.-G. Meissner and G. Rupak, *"Ab initio calculation of the spectrum and structure of ^{16}O,"* Phys. Rev. Lett. 112 (2014) 102501.

[53] R. Bijker and F. Iachello, "The algebraic cluster model: structure of ^{16}O," Nucl. Phys. A 957 (2017) 154.

[54] L. Carson, "Static properties of ^{3}He and ^{3}H in the Skyrme model," Nucl. Phys. A 535 (1991) 479.

[55] J. I. Rawlinson, "Quantum graph model for rovibrational states of protonated methane," J. Chem. Phys. 151 (2019) 164303.

[56] V. L. Tal'roze and A. K. Lyubimova, Doklady Akad. Nauk SSSR 86 (1952) 909.

[57] D. Marx and M. Parrinello, "CH_5^+: The Cheshire Cat smiles," Science 284 (1999) 59.

[58] E. Herbst et al., "Indirect observation of unobservable interstellar molecules," Astrophys. J. 215 (1977) 503.

[59] A. Gamba, G. Morosi and M. Simonetta, "An investigation of the geometry of the CH_5^+ ion by the CNDO method," Chem. Phys. Lett. 3 (1969) 20.

[60] V. Dyczmons and W. Kutzelnigg, "Ab initio calculations of small hydrides including electron correlation," Theoretica chimica acta 33 (1974) 239.

[61] H. F. Schaefer et al., "CH_5^+: The never-ending story or the final word?" J. Chem. Phys. 99 (1993) 3716.

[62] E. T. White, J. Tang and T. Oka, "CH_5^+: The Infrared Spectrum Observed," Science 284 (1999) 135.

[63] O. Asvany et al., "Experimental ground-state combination differences of CH_5^+," Science 347 (2015) 1346.

[64] X-G. Wang and T. Carrington, "Calculated rotation-bending energy levels of CH_5^+ and a comparison with experiment," J. Chem. Phys. 144 (2016) 204304.

[65] C. Fábri, M. Quack and A. G. Császár, "On the use of nonrigid-molecular symmetry in nuclear motion computations employing a discrete variable representation: A case study of the bending energy levels of CH_5^+," J. Chem. Phys. 147 (2017) 134101.

[66] X-G. Wang and T. Carrington, "Vibrational energy levels of CH_5^+," J. Chem. Phys. 129 (2008) 234102.

[67] L. M. Johnson and A. B. McCoy, "Evolution of Structure in CH_5^+ and Its Deuterated Analogues," J. Phys. Chem. A 110 (2006) 8213.